CONTROLS OF LITHIUM AND STRONTIUM ISOTOPES SPATIAL VARIABILITY ACROSS THE YUKON RIVER BASIN: IMPLICATIONS FOR WEATHERING IN A WARMING BASIN

Submitted by: Myunghak Kang

Thesis submitted to the University of Ottawa in partial fulfillment of the requirements for the degree of Master of Science in Earth Sciences

Department of Earth Sciences
Faculty of Science
University of Ottawa

Supervisor:
Dr. Clément P. Bataille (Department of Earth Sciences)

Thesis Committee:

Dr. Ian D. Clark, University of Ottawa

Dr. Shuangquan Zhang, Carleton University

Abstract

The Yukon River drains a large catchment underlain by a range of geological units characterized by diverse topography, environmental conditions, and land cover. The Yukon River catchment also displays a permafrost cover gradient and has active alpine glaciers in its headwaters. With ongoing warming, permafrost degradation, glaciers retreat, and land cover changes, the hydrochemistry of the Yukon River will likely change with risks for water quality and ecosystem sustainability. Here, we report elemental and isotopic data across the Yukon River to unravel the processes controlling the geochemistry of the dissolved load across the watershed and investigate the sensitivity of hydrochemistry to climate conditions.

We analyze 102 samples from most major tributaries of the Yukon River for major and trace elements, strontium isotope ratio ($^{87}Sr/^{86}Sr$) and lithium isotope composition (δ^7Li). Elemental and isotopic geochemistry displays strong spatial patterns that primarily correlate with lithological, topographic and climatic characteristics over the watershed. In the glacial and mountainous headwaters, we observe low Li/Na ratio and low δ^7Li values (<15‰). We suggest that glaciated headwaters are characterized by a very high denudation rate and low secondary mineral formation rate explaining the low δ^7Li values. In most of the permafrost-covered lowlands, we observe relatively constant Li/Na ratio and δ^7Li values suggesting that weathering intensity is at a steady state. Conversely, in the non-permafrost-covered lowlands, we observe higher and more variable Li/Na ratio and δ^7Li values suggesting increased weathering intensity when permafrost is absent. In the lowlands, glaciated or not, $^{87}Sr/^{86}Sr$ ratios remain within a tight range of values (0.709-0.715) and reflect the variable contribution of carbonate and silicate units throughout the basin. We found an interesting relationship between δ^7Li values and $^{87}Sr/^{86}Sr$ ratios, suggesting a strong geology influence on weathering processes. When $^{87}Sr/^{86}Sr$ are low or very high, δ^7Li values tend to be high (>25‰), whereas when $^{87}Sr/^{86}Sr$ are intermediate δ^7Li values are low. We argue that the presence of igneous rock units within the catchment is an important control of weathering intensity as igneous rock units can contribute fresh primary minerals for weathering reactions. Weathering intensity is also strongly associated with temperature and permafrost cover across the Yukon River. As temperature increases and permafrost thaws, the weathering intensity increases, modifying the flux of elements to rivers. As the climate continues to warm in the future, the Yukon River hydrochemistry will continue to evolve, reflecting the increased contribution of soils and clays to river water chemistry.

Acknowledgements

I would like to express my sincerest gratitude to my supervisor, Dr. Clément Bataille, for his continued guidance, support and encouragement. His constructive supervision, instruction and insightful criticism are very appreciated. I am deeply grateful to be a part of the Yukon project, and for the opportunity to have worked with him and the experiences, I have learned during graduate school. I would like to thank the fellow members of the SAiVE group for their feedback and helpful advice. I am very appreciative of Dr. Sean Brennan and other contributors to this project for providing Yukon River samples.

I would also like to thank Zhaoping Yang and Isabelle Girard at the Geological Survey of Canada for allowing me to work in the clean lab and providing excellent sample analyses. I am very grateful to Nimal DeSilva and Smita Mohanty at the Geochemistry lab for teaching me analytical techniques and instrument operations. I also want to thank Shaungquan Zhang at the IGGRC lab for numerous attempts on sample analysis. Many thanks to my lab mates and office mates for their understanding, help and good conversation.

I would like to thank my friends for distractions, encouragement and laughs. Finally, I am incredibly grateful for the support, love, and patience of my family during the pursuit of this degree. Thank you all very much.

Table of Contents

List of Figures

List of Tables

1. Introduction

Permafrost covers about a quarter of the land surface in the northern hemisphere and exerts an essential control on the hydrochemistry of northern rivers. Permafrost often acts as a semi-impermeable barrier between the soil layers, limiting weathering reactions in soils and interactions between groundwater and surface water (Kokelj & Burn, 2005; Douglas et al., 2013). Permafrost also stores large quantities of organic carbon and nutrient (Douglas et al., 2013). The ongoing global warming could drive a large-scale permafrost degradation in high latitudes, thereby significantly changing the hydrochemistry of northern rivers (Frey & McClelland, 2009; Toohey et al., 2016), as well as land cover and ecosystems (Brabets et al., 2000).

The Yukon watershed lies within the permafrost zone with a varying range of extent and depth (Fig.1), which provides an ideal setting to study permafrost and weathering interactions at the regional scale. A large increase in solute concentrations has been observed at the Yukon River mouth (Toohey et al., 2016); however, the influence of permafrost degradation on these hydrochemical changes is not well-established because river chemistry can be influenced by many variables (Toohey et al., 2016). The objective of this thesis is to understand better the interactions of permafrost cover and weathering processes across the Yukon River watershed. It is hypothesized that catchments with low permafrost cover will show increased weathering intensity than those with continuous permafrost cover. This increase in weathering intensity will lead to a higher contribution of surface weathering fluxes to river hydrochemistry in an area without permafrost cover. Changes in the hydrochemistry of the Yukon River (Toohey et al., 2016) would undoubtedly have some impacts on terrestrial and aquatic ecosystems and impact the Yukon River watershed residents who often directly depend on river resources (Holder & Senecal-Albrecht, 1998; Brabets et al., 2000).

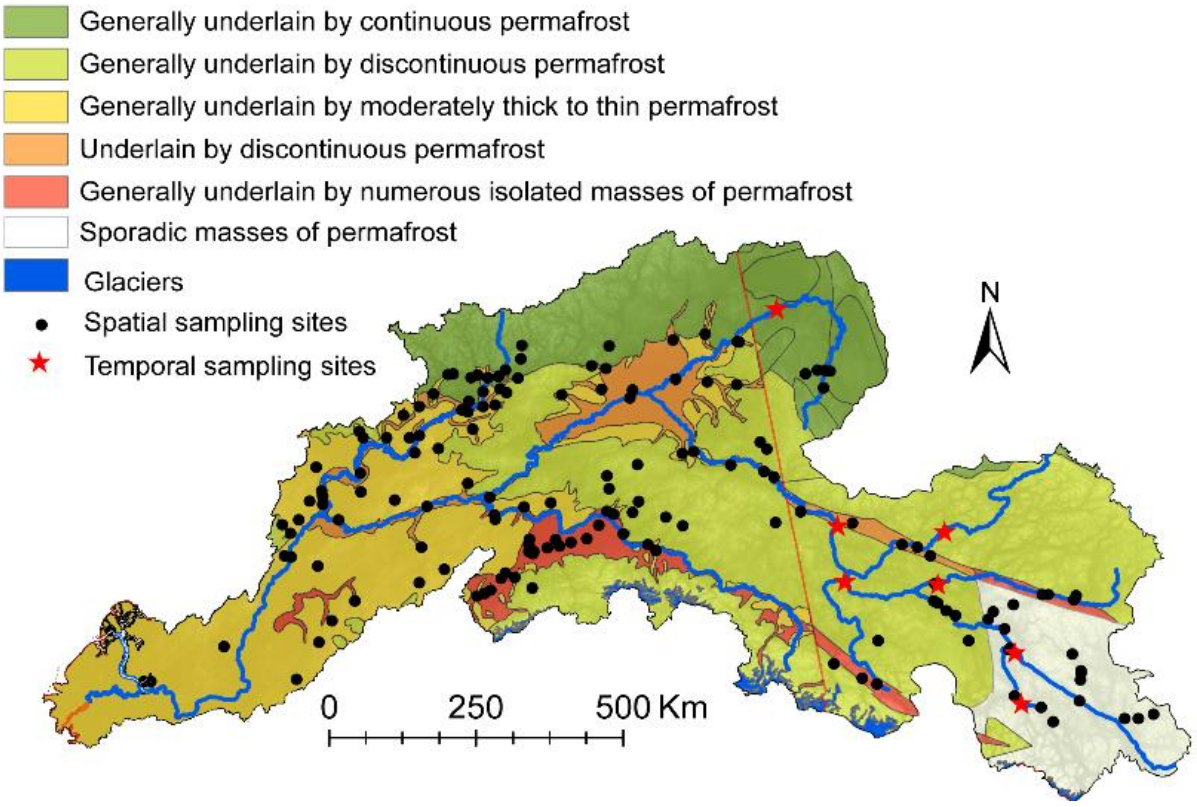

Figure 1: The Yukon River Watershed, permafrost cover and sample locations.

I will test this hypothesis by substituting space for the time scenario. The method consists of

1. sampling the Yukon River and its tributaries along a gradient of permafrost conditions (Fig.1),
2. comparing the changes in elemental and isotopic values of these samples, and
3. using geostatistics and machine-learning to disentangle the role of permafrost in controlling spatiotemporal geochemical variations.

My work uses a combination of isotopic tracers, including strontium (Sr) and lithium (Li) isotopes, to assess weathering processes and sources in different permafrost cover conditions. The Sr isotope ratios ($^{87}Sr/^{86}Sr$) in rivers track the lithology exposed in the catchment. This tracer will be used in combination with elemental chemistry to assess spatiotemporal variations in weathering sources in different watersheds (Keller et al., 2010; Douglas et al., 2013). Li isotopes, which fractionate with secondary mineral formation, will be used to track the weathering

intensity of the active layer (Hindshaw et al., 2018). An increase in weathering intensity of the active layer in the catchment with lower permafrost cover should lead to an increase in the Li isotope ratio (δ^7Li) in rivers (Hindshaw et al., 2018). However, as topography, geology, climate and land cover can also influence weathering processes, these factors will have to be disentangled from the hydrochemical signals to isolate the role of permafrost.

This thesis is organized as a traditional monograph. First, I will review the literature detailing the current understanding of weathering processes in a permafrost-covered environment. Second, I will introduce the studied catchment detailing the hydrology and hydrochemistry of the Yukon River. Third, I will detail the sampling collection and analytical procedure, including the development of a new lithium isotope chromatography procedure. Fourth, I will describe the numerical and statistical approaches. Last, I will describe and discuss the results.

2. Literature Review

Chemical weathering by exporting alkalinity to the ocean regulates the long-term carbon cycle and long-term climate (Lawrence et al., 2012). When the climate warms, weathering intensifies, exporting more calcium to the ocean and favouring atmospheric CO_2 drawdown and climate cooling. Simple numerical models predict that the strength of this climate-weathering feedback is a function of erosion rates (Hijmans et al., 2005) with stronger feedback in rapidly eroding mountainous regions relative to low-relief areas. However, this model does not account for the role of glacial processes in controlling weathering rates. In particular, permafrost-covered areas (17% of the globe (Gruber, 2012; Biskaborn et al., 2019)) have very different hydrology and erosion regimes than other catchments from warmer climate zones. It has long been hypothesized that the presence of ice and permafrost could play a strong role in controlling the long-term climate by influencing both erosion and weathering (Zolkos et al., 2018). However, little is known about the impact of permafrost and glacial cover on weathering processes in high latitude catchments.

Weathering processes are strongly dependent on climate conditions. Temperature controls the kinetics of mineral dissolution reactions (Casey & Cheney, 1993; Hellmann, 1994; Chen & Brantley, 1997; Rosso & Rimstidt, 2000), and hydrology controls the rate of weathering and erosion (Berner, 1978; Lasaga et al., 1994; Steefel & Mäher, 2009; Maher, 2010). Climate change is exacerbated in northern regions, and as a result, weathering processes in northern regions are changing (Vincent et al., 2012). Arctic and boreal regions have experienced the fastest warming rates over the last decades (Post et al., 2019). The air temperature of northern latitudes increased by approximately ~0.05°C annually over the past three decades (Serreze et al., 2000; Striegl et al., 2005; Sturm et al., 2005), and the water discharge from the many major Arctic rivers is also increasing (Peterson et al., 2002; Striegl et al., 2005). Land cover changes are also happening with the Arctic shrubification, which increases soil acidity due to plant root respiration. These changes have broad consequences for weathering processes and hence on river water quality, ocean composition and carbon cycle dynamics. In this context, there is an urgent need to study the interactions of weathering processes in northern watersheds, particularly the impact of permafrost thawing.

2.1 Permafrost cover in high latitudes

One particularity of arctic and high-latitude landscapes is the presence of a permanently glaciated soil layer, called permafrost (Woo, 2012). Permafrost is a layer of rock, sediment or any other Earth material that has been frozen (below 0°C) for two or more years (Woo, 2012). Permafrost covers about a quarter of the northern hemisphere (Brown et al., 1997; Woo, 2012) and is increasingly present closer to the poles (Obu et al., 2019; Fig.2). Permafrost in the northern hemisphere presents a great variation in extent and depth (Zhang et al., 1999). Continuous permafrost occupies about half of the permafrost-covered land, with the remainder almost equally divided between discontinuous, sporadic and isolated patches (Obu et al., 2019). Only continuous permafrost is present around the north pole, and discontinuous permafrost, including sporadic and isolated patches, mostly occurs south of the Arctic circle. Permafrost distribution is directly associated with the mean annual ground and surface temperature. The average ground temperatures at the boundaries at continuous/discontinuous, at discontinuous/sporadic, and at sporadic/isolated-patches are -1.71 ± 0.48°C, -0.01 ± 0.37°C and 1.46 ± 0.44°C, respectively (Obu et al., 2019).

As warming accelerates in the northern latitudes, this permafrost layer has been progressively thawing over the past 30 years (Hinzman et al., 2005; Osterkamp, 2007; Romanovsky et al., 2010; Jorgenson et al., 2013) with considerable implications for terrestrial, wetland and freshwater ecosystems in northern watersheds.

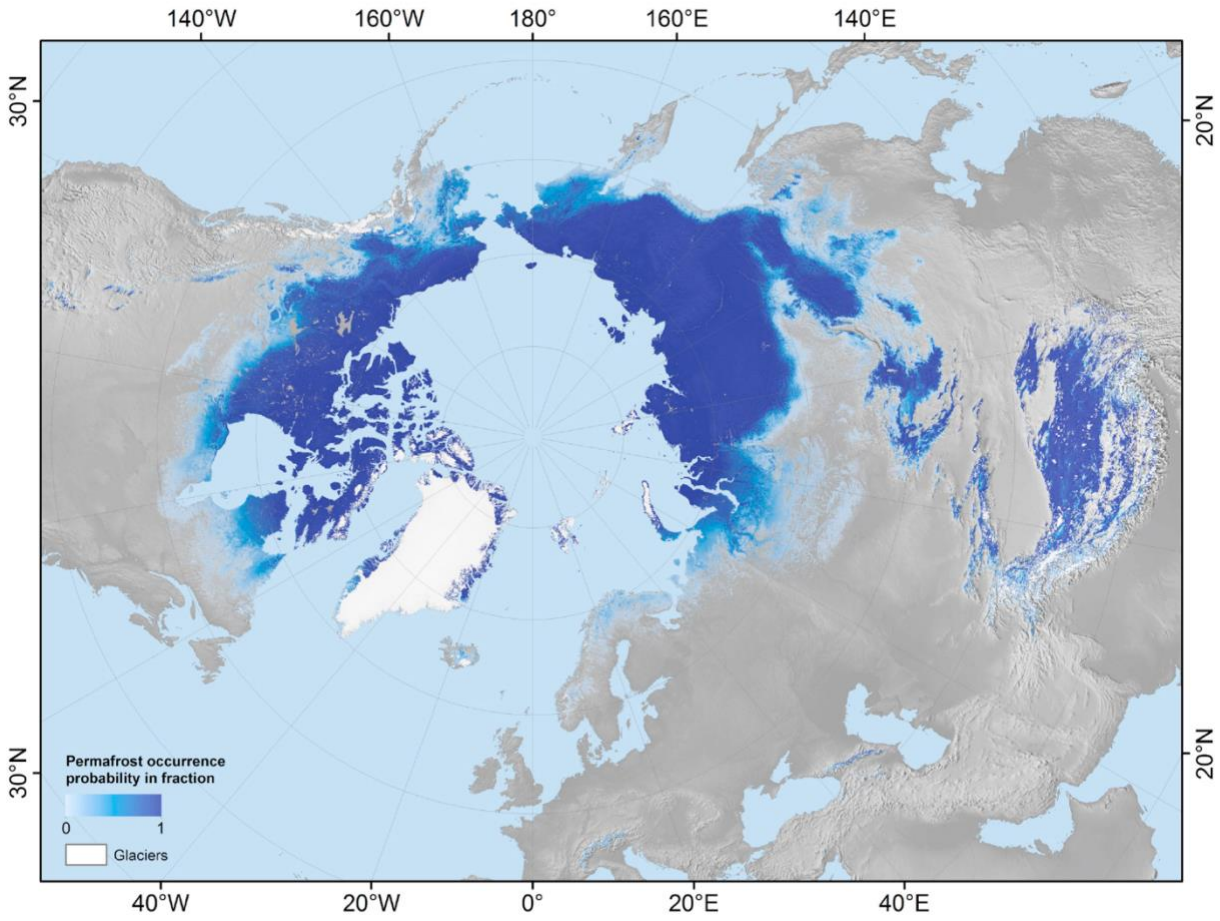

Figure 2: Calculated permafrost probability based on the fraction of the model run with mean annual ground temperature below 0°C (Obu et al., 2019). The permafrost probability is classified into continuous permafrost (>0.9), discontinuous permafrost (0.5-0.9), sporadic permafrost (0.1-0.5) and isolated patches (0.005-0.1).

2.2 Weathering processes in watersheds

Two weathering regimes endmembers exist on the Earth's surface: a transport-limited regime and a weathering-limited regime. In the transport-limited regime characteristic of flat areas of the Earth, erosion rates are low, allowing the formation of deep soils with high weathering intensity. In this weathering regime, the primary mineral availability is limited due to the low erosion rate. Primary minerals can dissolve and form secondary minerals (Sparks, 2003). If erosion rates become low enough, secondary mineral complete dissolution becomes the main contributor to weathering reactions, as is observed in some flat floodplains in tropical areas

(West et al., 2005). Conversely, in the weathering-limited regime more typical of mountain zones, high erosion rates remove weathered material rapidly downstream, preventing the accumulation of secondary minerals, resulting in lower secondary mineral formation rate relative to primary mineral dissolution (Stallard & Edmond, 1983; West et al., 2005). Between these two endmembers, weathering and erosion interactions lead to variable soil thickness and development (Stallard & Edmond, 1983; West et al., 2005; Murphy et al., 2019).

2.3 Weathering in northern watersheds

However, weathering and erosion processes in cold-climate regions and high-latitude watersheds differ from those of warm and wet watersheds in tropical and temperate regions. In northern latitude, physiographic characteristics of catchments depend on the permafrost distribution, permafrost thickness, and depth of the active layer, and these may play a primary role in controlling the hydrologic cycle, weathering and erosion processes (Hinzman et al., 2005; Lyon & Destouni, 2010). The hydrologic regimes in northern rivers are highly seasonal. In northern areas, most of the water falling on the catchment during the winter is accumulated as snow and ice (Derksen et al., 2012). In the winter, the river discharge and water-rock interactions are dominated by subsurface processes (i.e., baseflow). Baseflows of rivers underlined by continuous permafrost are low during the winter because continuous permafrost limits groundwater and surface water connectivity (Crites et al., 2020). Groundwater inputs usually occur at taliks, unfrozen zones in the permafrost, which provides a pathway between groundwater and surface water (Burn, 2002; Kokelj & Burn, 2005). In the spring, the stored water is discharged during the snowmelt creating a spike on the hydrograph called "Freshet." A large portion of freshet water is sourced from snowmelt and stored pre-melt water displaced through the organic layer to the stream during the melting season. Most of the runoff in northern rivers usually occurs from May to September, but the exact runoff timing differs depending on basins' characteristics (Ge et al., 2013). As the summer progresses, ice and snow continue to melt, and the layer above the permafrost progressively thaws (i.e., the active layer), allowing deeper infiltration of surface water (Woo, 2012). In the summer, deeper flow paths within the active layer combined with increased connectivity between surface and subsurface waters, lead to increase water-rock interactions. The river discharge becomes a combination of groundwater

inputs, surface runoff and shallow groundwater discharge. However, even during the summer, permafrost often acts as a semi-impermeable barrier between the active layer and deeper aquifers, limiting groundwater contribution (Xiao et al., 2020). Consequently, the majority of surface weathering processes in permafrost-dominated regions occur during summer within the seasonally thawed active layer until the water gets refrozen with decreasing air temperatures in the Fall.

2.4 Permafrost thawing and weathering in northern watersheds

With the accelerated warming of northern regions, permafrost cover is predicted to shrink rapidly over the next decades. Accelerated permafrost degradation due to climate warming will modify flow-paths and weathering processes in the north, thereby influencing the hydrochemistry of northern rivers (Frey & McClelland, 2009). Thawing of permafrost deepens the active layer and expose fresh primary minerals to weathering (Frey & McClelland, 2009). This increase in primary mineral availability could increase the silicate weathering rate with greater infiltration and water interactions with the freshly exposed primary minerals (Hilley & Porder, 2008). However, permafrost-covered soils are also regularly submitted to seasonal freeze and thaw cycles that promote high denudation rates (Murphy et al., 2019). These freeze and thaw cycles can enhance the availability of primary minerals favouring a higher weathering rate while preventing soils from forming. In addition, permafrost thawing can also facilitate higher connectivity between solute-rich groundwater and surface water, which can modify the hydrochemistry of rivers (Frey & McClelland, 2009). All these processes can concomitantly influence the hydrochemistry of northern rivers, making it challenging to predict the evolution of the northern river hydrochemistry.

As long-term climate warming of northern regions will likely continue and accelerate over the next century, it is critical to understand better weathering processes in these environments and how they will respond to warming. Although the connection between permafrost degradation and weathering processes is not fully understood (Pokrovsky et al., 2005; Frey et al., 2007; Frey & McClelland, 2009; Keller et al., 2010; Murphy et al., 2019), identifying the drivers of weathering in permafrost-covered regions would be critical to predict the impact of climate change to river water chemistry in northern watersheds. These hydrochemical changes

will likely have critical implications for the ecology and the sustainability of native and human communities living in the north. At a longer timescale, understanding how permafrost influences weathering processes will refine our understanding of global biogeochemical cycles in glacial times.

2.5 Lithium Isotopes

Studies have proved that constraining weathering processes in permafrost dominated regions is challenging because multiple processes such as biology, lithology and redox influence existing tracers (Pokrovsky et al., 2005; Frey et al., 2007; Frey & McClelland, 2009; Keller et al., 2010; Murphy et al., 2019). In this work, a combination of Li and Sr isotopes are used to understand weathering processes better. Li has two stable isotopes, ^{6}Li and ^{7}Li, with abundances of 7.5% and 92.5% (Coplen et al., 2002), respectively. The large relative mass difference (~17%) between the two isotopes allows wide fractionations of Li isotopes in various geological processes, including continental weathering (Liu & Rudnick, 2011), crustal recycling (Tang et al., 2014) and climate and tectonic evolution (Misra & Froelich, 2012). The Li isotope composition is the measured ratio of Li isotopes in an unknown sample normalized to that in the L-SVEC standard, usually expressed as δ^{7}Li with the following equation (Flesch et al., 1973):

$$\delta^{7}Li\ (‰) = \left[\frac{\left({}^{7}Li/{}_{6}Li\right)_{unknown} - \left({}^{7}Li/{}_{6}Li\right)_{standard}}{\left({}^{7}Li/{}_{6}Li\right)_{standard}} \times 1000\right] \ldots \text{Eq.1}$$

Li isotopes have great potential as a geochemical tracer for weathering processes in permafrost cover environments (Hindshaw et al., 2018). Li is a water-soluble element enriched in silicate rocks that greater than 90% of riverine Li is derived from silicate rock weathering (Kisakurek et al., 2005). The fractionation of Li isotopes occurs by chemical weathering during water-rock interactions (Huh et al., 1998; Pistiner & Henderson, 2003; Dellinger et al., 2015); however, neither primary basalt dissolution nor metamorphic dehydration is involved in the fractionation of Li isotopes (Pistiner & Henderson, 2003; Teng et al., 2007; Qiu et al., 2009; Wimpenny et al.,

2010). Li is only present in one redox state (+1 charge) and is, therefore, not influenced by redox reactions (Teng et al., 2007). Li is not a nutrient; hence, any biological processes do not significantly impact the Li isotopic compositions (Lemarchand et al., 2010; Pogge von Strandmann et al., 2012). Li fractionation occurs primarily during the secondary mineral formation where the ^{6}Li isotope is preferentially retained into the solid phase, and ^{7}Li remains in the residual solution (Huh et al., 2001; Pistiner & Henderson, 2003; Vigier et al., 2008; Pogge von Strandmann et al., 2010, 2016; Wimpenny et al., 2010; Hindshaw et al., 2018; Liu & Li, 2019). Several laboratory experimental studies have demonstrated that secondary mineral formation produces variable and potentially large isotopic fractionations, with preferential incorporating or adsorbing ^{6}Li onto the surface of secondary mineral (Starkey, 1982) or into octahedral sites in clay structure (Li & Liu, 2020) and leaving the equilibrium fluid enriched in ^{7}Li (Pistiner & Henderson, 2003; Williams & Hervig, 2005; Vigier et al., 2008; Wimpenny et al., 2015). The degree of fractionation (fractionation factor) between secondary mineral and fluid phase is expressed as α ($\delta^{7}\mathrm{Li}_{\mathrm{solid}} - \delta^{7}\mathrm{Li}_{\mathrm{solution}}$) varies depending on the mineral type and the temperature when the fractionation reaction occurs (Taylor & Urey, 1938; Wunder et al., 2006, 2007; Brenot et al., 2008; Wimpenny et al., 2015).

The fractionation factor between some secondary minerals and water from literature span a range from 0.984 to 1.000 are shown in Table 1. Williams & Hervig (2005) investigated isotopic fractionation during the transformation from smectite to illite, which turned out to be ~11‰ (α = 0.989 at 300°C). The fractionation in smectite increases systematically as a function of decreasing temperature, from 0.998 at 200-250°C to 0.990 at 90°C (Vigier et al., 2008). Pistiner & Henderson (2003) focused their Li isotopic fractionation experiments on sorption experiments of three secondary minerals, smectite, ferrihydrite and gibbsite, at room temperature (22°C) and concluded that the fractionation factor between mineral and fluid is 0.998 and 0.986 for ferrihydrite and gibbsite, respectively; and no Li isotope fractionation was observed between smectite and fluid. Hindshaw et al. (2019) investigated the synthesized Mg-rich layer silicates (stevensite and saponite) at high pH (9.0-10.4) and ambient temperature and concluded that the fractionation factor of Mg-rich layer silicates is 0.983. Li & Liu (2020) performed a series of experiments to estimate Li isotopic fractionation during sorption on kaolinite at ambient temperature (22°C) in three different settings; time series-, pH-, concentration-control settings and found that the fractionation factor of kaolinite is 0.992 for pH=8.5.

Table 1: Experimentally determined lithium isotopic fractionation between secondary mineral and water from the literature.

Mineral/fluid Fractionation Factors	**α**	**Starting solution [Li] (ppm)**	**T (°C)**	**pH**	**References**	**Notes**
Illite	0.989	1000	300		(Williams & Hervig, 2005)	
Smectite	0.983	20000	25		(Vigier et al., 2008)	
Smectite	0.990	20000	90		(Vigier et al., 2008)	
Smectite	0.997	20000	200 to 250		(Vigier et al., 2008)	
Smectite	1.000	0.5	22	7	(Pistiner & Henderson, 2003)	Sorption experiment
Ferrihydrite	0.998	0.5	22	7	(Pistiner & Henderson, 2003)	Sorption experiment
Gibbsite	0.986	0.5	22	7	(Pistiner & Henderson, 2003)	Sorption experiment
Gibbsite	0.984	56000	25	7	(Wimpenny et al., 2015)	
Stevensite	0.983	13.9	20	9.0-10.4	(Hindshaw et al., 2019)	
Saponite	0.983	7.9	20	9.5	(Hindshaw et al., 2019)	
Kaolinite	0.992	3	22	8.5	(Li & Liu, 2020)	Sorption experiment

2.6 Lithium isotope variability in the river at the global scale

In river basins, δ^7Li of river water range from +2‰ to +44‰ and is always higher than that of the source bedrock or suspended sediments (Huh et al., 1998, 2001; Kisakurek et al., 2005; Pogge von Strandmann et al., 2016, 2017, 2006, 2010, 2012; Vigier et al., 2008; Wimpenny et al., 2010; Lemarchand et al., 2010; Witherow et al., 2010; Rad et al., 2013; Dellinger et al., 2015; Pogge von Strandmann & Henderson, 2015; Murphy et al., 2019). δ^7Li

variations in the river have been used to better understand weathering processes at the local to the global scale. δ^7Li values in a river are controlled by the ratio that has been described as "silicate weathering congruency" that is defined by the ratio of the primary mineral dissolution relative to the secondary mineral formation (Misra & Froelich, 2012; Pogge von Strandmann & Henderson, 2015; Vigier & Goddéris, 2015; Pogge von Strandmann et al., 2016, 2017; Murphy et al., 2019). The dissolution process of primary mineral (crustal δ^7Li of ~0‰ to +5‰) does not cause any fractionation (Pistiner & Henderson, 2003; Vigier et al., 2008; Wimpenny et al., 2010; Dellinger et al., 2015) but releases unfractionated Li (Pistiner & Henderson, 2003; Vigier et al., 2008; Wimpenny et al., 2010; Murphy et al., 2019). Fractionation during the secondary clay formation incorporates ^{6}Li onto the surface of clay or into a structural lattice and results in increasing δ^7Li of the solution (Pistiner & Henderson, 2003; Vigier et al., 2008; Wimpenny et al., 2010; Murphy et al., 2019). The interactions of weathering, erosion and climate at the global scale lead to a broad range of δ^7Li in rivers of more than 30 ‰. The Ganges, Lena and river draining basalt terrains have a similar δ^7Li mean (~ 23‰) (Huh et al., 1998; Murphy et al., 2019), whereas the Amazon, the Mackenzie and rivers draining the high Himalayas have lower δ^7Li mean values (~15‰).

δ^7Li values often vary as much within a watershed than at the global scale because δ^7Li values reflect the interplay of erosion and weathering processes within the river basin. In the headwaters, where the erosion rate is very high, weathering intensity is low (weathering-limited regimes) and usually coincides with low dissolved δ^7Li values with high dissolved Li fluxes. Conversely, close to the mouth of the river, where sediments accumulate, the fluvial system becomes transport-limited and is characterized by higher weathering intensity. These regions display low dissolved δ^7Li, similar to the weathering-limited regimes (Dellinger et al., 2015). The region with the highest weathering intensity is generally between these two extremes in alluvial plains or flood plains, where erosion rate remains high, but the weathering reaction has the time to proceed (Fig.3). Consequently, many rivers in a tropical and temperate setting display a bell-shaped relationship between δ^7Li and dissolved Li concentration, as seen in the Amazon (Dellinger et al., 2015; Fig.4A)

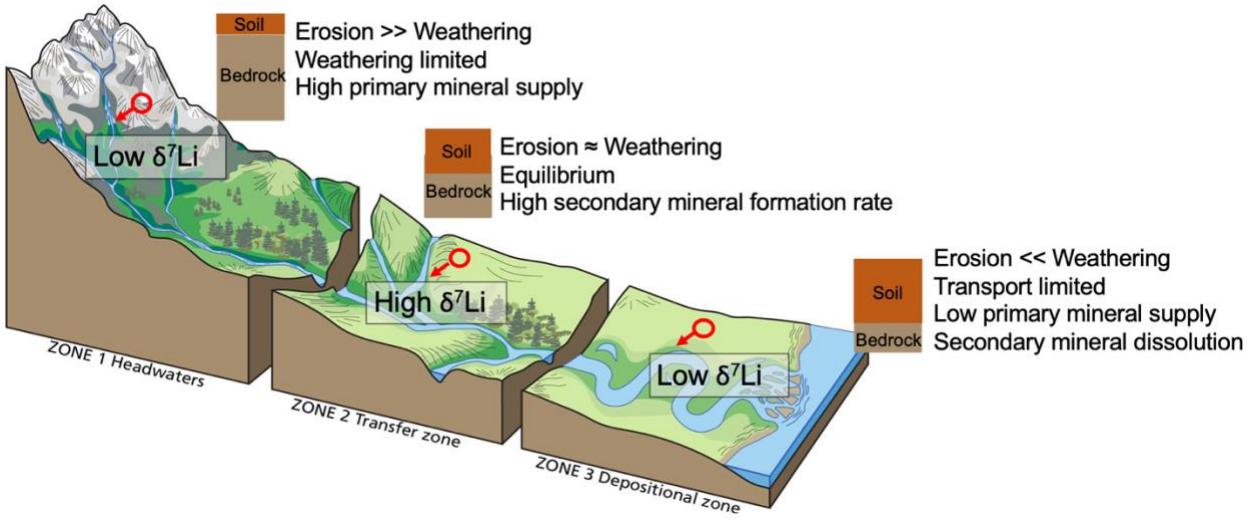

Figure 3: Conceptual model of theoretical δ^7Li values variations within a watershed profile (modified from Trista L. Thornberry-Ehrlich, Colorado State University).

2.7 Lithium isotope variability in the Arctic rivers

As mentioned above, weathering reactions are temperature dependent; consequently, weathering processes tend to be slower in northern watersheds relative to tropical regions. However, in high-latitude regions, glacial processes can also influence weathering and erosion processes. A few studies have explored δ^7Li variability in high-latitude watersheds, including the Mackenzie River Basin, the Lena River and other Siberian rivers. The permafrost cover in these watersheds ranges from 75% to 90%. The variations of riverine δ^7Li values are still large in these northern watersheds with a range of 9.3‰ to 29.0‰ in the Mackenzie River Basin (Millot et al., 2010), 7.1‰ to 41.9‰ in the Lena River Basin (Murphy et al., 2019), and 3.9‰ to 23.7‰ in the Siberian rivers (Huh et al., 1998). δ^7Li can also vary seasonally in norther regions, possibly informing about seasonal changes in weathering processes. Hindshaw et al. (2019) showed that a 4‰ seasonal range occurs in the Yenisei River in Siberia. They suggested that the samples collected in winter represent the winter flow predominantly sourced from the reservoirs (neighbouring lakes), allowing long residence time and elevated clay formation. In contrast, the samples collected in spring had short water residences with increased discharge and, therefore, less clay formation. The relationship between δ^7Li and Li concentrations in the Arctic river reflects a similar sort of interplay between erosion and weathering as those observed in tropical

catchments (Fig.4A). However, in the northern latitudes, weathering reactions tend to be slower due to low temperatures (Millot et al., 2003), and erosion is generally high due to glacial processes (Hallet et al., 1996). Consequently, northern watersheds are unlikely to reach a fully "transport limited" regime as is observed in the Amazon floodplains with the dissolution of secondary minerals. Ultimately, the dissolved δ^7Li in the northern river does not display a parabolic relationship as in tropical watersheds (Dellinger et al., 2015; Fig.4A) but only shows a broad positive correlation with the inverse of dissolved Li concentrations (Murphy et al., 2019; Fig.4B). Northern rivers display only "weathering limited" regimes where the erosion rates are high, but the rates of secondary mineral formation are low because of limited weathering reactions. Therefore, the Arctic rivers display increasing riverine δ^7Li values with decreasing dissolved Li concentrations (Murphy et al., 2019; Fig.4B)

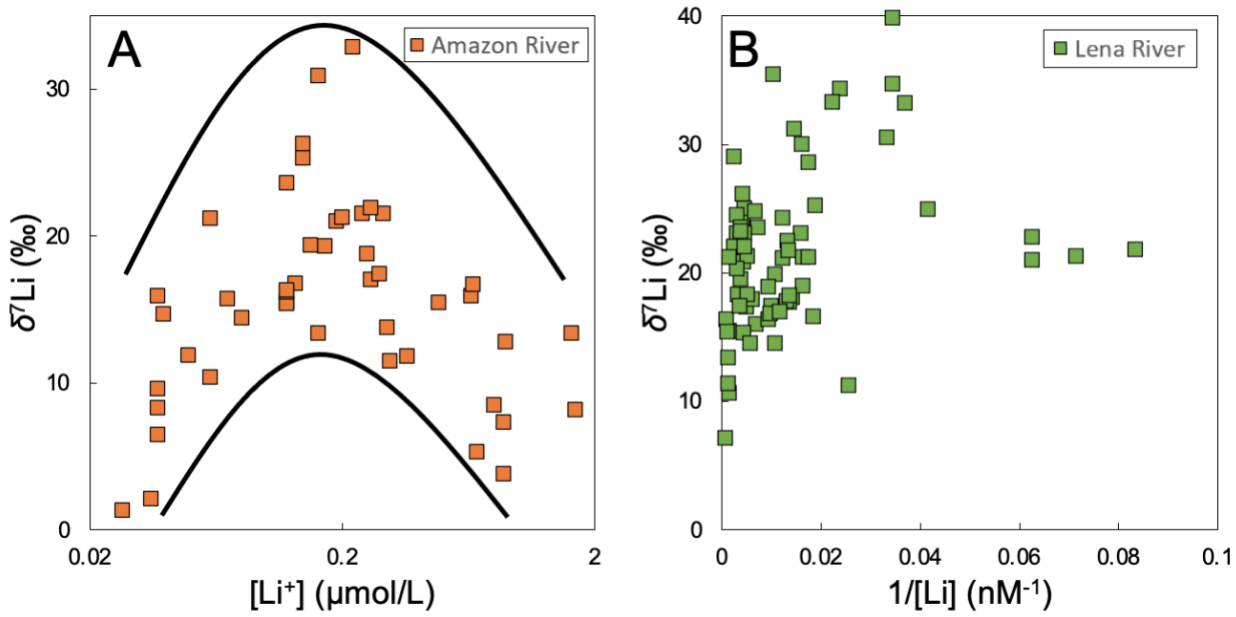

Figure 4: (A) the riverine δ^7Li values plotted against the dissolved Li concentrations in the Amazon River (Dellinger et al., 2015). (B) the riverine δ^7Li values plotted against the inverse of dissolved Li concentrations in the Lena River (Murphy et al., 2019).

2.8 Strontium isotope in rivers

Strontium (Sr) has four stable isotopes, ^{88}Sr, ^{87}Sr, ^{86}Sr and ^{86}Sr, with their relative abundances of 82.53%, 7.04%, 9.87% and 0.56%, respectively, while only the fraction of ^{87}Sr increases with time due to the decay of rubidium isotope, ^{87}Rb (Capo et al., 1998). The $^{87}Sr/^{86}Sr$ has become a significant geochemistry tool to trace the source of weathering in watersheds as biological processes, or low-temperature geochemical reactions are not involved in the fractionation (Capo et al., 1998). $^{87}Sr/^{86}Sr$ variability in river usually reflects that of the rocks weathering on the catchment. However, as different rocks do not weather at the same rate and do not have the same Sr abundances, their contribution to the river Sr flux varies (Bataille & Bowen, 2012). Studies have shown that the riverine $^{87}Sr/^{86}Sr$ variability often results from mixing two endmembers: carbonates and silicates (Brass, 1976; Wadleigh et al., 1985; Palmer & Edmond, 1989, 1992). Silicate rocks tend to have low Sr concentrations but a broad range of $^{87}Sr/^{86}Sr$ ratios depending on their age and lithology (Capo et al., 1998; Bentley, 2006). Silicates are also more resistant to weathering and cover larger Earth's surface areas than carbonates (Dürr et al., 2005). Conversely, carbonates have higher Sr concentrations, less variable and lower $^{87}Sr/^{86}Sr$ ratios (0.707-0.709) and are much more rapidly weathered. Consequently, rivers draining old cratonic areas have higher $^{87}Sr/^{86}Sr$ ratios than rivers draining young volcanic rocks, but carbonate dissolution always buffers the $^{87}Sr/^{86}Sr$ of rivers relative to their underlying rocks.

2.9 Strontium isotope variability in the Arctic rivers

As mentioned earlier, the $^{87}Sr/^{86}Sr$ ratios in rivers are highly dependent on the age of the rock and lithology exposed to the catchment. In most tropical and temperate rivers, $^{87}Sr/^{86}Sr$ are relatively constant through time and track the contribution of different rock units weathering on the catchment. However, in high-latitude rivers, the seasonal variation of $^{87}Sr/^{86}Sr$ ratios can occur due to large changes in water sources to river discharge. For example, the Chena River Basin, underlined by the discontinuous permafrost, displays some large seasonal $^{87}Sr/^{86}Sr$ variations (Douglas et al., 2013). $^{87}Sr/^{86}Sr$ ratios in the Chena River Basin are lowest during winter baseflow, and $^{87}Sr/^{86}Sr$ ratios increase in spring and summer. The groundwater base flows reflect the $^{87}Sr/^{86}Sr$ of subsurface rocks in the winter since the soil profiles are frozen. The thawing of permafrost occurs as the spring comes, the active layer starts deepening, and

carbonate minerals in the active layer start to weather, decreasing $^{87}Sr/^{86}Sr$. Similarly, the Yenisei River in Siberia displays some large seasonal $^{87}Sr/^{86}Sr$ variations caused by the seasonally varying proportions of runoff (Bagard et al., 2011; Mavromatis et al., 2016; Hindshaw et al., 2019)

2.10 Combining strontium and lithium isotopes to reconstruct weathering

When used together with major and trace elements, Sr and Li isotopes have great potential to refine our understanding of weathering processes. Li is concentrated in silicate rocks, while Sr is primarily concentrated in carbonate rocks. Unfractionated Li released from silicate rocks have almost identical δ^7Li to its parent rock, but it is highly fractionated during the interaction with the fluid. Variations in δ^7Li allow tracing silicate weathering intensity occurring on a catchment, whereas the Sr isotopes provide lithological information on weathering sources.

3. The Yukon River

All the samples collected in this work are focused on the Yukon River Basin. In this thesis, I aim to understand if permafrost cover has an influence on lithium isotope variations and weathering processes occurring on the Yukon River. The Yukon River Basin is covered with varying degrees of permafrost, providing a great setting to test the hypothesis of this thesis. However, as mentioned above, many environmental and geological factors can influence weathering. Disentangling these processes and identifying their impacts on hydrochemical data is critical to properly identifying the role of permafrost cover. In this section, I will review the hydrological, topographic, geological, climatological and permafrost cover conditions on the Yukon River to set the stage for hydrochemical data interpretation.

3.1 The Yukon River Geography

The Yukon River is approximately 3,200 km long, draining an area of more than 850,000 km^2 covering part of northwest Canada and central Alaska (Brabets et al., 2000). The Llewellyn Glacier, near Atlin lake, in northwestern British Columbia, is the source of the Yukon River (Parfit, 1998; Brabets et al., 2000). From this point, the Yukon River flows northwestward to the Canada/Alaska boundary, then begins to flow westward and finally discharges to the Bering Sea. The Yukon River headwaters are located on moderately high rugged mountainous regions, while the downstream parts of the river are primarily lower mountains, plains and lowlands. The Yukon River Basin can be subdivided into 13 basins, eight major tributaries to the Yukon River and five lowland areas that drain directly into the Yukon River (U.S. Geological Survey, 1987; Brabets et al., 2000). In general, the contributions of water discharge from the basin are proportional to the basin's size (Brabets et al., 2000; Fig.5). However, the presence of glaciers that store a large amount of water can lead to higher contributions from rivers draining alpine glaciers. For example, the Tanana River and the White River in the northern basin are two glacier-fed rivers that contribute 29% of the Yukon River's total water flow but only account for 19% of the Yukon River Basin. Conversely, rivers underlined by continuous permafrost, such as the Porcupine River or the Koyukuk River, tend to contribute less discharge proportionally to their surface.

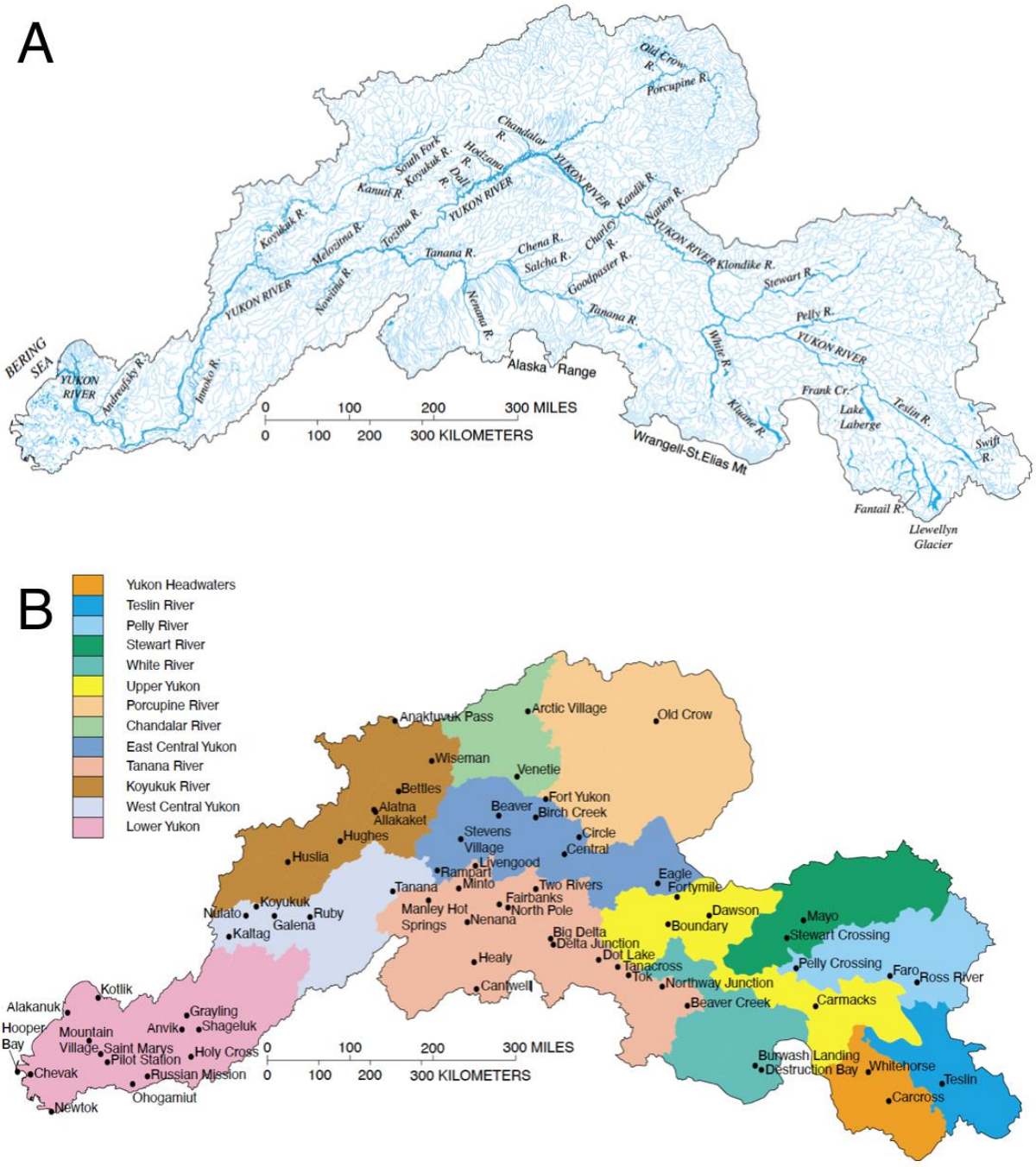

Figure 5: (A) Rivers and glaciers of the Yukon River Basin (Brabets et al., 2000) and (B) Major drainage basins in the Yukon River Basin (Brabets et al., 2000).

As mentioned earlier, topography controls erosion rate and exerts a direct influence on weathering intensity and lithium isotope variations (Figure 3). The topography of the Yukon

River can be classified into five different physiographic regions (Wahrhaftig & Nolan, 1965; Bostock, 1970; Brabets et al., 2000; Fig.6). The Alaska Range and the Wrangell-Saint Elias Mountains, located south-central part of the basin, are high altitude, highly rugged, largely glaciated mountains with high erosion rates. Other lower altitudes and unglaciated mountain ranges are also part of the Yukon River Basin, including the Central and Eastern Brooks Range and the Ogilvie Mountains. The eastern part of the Brooks Range, located in the northern part of the Yukon River Basin, is partly glaciated. The Ogilvie Mountains are unglaciated and located near the Yukon River headwaters. They are underlain by discontinuous permafrost, but glaciers are not present. A large portion of the Yukon River Basin is dominated by rolling topography with gentle slopes such as the Yukon-Tanana Upland and the Porcupine Plateau. The entire upland is covered by discontinuous permafrost, while the Porcupine Plateau located in the northern basin is underlain by continuous permafrost. Low mountains, plains and lowlands are mostly located in the central and lower portion of the basin. The Porcupine River flows into the Yukon River through the Yukon Flats, which form an outwash fan by braided rivers in the northern part and flat floodplains in other areas. Most of the tributaries in this region surrounding uplands and mountains have meandering courses drained by the Yukon River. Streams and rivers in the central and lower basin flow to the Yukon River, and the Yukon River drain the Flats in this area.

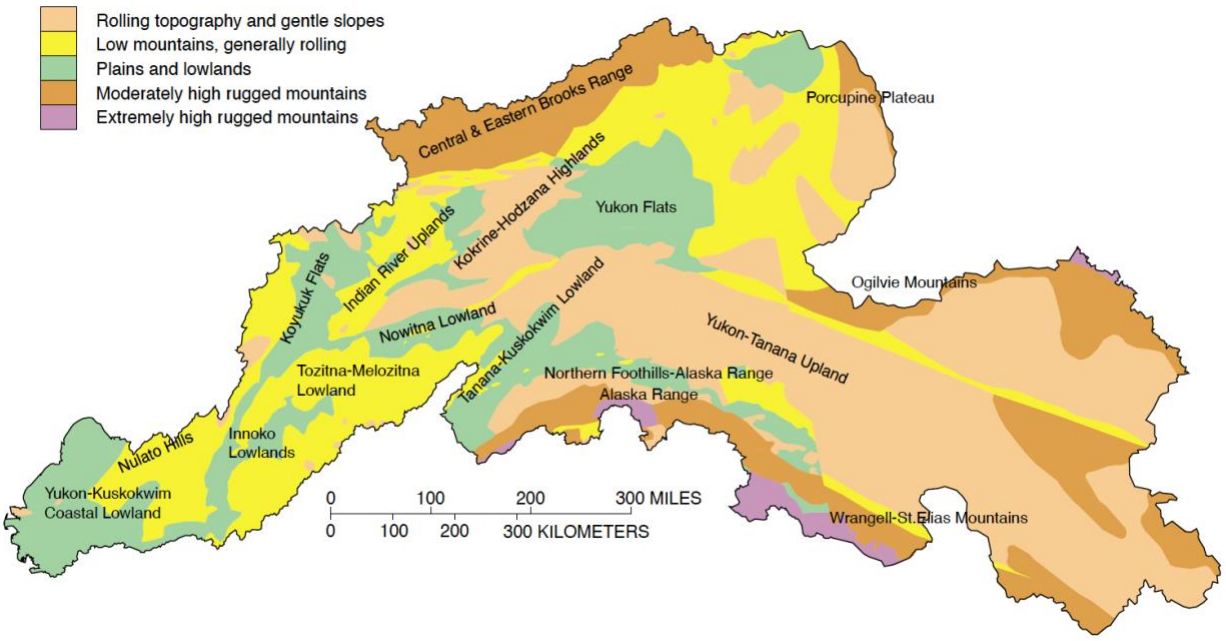

Figure 6: Physiographic regions of the Yukon River Basin (Wahrhaftig & Nolan, 1965; Bostock, 1970; Brabets et al., 2000).

3.2 The Yukon River Geology

Lithology is also an important control of weathering processes as different rock types erode and weather at different rates (Eby, 2004). The chemical weathering of rocks occurring over the drainage basin is the main source of the river dissolved and suspended loads. The Yukon River Basin is a large, multi-lithological basin, including unconsolidated deposits and consolidated rocks ranging from Precambrian to Holocene in age (Brabets et al., 2000). Due to the complexity of the geology in the Yukon River Basin, the rock types are combined into four major rock types; siliciclastic sediments, carbonate sediments, volcanic rocks and metamorphic rocks (Fig.7). The geology of the headwater of the Yukon River is more complex than other regions and is composed of Cenozoic volcanic rocks, siliciclastic sediments and locally Paleozoic metamorphic rocks and carbonate sediments. As the river flows westward towards the Alaska border, the geology becomes primarily composed of Mesozoic metamorphic and partially Cenozoic volcanic rocks. The Yukon-Tanana Terrane, mostly composed of metamorphic rocks (Fig.7), is bounded by the Tintina Fault to the north and the Denali Fault to the south. The Denali Fault separates Paleozoic metamorphic rocks in the north (Yukon-Tanana Terrane) from the

younger volcanic terrane of the south (Cenozoic or Mesozoic in age) (Brabets et al., 2000; Brennan et al., 2014). In the northern part of the Yukon River Basin, the Porcupine River catchment is composed primarily of Paleozoic siliciclastic and carbonate sediments and locally Paleozoic volcanic rocks. The western part of the Yukon River Basin is primarily underlain by both Mesozoic siliciclastic and carbonate sediments and locally Mesozoic volcanic rocks. The Koyukuk Flat is mainly composed of Cenozoic volcanic and volcaniclastic sediments. The Lower Yukon is composed up of mostly Mesozoic to Cenozoic siliciclastic sediments and locally Cenozoic volcanic rocks.

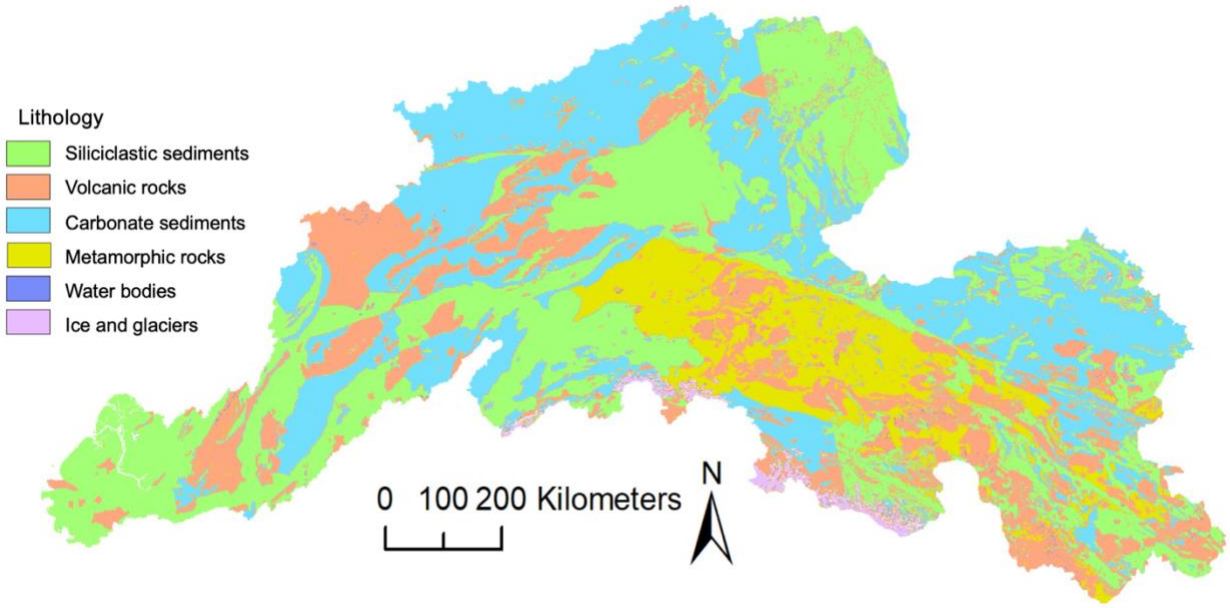

Figure 7: The geology of the Yukon River Basin. Geology ranging from Precambrian to Cenozoic are summarized into the same major rock types and categorized into siliciclastic, carbonate sediments, volcanic and metamorphic rock.

3.3 Soil property in the Yukon River

Soil property is another critical control of the chemical weathering process. Young soils, rich in primary minerals, tend to have a higher secondary mineral formation rate and contribute higher elemental fluxes to rivers. Deep and weathered soils are richer in secondary minerals and

shield bedrock from surface weathering reactions though they might contribute to deeper flow paths and enhanced surface and sub-surface interactions. The chemistry and development of soils, and their contribution to elemental flux to rivers, are strongly influenced by the chemical composition of the parent rocks and other soil-forming factors (Jenny, 1994).

The Yukon River Basin is dominated by cryosols (Brabets et al., 2000; Fig.8), a mineral or organic soil with perennially frozen material within 1 m of the surface. The organic soil acts as an insulator for the frozen soil layer below during the summer. In the northern watersheds, the soil cryoturbation, the mixing and distortion of the soil horizons, is generated by seasonal freeze-thaw (Scudder, 1997), and it is suggested that the cryoturbation has been active since deglaciation (Zoltai and Tarnocai, 1974; Zoltai et al., 1978; Scudder, 1997)

Brunisols dominate the headwater and its surrounding regions of the Yukon River. Brunisols are characterized by their weakly developed subsoil layer, and two groups of brunisols are found in the Yukon River Basin; dystric brunisols and eutric brunisols (Brabets et al., 2000). Most of the brunisoils found in the headwater regions are eutric brunisols, which have a less than 5 cm thick horizon composed of organic matter and minerals and are not strongly acidic (Scudder, 1997). The other type of brunisoils, dystric brunisols, which are found in high mountainous regions surrounding the headwater region, are similar to eutric brunisols but lack a well-developed topsoil horizon and strongly acidic (Scudder, 1997). Regosols are recently formed soils that lack a horizon development and are found locally at the Yukon Flats and valley bottoms of the Yukon River (Scudder, 1997; Brabets et al., 2000). Rock outcrop areas on rough mountainous land lack soil development.

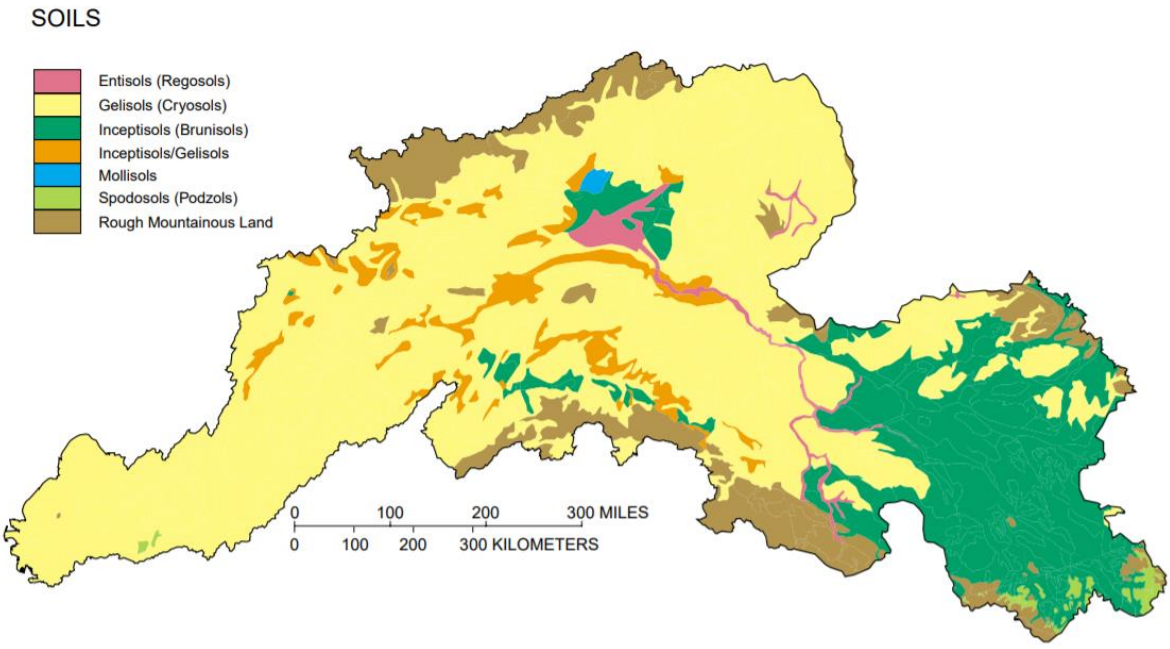

Figure 8: The soil types on the Yukon River (Brabets et al., 2000).

3.4 The Yukon River Climate and Hydrology

Climate is an important weathering control (Jenny, 1994; Rasmussen et al., 2011; Molina et al., 2019) as temperature and precipitation influence the weathering rates and the kinetic of weathering reaction (White & Blum, 1995). Chemical weathering reactions are enhanced with increasing temperature and rainfall (Grotzinger and Jordan, 2014). The climate of the Yukon River is very varied due to its large size and range in altitude of the land surfaces (Searby, 1968; Hartman & Johnson, 1978; Brabets et al., 2000). The mean annual temperature varies spatially between -6.3 °C and 1.5 °C, with colder temperatures in the north and high-altitude regions and warmer temperatures in the south and coastal setting (Obu et al., 2019; Fig.9). Temperature amplitude is also larger in the more continental portion of the Yukon River Basin than in coastal regions (Brabets et al., 2000).

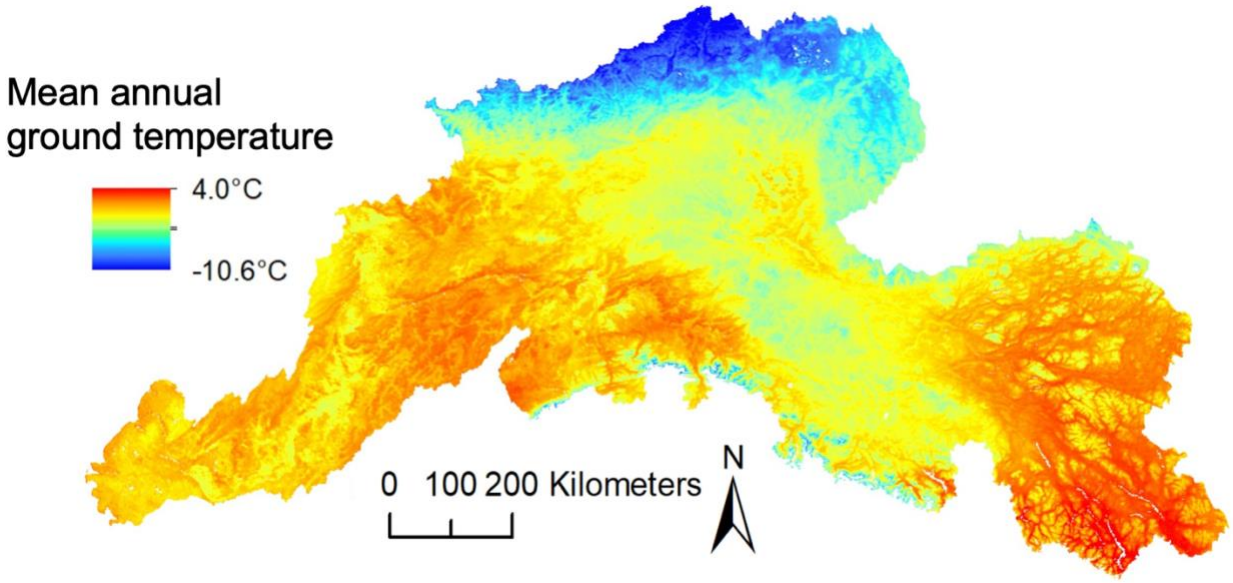

Figure 9: The mean annual ground temperature at the top of permafrost clipped for the Yukon River Basin from (Obu et al., 2019).

Annual precipitation ranges from 25 cm to 330 cm as a mix of snow and rainfall, with the amount of precipitation being related to topography and distance from the coast; mountainous regions, particularly the Alaska Range, receive a larger amount of precipitation than lowland areas (Brabets et al., 2000; Fig.10). Most of the Yukon River Basin received little precipitation because the Alaska Range constitutes a barrier to moisture transport inland. Most of the precipitation falls in the form of snow in the high mountainous regions and accumulates in alpine glaciers (Brabets et al., 2000). The mean annual precipitation in the Alaska Range peaks at approximately 200 cm, and the snowfall is estimated at 1020 cm, whereas in most of the lowlands, the average annual precipitation is approximately 38 cm, and snowfall ranges from 150 to 300 cm.

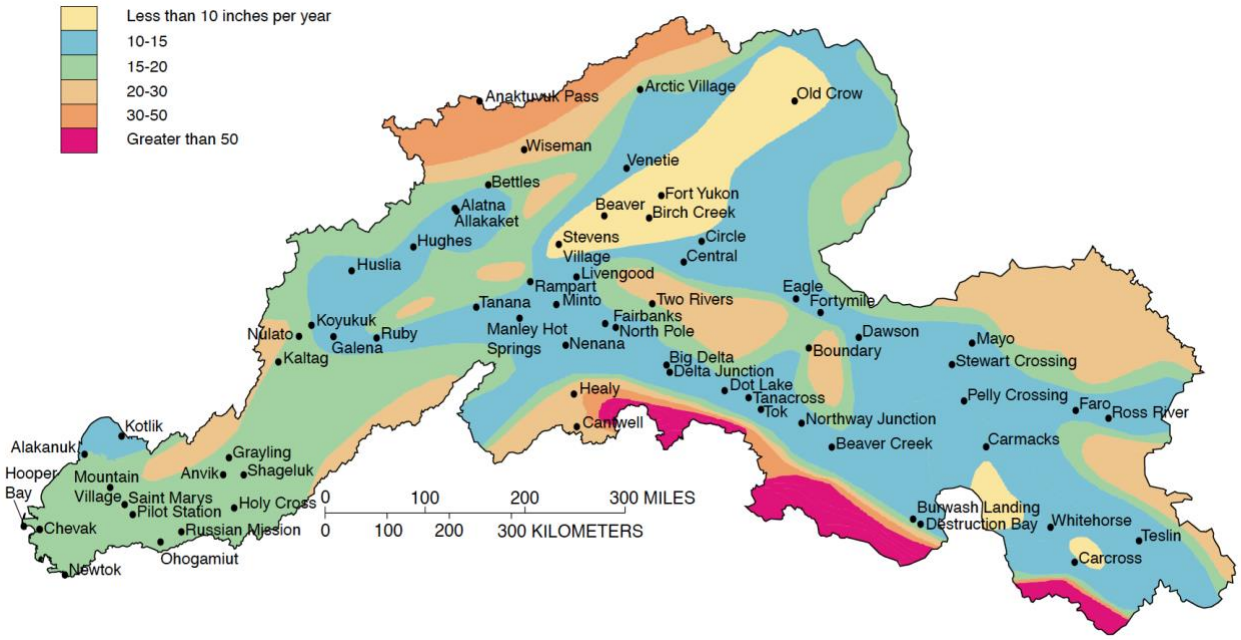

Figure 10: Mean annual precipitation across the Yukon River Basin (Jones & Fahl, 1994; Brabets et al., 2000).

In the Yukon River Basin, streamflow generally decreases from October to late April, and most runoff usually occurs from May to September; however, the exact runoff timing varies depending on the basin characteristics (Brabets et al., 2000). The variations of average discharge are large between locations (Brabets et al., 2000; Fig.11), but they all show a typical glacial river hydrograph. There are three runoff patterns exhibited: lake runoff, snowmelt runoff and glacier-runoff (Brabets et al., 2000). Lakes are filled with precipitations such as snowmelt and rainfall, and once filled, lake runoff begins with the highest discharges occurring in August and September. Both snowmelt and glacier runoff begin in June from snowmelt, but unlike snowmelt, which almost stops contributing during the summer, glacier melt is sustained throughout the summer. Most of the rivers in the headwaters of the Yukon River exhibit lake runoff pattern, only two rivers display glacier runoff patterns (the Tanana and White Rivers), and the remaining of the rivers exhibit snowmelt runoff patterns. The Porcupine, Chalandar and Koyukuk Rivers are distinguished from other snowmelt-runoff rivers as the baseflows of these rivers are very low during the winter. This is likely due to the headwaters of these rivers being

underlain by continuous permafrost, limiting groundwater inflow by acting as a barrier (Brabets et al., 2000).

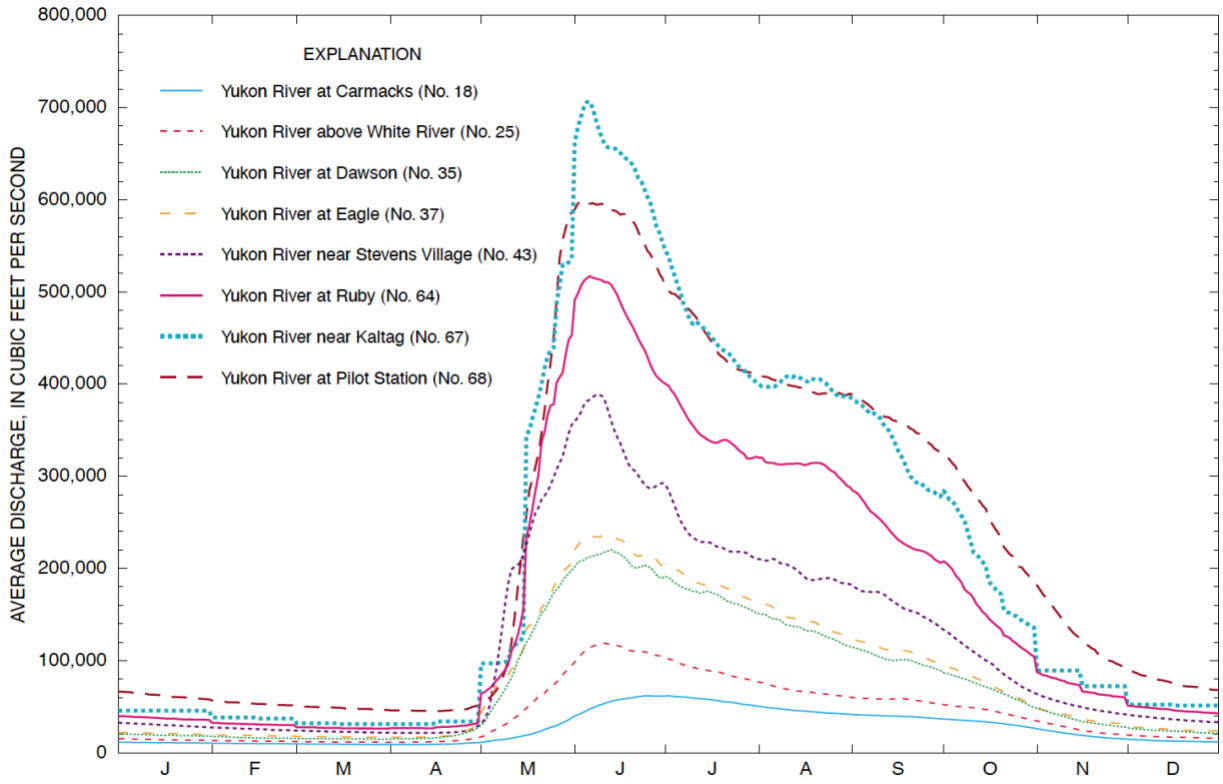

Figure 11: The average water discharge of the Yukon River at eight locations (Brabets et al., 2000).

The Yukon River Basin can be divided into different permafrost zones (Obu et al., 2019): continuous permafrost, discontinuous permafrost, sporadic permafrost and isolated patches. Isolated patches of permafrost underlie the headwater of the Yukon River (Obu et al., 2019; Fig.12). Continuous permafrost lies in the northern part of the basin, including the Central and Eastern Brooks Range and the Porcupine Plateau and locally on the Yukon-Tanana Upland and the Yukon Flats. Discontinuous permafrost primarily lies in the surrounding areas of the Yukon-Tanana Upland, and the Yukon Flats underlain by continuous permafrost. The west-central basin is mostly underlain by sporadic and isolated permafrost, while primarily sporadic to discontinues

but locally continuous permafrost lies in the Koyukuk Flats and the Lower Yukon drainage basin.

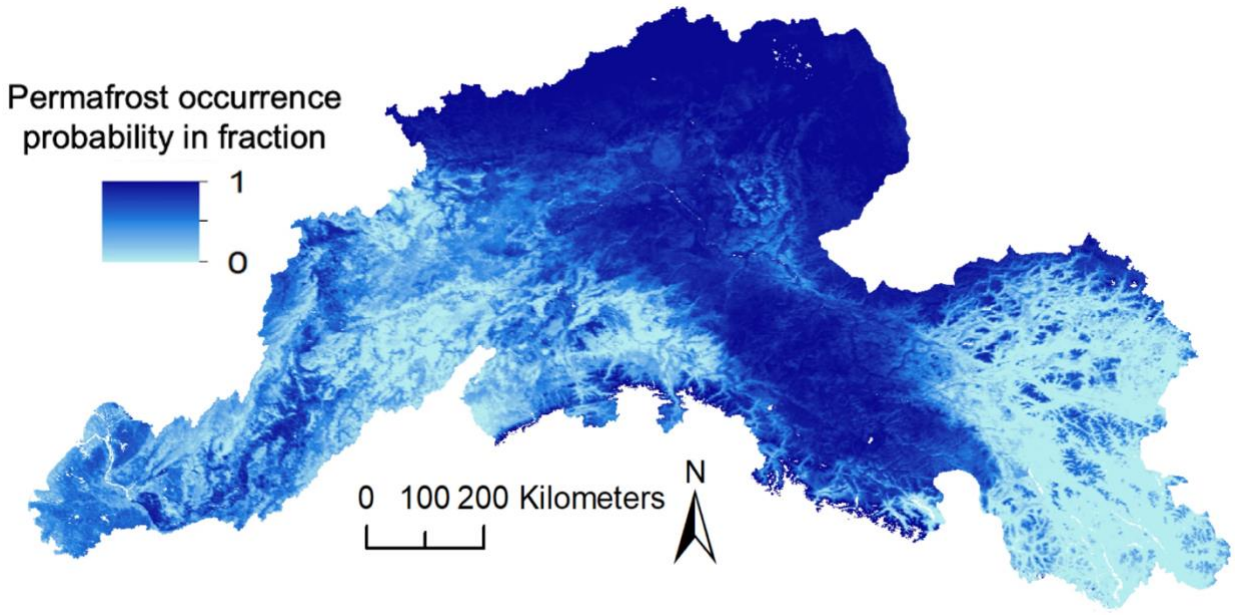

Figure 12: Calculated permafrost probability based on the fraction of the model run with mean annual ground temperature below 0°C clipped for the Yukon River Basin from (Obu et al., 2019). The permafrost probability is classified into continuous permafrost (navy), discontinuous permafrost (blue), sporadic permafrost (lighter blue) and isolated patches (sky blue).

3.5 Climate Warming and Hydrochemical Changes on the Yukon River

The annual flow in the Yukon River Basin has remained relatively constant since the 1950s but with potentially an increased groundwater contribution to surface waters (Walvoord & Striegl, 2007; Brabets & Walvoord, 2009; Ge et al., 2013; Toohey et al., 2016). A decreased groundwater storage was observed between 2002 and 2008 within the Yukon River Basin (Muskett & Romanovsky, 2011; Toohey et al., 2016). The warming is thought to increase groundwater input to rivers by enhancing permafrost thawing and facilitating the connectivity between shallow groundwater and surface water (Walvoord & Striegl, 2007). In the winter, taliks also provide a pathway to some supra-permafrost groundwater flow to the river (Woo, 2012),

and some studies have hypothesized that the taliks may contribute to the increased groundwater contribution within the Yukon River Basin (Zhang et al., 1999; Muskett & Romanovsky, 2011; Walvoord et al., 2012; Toohey et al., 2016).

The changes in water discharge (Striegl et al., 2005) and solute fluxes of organic matter, nutrients and major ions (Frey & McClelland, 2009) have a significant effect on terrestrial ecosystems. The ongoing warming also accelerates the degree of permafrost thawing (Hinzman et al., 2005; Osterkamp, 2007; Romanovsky et al., 2010; Jorgenson et al., 2013). Thawing of permafrost deepens the active layer that thaws and freezes seasonally above the permafrost and exposes fresh primary minerals (Frey & McClelland, 2009). The accelerated degradation of permafrost due to climate warming exposes solute-rich permafrost that may contribute to increasing solute to streams and rivers (Kokelj & Burn, 2005; Frey & McClelland, 2009). Toohey et al. (2016) observed a significant increase in solute concentrations of nutrients over the last three decades within the Yukon River Basin. While these increased annual fluxes are observed during the summer as expected, there are significantly increased fluxes during the fall and winter river flows, suggesting deepening of the active layer, enhanced weathering, and increased sulphide oxidation (Toohey et al., 2016).

4. Sampling and Analytical Methodology

The river water samples for this study collected from mid-July to early September of 2016, 2017, and 2018 when the active layer of soil profiles deepens at its maximum and represents the maximum surface weathering rate on the basin. River water samples were collected to cover a range of permafrost covers across the Yukon River Basin (Fig.13). The river water samples were collected during similar periods to minimize seasonal variations in weathering. This will allow us to investigate how Li and Sr isotopes change as a function of permafrost distribution probability and how the degradation of permafrost influences weathering processes.

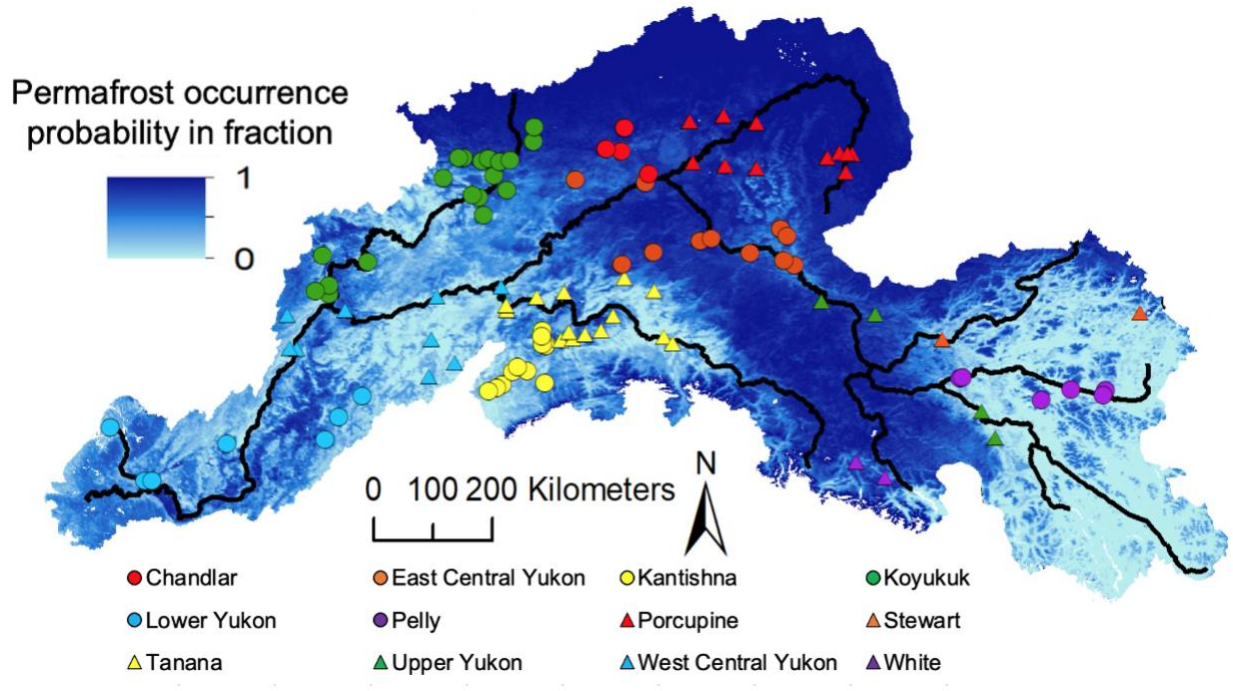

Figure 13: The locations of the collected river water samples (bright green) on different permafrost distribution displayed from dark (permafrost-dominated) to light colour (no permafrost) across the Yukon River Basin. The black line represents the main stem of the Yukon River and its principal tributaries.

Most of the samples used for this study have been collected by the late Dr. Brennan and a network of collaborators and volunteers established by Dr. Bataille and Dr. Brennan. The rationale for the sampling locations included a compromise between gathering enough samples with a variety of permafrost cover and cost considerations associated with the accessibility of the sampling sites. Locations of sampling were accessed either by car, by plane or by helicopter. At each sample site, water was collected upstream of the collector in acid-washed 250 ml low-density polyethylene (LDPE) wide-mouth bottles, which were rinsed three times with sample water. Within 48 hours of collection, each sample was filtered through a 0.45 µm Luerlock syringe filter (polypropylene membrane) using a 50 cm^3 polypropylene syringe into a clean acid-washed 125ml LDPE narrow-mouth bottle. Within a maximum of 16 days of collection, samples were acidified with 2 ml ultra-pure concentrated HNO_3 (BDH Aristar Ultra). To evaluate consistency in field collection methods, 15% of the samples were collected as field triplicates. To evaluate any field-related contamination, regular blanks were collected in the field using the same steps described above for samples, but by using NANOpure de-ionized water (type I, 18.0 MΩ) (Barnstead, NANOpure Diamond).

4.1 Elemental analyses

The concentrations of major and trace elements in river water samples were quantified through inductively coupled plasma mass spectrometry (ICP-MS) at the Department of Geology and Geophysics ICPMS laboratory at the University of Utah using an Agilent 7500ce ICPMS and the Department of Earth and Environmental Sciences at the University of Ottawa using an Agilent 8800 triple quadrupole mass spectrometer.

At the University of Utah, the river water samples were diluted 4:1 with 2.4% ultra-pure HNO_3, and 25 ng/mL of indium was added as an internal standard for ICP-MS analysis. The external standard of the USGS standard reference sample, T-205, was measured after every five samples to check the consistency of the analysis.

At the University of Ottawa, calibration standards for Li and Na were prepared using single element certified standards purchased from SCP Science (Montreal, Canada). The 1 ppb checking standard was measured every ten samples throughout the run to account for any instrument drift. After the Li purification of river water samples, the aliquots of reconstituted

samples in 2% TraceMetal™ Grade HNO_3 were analyzed on ICP-MS at the University of Ottawa's Geochemistry Laboratory to check Li recovery before Li isotope measurements.

4.2 Sr isotope analyses

The river water preparation for Sr analysis took place at the Department of Geology and Geophysics ICPMS laboratory at the University of Utah and the University of Ottawa. In both cases, the analysis was performed using a Thermo Scientific™ Neptune™ high-resolution multi-collector inductively coupled plasma mass spectrometer (MC-ICP-MS; Thermo Fisher Scientific, Bremen, Germany).

At the University of Utah, prior to the Sr isotope analysis, purification of Sr in the water sample was conducted through an inline chromatographic column packed with a Sr-specific crown ether resin(Mackey & Fernande, 2011; Brennan et al., 2014). Samples were acidified to 4 M HNO_3. A set volume of the sample is transported into a 2mL coiled PTFE tube. A vacuum is the motive force during the sample uptake that switches to a peri-pump, and the sample is transferred into a column filled with the crown ether resin. The crown ether resin has a higher affinity for Sr than other alkali and alkali earth metals at high HNO_3 concentration (≥4 M), allowing to minimize the ^{87}Rb isobaric interference on ^{87}Sr and Sr is eluted out from the resin at a lower HNO_3 concentration (0.04 M) (Horwitz et al., 1992; Brennan et al., 2014). The solution with eluted Sr in 0.04 M is directly used for Sr isotope analysis into the MC-ICP-MS. Samples containing the lowest Sr concentrations to progressively higher concentrations were sequenced during the ICP-MS analysis to avoid potential memory effects.

At the University of Ottawa, the separation of Sr was processed in 100 µL microcolumn loaded with Sr-spec Resin™ (100–150 µm; Eichrom Technologies, LLC). The matrix was rinsed out using 6 M HNO_3. The Sr was collected with 0.05 M HNO_3. After separation, the eluates were dried and re-dissolved in 200 µL 2% v/v HNO_3 for $^{87}Sr/^{86}Sr$ analysis. Sample solutions in 2% v/v HNO_3 were introduced using a micro*FAST* MC single-loop system (Elemental Scientific). The loading volume was 200 µL, and the injecting rate was 30 µL/min.

At both the University of Ottawa and the University of Utah, the solution was aspirated using a PFA nebulizer, a double-pass quartz spray chamber, quartz torch, and nickel sample and

skimmer cones. Isotopes ^{82}Kr, ^{83}Kr, ^{84}Sr, ^{85}Rb, ^{86}Sr, ^{87}Sr, and ^{88}Sr were simultaneously measured in L4, L3, L2, L1, C, H1, and H2 Faraday cups, respectively. Measurements of samples were made using a static multi-collector routine that consisted of one block of 75 cycles with an integration time of 4.194 s/cycle. ^{84}Sr and ^{86}Sr have isobaric interferences from ^{84}Kr and ^{86}Kr, respectively. ^{87}Sr has an isobaric interference from ^{87}Rb. The interferences of ^{84}Sr and ^{86}Sr were corrected by subtracting the amount of ^{84}Kr and ^{86}Kr corresponding to the ^{83}Kr signal. The interference of ^{87}Sr was corrected by subtracting the amount of ^{87}Rb corresponding to the ^{85}Rb signal. Instrumental mass fractionation was corrected by normalizing $^{86}Sr/^{88}Sr$ to 0.1194 using the exponential law. Strontium isotope compositions are reported as $^{87}Sr/^{86}Sr$ ratios. At the University of Utah, the long-term reproducibility of the $^{87}Sr/^{86}Sr$ measurement of NIST SRM987 with ~6V intensity of 88Sr is 0.710287 ± 0.000025 (2SD).

At the University of Ottawa, the long-term reproducibility of the $^{87}Sr/^{86}Sr$ measurement for NIST SRM987 is 0.71025 ± 0.00004 (1SD, n = 16). A 100 ng/g pure Sr standard was measured along with the sample as the in-house standard (0.70823 ± 0.00005, 1SD, n = 4). The long-term reproducibility of the in-house standard is (0.70822 ± 0.00004, 1SD, n = 106).

4.3 Li isotope analyses

The purification of Li in the river water sample was performed in an ISO-100 clean lab at the University of Ottawa. The volume of each river water sample was calculated to obtain at least 80 ng of Li. The calculated volume of each sample was then dried completely on a heating plate at 100°C in Teflon beakers. The residue was dissolved in 1 ml of HNO_3 to digest organic matter remaining and placed on a heating plate with the cap closed for a day. Samples were dried and re-dissolved in 2 ml of 0.18 N HCl for column chromatography. The re-dissolved samples should be clear or a pale colour without any floating matter at this point.

For Li purification, we developed a novel in-house Savilex column chromatography that is detailed in the following section. Briefly, the Savillex columns were filled with 2.9 ml of the pre-cleaned cation-exchange resin, Dowex 50W-X8 (200-400 mesh size), and were washed thoroughly by passing through 15 ml 6N HCl, followed by 15 mL Milli-Q water. Columns were then conditioned using 10 ml 0.18 N HCl. The re-dissolved prepared samples were loaded onto the columns. After passing through 14 ml 0.18 N HCl, the Li-elution was collected with 18.5 ml

of 0.18 N HCl. In this study, two standards, IAPSO and Syn-1, were prepared with the same sample preparation protocol to ensure consistency of column chromatography. Blanks were also run to ensure there was no contamination during the procedure. The Li-elution was dried completely on a heating hotplate at 100°C and was reconstituted in 4.2 ml 2% HNO_3. Prior to Li isotope measurements, aliquots of before and after the Li-elution and 0.2 ml of the reconstituted Li-elution were analyzed on ICP-MS at the University of Ottawa's Geochemistry Laboratory to ensure 100% Li recovery. The total procedural blanks were not detectable (<0.005 ng Li), insignificantly relative to the 80 ng of Li analyzed in each sample and suggested there was no contamination during the column chromatography. The highest Na/Li mass ratio in the Li-elution of all river water samples in this study was 1.7. Based on previous studies, Na/Li mass ratio inferior to 3 should not lead to a decrease in the accuracy and precision of the δ^7Li measurements (Liu and Li, 2019).

The δ^7Li of river water samples was measured on an MC-ICP-MS (Neptune Plus) at the Geological Survey of Canada using a standard-bracketing method with L-SVEC as the standard (Fig.14). The measurements were performed using solution nebulization in the "wet plasma" mode. The sample solution was aspirated using a double pass spray chamber, H-type sample and X-type Skimmer cone to achieve high sensitivity. Isotopes of ^{6}Li and ^{7}Li were measured in L4, and H4 Faraday cups, respectively, and the mass of 6.5041 was set in the central Faraday cup, C. Li isotope measurement consists of one block with 40 cycles of 4.174 s integration time. The instrumental mass bias was corrected through the standard-bracketing method. The analytical sequence was repeated in this order; blank, standard, blank, sample, blank, standard, blank, sample, blank. The washing time between each analysis was 140 s using 2% HNO_3 to minimize the memory effect. The Li isotopic composition was calculated with Eq. 1 and reported in δ^7Li notation (Flesch et al., 1973). The accuracy and external reproducibility were determined from repeat measurements (n = 33) of IAPSO, which yielded δ^7Li = 31.10 ± 0.68‰, over a period of 8 months, which agrees with the reported IAPSO δ^7Li values (Brand et al., 2014). The long-term reproducibility of the δ^7Li for the L-SVEC solutions were -0.002 ± 0.31‰ (n = 106), which is in good agreement with the reported L-SVEC values of 0.003 ± 0.09‰ (Magna et al., 2006).

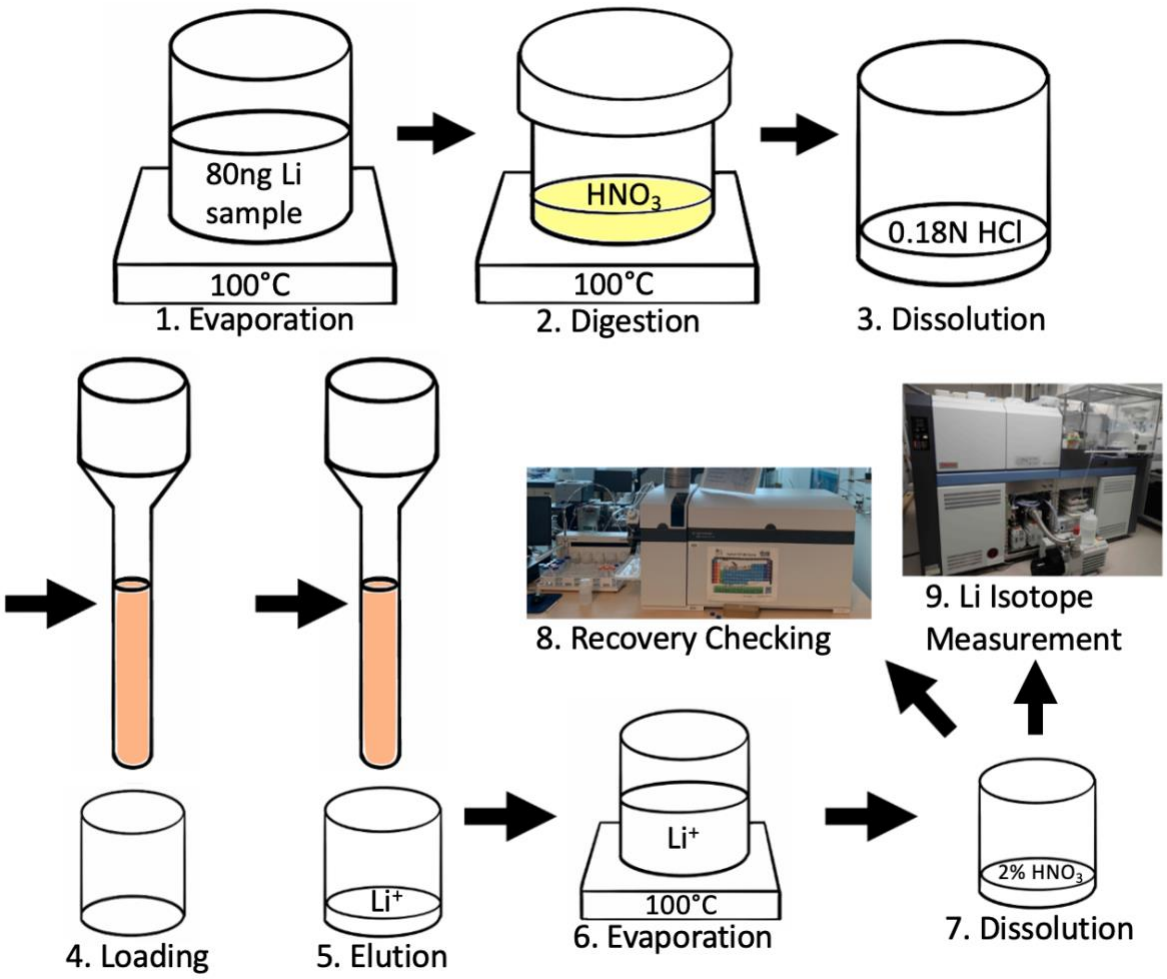

Figure 14: Schematic summarizing the procedure to analyze Li isotopes from river.

4.4 Watershed delineation

We used GIS methods to link the stream geochemistry with the environmental and geological conditions on the drainage catchment. In a first step, we delineated the Yukon River Basin and its subbasins from a 61 m resolution digital elevation model (DEM). We used the Spatial Tools for the analysis of River Systems (STARS) (Peterson, 2015).

The constructed landscape network (LSN) geodatabase contains spatial context and relationships (Theobald et al., 2006; Peterson, 2015) and features such as nodes, edges and Reach Catchment Areas (RCAs) (Theobald et al., 2005; Peterson, 2015). Nodes display topologic stream breaks such as confluences and stream sources. Edges are flow paths from one

node to another. RCAs represent the smallest edge-matching interbasin unit over the watershed. Before calculating the environmental and geological attributes for each sampled catchment, the sample locations must be correctly positioned on the LSN. We used the "Snap Points to Landscape Network" in STARS to incorporate point features (sample location) into the LSN (Theobald et al., 2006; Peterson, 2015). A point feature "site" was incorporated in the LSN geodatabase after this process. Prior to calculating the site catchment attributes, all sample locations were verified on Google Earth. Often imprecision on DEM leads to incorrect LSN or incorrect placement of rivers. We used the latitude and longitude of each site as well as Google Earth to compare the constructed LSN with the actual river flow path from satellite data. In most cases, the sites were located correctly on the LSN, but the sites were snapped on different rivers for a few sites. These points were manually replaced on the proper position on the LSN.

Using the constructed LSN geodatabase incorporating our sampled site, we could calculate the accumulated hydrological, environmental and geological characteristics at any location on the watershed. To summarize the environmental and geological conditions on each sampled catchment, we compiled a dataset of open-access geospatial data from the literature (Table 2). The selected raster files were re-projected into the same coordinate system as the DEM raster file (NAD_1983_Alaska_Albers) and then clipped to the size of the study area. Briefly, each resampled covariate raster file was first incorporated into the RCA attribute calculation using "Zonal Statistics as Table" from the STARS tool. Zonal Statistics output an attribute table that contains the minimum, maximum, mean and sum of the specific summarized covariate over the RCA area. We incorporated this statistic table into the LSN geodatabase for each of the RCA the sub-. We then accumulated downstream the sum of each summarized covariate in RCAs using the "Accumulation Values Downstream" tool in STARS. Each accumulated covariate value was finally used to calculate the average statistics over the series of sampled watersheds (sample locations) "Watershed Attributes" tool in STARS. The output from this step provided a table that summarized the average value of one given covariate for the catchment corresponding to each sampled location. We repeated this process for each of the covariates to obtain a table summarizing the geological, climatological and environmental conditions on each of the sampled watersheds (Fig.15).

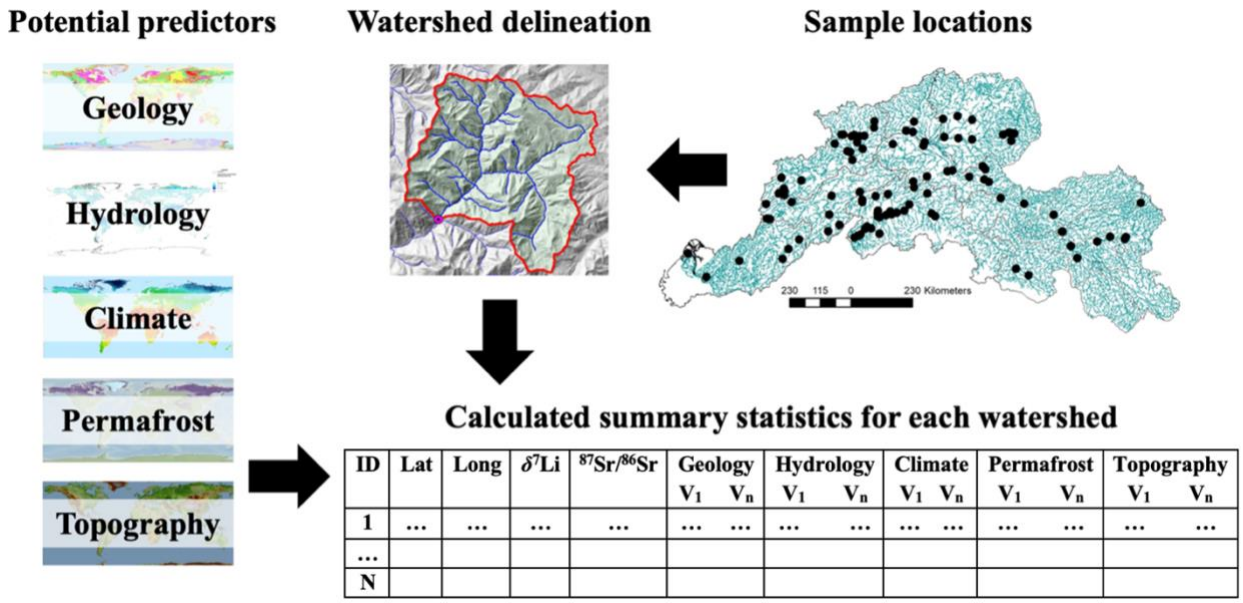

ID	Lat	Long	δ^7Li	^{87}Sr/^{86}Sr	Geology		Hydrology		Climate		Permafrost		Topography	
					V_1	V_n	V_1	V_n	V_1	V_n	V_1	V_n	V_1	V_n
1	…	…	…	…	…	…	…	…	…	…	…	…	…	…
…														
N														

Figure 15: A summarized GIS workflow to calculate environmental predictors on each sampled catchment.

Table 2: List of geological, climate, environmental variables used for statistics (C = Continuous; D = Discrete).

Variables	Description	Transformation	Resolution	Type	Source
r.perp	Permafrost distribution probability		1 km	C	(Obu et al., 2019)
r.magt	Mean annual ground temperature		1 km	C	(Obu et al., 2019)
r.mat	Mean air temperature		30-arc sec	C	(Hijmans et al., 2005)
r.ph	Soil pH in H_2O solution		250 m	C	(Hengl et al., 2017)
r.clay	Clay (weight %)		250 m	C	(Hengl et al., 2017)
r.cec	Cation exchange capacity		250 m	C	(Hengl et al., 2017)
r.orc	Soil organic carbon (weight %)		250 m	C	(Hengl et al., 2017)
r.bouguer	WGM2012_Bouguer		2 min	C	(Hengl et al., 2017)
r.pet	Global Potential Evapo-Transpiration		30 arc	C	(Zomer et al., 2008)
r.salt	Community Climate System Model 3 simulation	Log	1.4° x 1.4°	C	(Mahowald et al., 2006)
r.elevation	Shuttle Radar Topography Mission		90 m	C	(Jarvis et al., 2008)
r.xx	GLiM 1st lithological class attribute		1 km	D	(Hartmann & Moosdorf, 2012; Bataille et al., 2018)
r.litho	GLiM 2nd lithological class attribute		1 km	D	(Hartmann & Moosdorf, 2012; Bataille et al., 2018)
lgm	LGM Glaciation Extends		125 m	C	(Ehlers & Gibbard, 2007)
glacier	Global Land Ice Measurements from Space		30 m	C	(RGI Consortium, 2017)

4.5 Statistical Analysis

The statistical analyses and figures were computed using R programming language version Rx64 3.6.2 (https://www.r-project.org/) using R studio.

As we collected a fairly large hydrochemical dataset with environmental covariates, we first then used Principle Component Analysis (PCA) to reduce the dimensionality of the dataset. PCA is a statistical method used for a multivariate dataset, summarizing the interrelation of the dataset in a bivariate plot with the axis of two greatest variances (PC1 and PC2). We first used PCA between isotope measurements and molar element ratios to summarize hydrochemical variables. We then used PCA between isotope measurements and geological, climatic and environmental predictors.

We then used linear regression to assess the relationship between environmental covariates, geochemical values and isotopic values at each site. In particular, we plotted the riverine δ^7Li values against molar element ratios, geological, environmental, and climatic predictors to understand which variable might influence δ^7Li variations and hence weathering processes. Linear regression is a simple analysis method used to explain a relationship between two variables. A relationship is explained with a best-fitting straight line through the points on a bivariate plot called a regression line, which minimizes the sum of squared prediction errors. The prediction errors are squared because the prediction can be either above or below the regression line.

Once we had summarized and identified the key relationship between variables, we developed a multivariate random forest regression. Random forest regression is a machine-learning algorithm consisting of many decision trees trained by bootstrap sampling and random feature selection. A random subset of the dataset is entered, and then the original dataset is split by each predictor into smaller and smaller sets at nodes in the decision tree. Bootstrapping is a sampling technique that allows the sampling selection procedure completely random with replacements to prevent overfitting, constructing an ensemble of multiple decision trees. The results of each decision tree undergo aggregation to predict the mean value of the responsive variable. In this study, the compiled database (Table 2) was incorporated into the random forest regression to predict riverine δ^7Li variability following the framework developed by Bataille et al. (2018) and the caret package (Kuhn, 2008).

Random forest regression models were optimized using root mean squared error (RMSE) as the primary metric and a 10-fold repeated cross-validation scheme with 5 repetitions in our approach. The VSURF package was used to perform variable selection (Genuer et al., 2015). Once the model is optimized, the relationships between the selected predictors and predicted δ^7Li values were described using variable importance purity measure and partial dependence plots.

5. Lithium Column Chemistry Development

5.1 Need for Lithium isotope chromatography

A prerequisite to analyze Li isotopes on the Yukon River samples is to have a reliable column chromatography method.

In this thesis, we use an MC-ICP-MS instrument to analyze the Li isotope composition in our samples. The method to analyze Li isotope composition using MC-ICP-MS analysis is based on standard bracketing procedure. This procedure has been adopted as the method of choice by the community to analyze the Li isotope composition of different types of material (Tomascak et al., 1999; Bryant et al., 2003). The sample-standard bracketing (SSB) method is the correction method widely used to deal with the problem of instrumental mass discrimination (Albarède et al., 2004; Mason et al., 2004; Pietruszka & Reznik, 2008; Petit et al., 2008; Yang et al., 2009). It is suitable for Li isotopic analysis because Li has only two stable isotopes. The SSB method measures the isotope ratio of the analyte element in standard solutions (L-SVEC in this case) before and after analyzing unknown samples. The isotopic ratio of the standard is known, and the correction factor for the unknown sample is determined with the standards. The value is applied to calculate the isotopic ratio in the sample. The Li isotopic ratios are reported in δ^7Li notation (Flesch et al., 1973) and are calculated with Eq.1.

However, SSB analysis is challenging because the plasma is very sensitive to the matrix effect, causing significant instrumental mass-dependent isotope fractionation due to the space-charge effect from the ionization of non-analytes (Košler et al., 2001; Bryant et al., 2003). To avoid such interferences, Li needs to be purified and fully isolated from sample matrices. Gravity column chromatography has been successfully used to separate Li from other elements, particularly sodium (Na), in a sample matrix (Huang et al., 2010). However, 100% recovery of sample Li is required to avoid isotope fractionation in the column matrix. Early attempts to isolate Li from geological materials required three or four separate column procedures (Moriguti & Nakamura, 1998; James & Palmer, 2000; Rudnick et al., 2004; Teng et al., 2006; Liu et al., 2010). These approaches are time-consuming and generally require a large volume of eluents, thus increasing the risk of contamination. This is particularly challenging because Li isotopic data from common reagents show a huge range of variations (Qi et al., 1997), increasing the potential for contamination (Košler & Magna, 2013). Moreover, incomplete Li recovery in any

of these steps will lead to isotopic fractionation (Misra & Froelich, 2009). Consequently, many research groups have developed their own Li isotope chemistry (Tomascak et al., 1999; Nishio & Nakai, 2002; Jeffcoate et al., 2004; Rosner et al., 2007; Huang et al., 2010; Gao & Casey, 2012; Choi et al., 2013; Van Hoecke et al., 2015; Lin et al., 2019).

During the column chromatography, Li^+ and Na^+ elute out while other cations such as Fe^{3+}, Al^{3+} are retained by the resin. This is because alkali cations have low ionic potential with low partition coefficients compared to others (Liu & Li, 2019). These separation techniques vary in their protocol and reagents, but to achieve satisfactory lithium vs. matrix elements separation, relatively large resin loads, high aspect ratios and large eluent volumes are required. A large volume of resin is required because lithium is usually present at trace level and require a large volume of sample (e.g., 0.001 to 0.020 mg/L in freshwater (Emery et al., 1981; Huh et al., 1998; Ayotte et al., 2011; Kavanagh et al., 2017) and 0.14 to 0.20 mg/L in seawater (Riley & Tongudai, 1964; Angino & Billings, 1966; Kavanagh et al., 2017). A high aspect ratio is required to separate Li from Na because these two cations are monovalent and behave similarly with the chromatographic resins. Large eluent volumes are required because the recovery of Li should be nearly 100% to avoid any fractionation during chromatography. Existing procedures have varied greatly, with dual columns being the most common method with a first path separating Li from the cationic matrix and a second path to separate Li from Na more specifically. Na, which is the most common matrix element, may cause matrix interference during the Li isotope analysis due to a similar distribution coefficient between Li and Na. δ^7Li can be decreased by up to 3‰ (Nishio & Nakai, 2002; Jeffcoate et al., 2004; Liu & Li, 2019) and increased by ~ 1‰ (Bryant et al., 2003; Li et al., 2019; Liu & Li, 2019) due to Matrix-induced mass interference.

Among the technique used, some methods use inorganic eluents including hydrochloric acid (HCl), nitric acid (HNO_3) and hydrofluoric acid (HF) combined with organic solvents such as methanol (Tomascak et al., 1999; Nishio & Nakai, 2002; Jeffcoate et al., 2004; Rosner et al., 2007; Huang et al., 2010; Choi et al., 2013; Phan et al., 2016; Bohlin et al., 2018; Lin et al., 2019). The use of HF is particularly common and limits the applicability of Li chromatography to experience geochemists due to the significant hazard associated with HF (Kirkpatrick et al., 1995). While Tomascak et al. (2016) have suggested that adding methanol or ethanol to eluent provides better separation of Li from matrix elements than inorganic eluents, (Li et al., 2019)

demonstrated that this method had significant disadvantages, including (1) decreased eluent composition due to fast volatilization of methanol which may cause drifting of elution curves (Ai et al., 2014; Li et al., 2019) (2) decreased air solubility due to rapid evaporation of methanol (Swann et al., 1983; Li et al., 2019) and air bubbles formed during evaporation may disturb the compact resin structure, and (3) organic solvent stimulates resin degradation which can lead to drifting of Li and Na peaks (Jeffcoate et al., 2004; Li et al., 2019). Consequently, other chromatographic methods attempted to remove the need for organic solvents with varied success (Misra & Froelich, 2009; Gao & Casey, 2012; Van Hoecke et al., 2015).

Developing a fast, precise and reliable single-column system that can be used for multiple types of material remained challenging. In particular, the need for high aspect-ratio and a high amount of resin usually lead to slow elution rates resulting in 7–10 h separation procedures (Rudnick et al., 2004; Van Hoecke et al., 2015; Phan et al., 2016; Lin et al., 2019). The efficiency of one-column systems must be better tested, and potentially, the use of multiple solvents and dangerous acids should be avoided. The challenge with single column chromatography is that different material has very different matrices, and this matrix might modify the elution curve of Li isotope in a column and require column re-calibration (Moriguti & Nakamura, 1998; Chan et al., 1999; Chan et al., 2002; Van Hoecke et al., 2015; Tomascak et al., 2016; Bohlin et al., 2018). Additionally, for samples with very little Li content, the single-column method may not be sufficient, and therefore individually calibrated separation protocols are required to achieve complete removal of matrix elements and full recovery of Li during chromatography (Van Hoecke et al., 2015; Phan et al., 2016; Tomascak et al., 2016). For example, Van Hoecke et al. (2015) developed separate single-column systems for carbonates and clays.

We aim to develop a safe and efficient single-column chromatography protocol to purify Li prior to Li isotopic analysis. More specifically, we aim to develop a protocol safer than previously established by exclusively using diluted weak acid (HCl or HNO_3) as an eluent instead of HF. We also aim to make the chromatography faster by shifting from a dual-column system to a single-column setting while still producing reproducible and reliable results. We aim to test the column for a different type of substrate, including freshwater, brine waters, and rock standards, to ensure it is transferable to different matrices.

5.2 Materials

We selected three standards to test and develop our new column chromatography procedure: an in-house synthetic fluid (Syn-1), a seawater standard (IAPSO), and a basalt standard (BHVO-2). These three standards were selected as they represent the most typical samples analyzed for δ^7Li, including river water matrix (Syn-1), brine (IAPSO) and silicate rock (BHVO-2). We prepared Syn-1 with average concentrations of major and trace elements and the highest Na/Li ratio of the river water samples used in this study. The cation concentrations of IAPSO, Syn-1 and BHVO-2 are shown in Table 3. IAPSO represents the brine waters endmember, whereas BHVO-2 represents the rock matrix endmembers.

Table 3: Cation concentrations of IAPSO (Summerhayes and Thorpe, 1998), Syn-1 and BHVO-2 standards (Wilson, 1997).

Sample Type	**Li (µg/kg)**	**Na (mg/kg)**	**Mg (mg/kg)**	**Al (µg/kg)**	**Ca (mg/kg)**	**Mn (µg/kg)**	**Cu (µg/kg)**	**Sr (µg/kg)**	**Ba (µg/kg)**
IAPSO	174	10770	1290	0.54	412	0.014	0.25	7900	14
Syn-1	11.04	10.51	10.49	42.64	28.43	3.28	1.20	5.64	2.66
BHVO-2	5 (mg/kg)	16400	43600	71600 (mg/kg)	81600	1290 (mg/kg)	127 (mg/kg)	389 (mg/kg)	130 (mg/kg)

TraceMetal™ Grade hydrochloric acid (HCl) and nitric acid (HNO_3) were purchased from Fisher and diluted to the required molarities with Milli-Q water purified to 18.2 MΩ acquired using a Milli-Q system. The molarities of HCl (6 N, 0.2 N and 0.18 N) and HNO_3 (6 N, 0.7 N) were used for column chromatography. The acid concentrations were accurately determined through the acid-base titration with NaOH and phenolphthalein as an indicator. Li carbonate isotopic reference material NIST RM 8545 (LSVEC; Flesch et al. (1973)) was used as the bracketing standard.

5.3 Column chromatography set-ups

We tested, improved and calibrated several protocols to purify Li using columns with different aspect ratios, testing different acids and incorporating a different amount of resin. The starting point from each tested protocol was obtained from the literature:

1) Protocol 1: The Bio-Rad Poly-Prep column chromatography was adapted from Li et al. (2019) and modified according to the following procedure. The Bio-Rad Poly-Prep columns (8mm ID x 4 cm Height) were loaded with 2 ml Dowex 50W-X8 200-400 mesh cation-exchange resin to separate Li from matrix elements, especially sodium. The columns were washed sequentially with 10 ml 6 N HCl, 10 ml Milli-Q water and then, conditioned with 10 ml 0.2 HCl. In order to evaluate the ability of the Bio-Rad Poly-Prep columns on separating Li from Na, synthetic samples with three different Na/Li ratios (1000, 10000, and 100000) were prepared using single-element standards, completely dried on a heating plate and re-dissolved in 1 ml 0.2 N HCl. The first matrix elements were eluted with 2 ml 0.2 N HCl, and then the second matrix elements were eluted with 3 ml of 0.5 N HCl. Using 0.2 N HCl effectively elutes most of the matrix cations, prevents possible early elution of Li, and switches to 0.5 N HCl, allowing a restricted elution range of Li with a stronger extraction ability (Li et al., 2019). The pre-cuts were collected by adding 1 ml 0.5 N HCl. The Li-bearing fractions were collected with 11 ml 0.5 HCl, and post-cuts were collected by adding 1 ml 0.2 N HCl. All matrix elution, pre-cuts, Li-bearing fractions and post-cuts were collected into acid-cleaned Teflon beakers. The collected samples from both columns were dried down and were prepared in 2% HNO_3 for ICP-MS analysis. The total procedure blank is <0.02 ng.

2) Protocol 2: The Bio-Rad Econo-Pac column chromatography was adapted from Liu & Li (2019) and modified according to the following procedure. The Bio-Rad Econo-Pac columns (15 mm ID x 12 cm Height) were loaded with 17 ml Dowex 50W-X8 200-400 mesh cation-exchange resin to purify Li from the majority of major and trace elements. The columns were washed sequentially with 100 ml 6 N HCl, 100 ml Milli-Q water and then conditioned with 50 ml 0.7 N HNO_3. Three IAPSO samples were prepared to test the first columns, they were completely dried on a heating plate and

re-dissolved in 2 ml 0.7 N HNO_3 and loaded onto the columns. Matrix elements were eluted with 25 ml 0.7 N HNO_3, pre-cuts were collected by adding 5 ml 0.7 N HNO_3. The Li-bearing fractions were collected with 50 ml 0.7 N HNO_3, and post-cuts were collected by adding 5 ml 0.7 N HNO_3. All matrix elution, pre-cuts, Li-bearing fractions and post-cuts were collected into acid-cleaned Teflon beakers. The collected samples from both columns were dried down and were prepared in 2% HNO_3 for ICP-MS analysis. The total procedure blank is <0.02 ng.

3) Protocol 3: The Savillex column chromatography was adapted from Li et al. (2019) and modified according to the following procedure. The capillary of each 30 ml long Savillex column (6.4 mm ID x 9.6 mm OD x 25 cm Capillary) was cut to 18 cm, then soaked in 6 N HCl for three days and in Milli-Q water for another three days. The columns were loaded with 2.9 ml of the Dowex 50W-X8 200-400 mesh cation-exchange resin (~ 9.1 cm height), washed sequentially with 15 ml 6 N HCl and 15 ml Milli-Q water. Columns were conditioned using 10 ml 0.18 N HCl. The re-dissolved samples in 2 ml 0.18 N HCl were loaded onto the columns. After passing through 14 ml 0.18 N HCl, the Li-elution was collected with 18.5 ml 0.18 N HCl. 1 ml of the pre-cut and post-cut were collected before and after Li-elution. All pre-cuts, Li-bearing fractions and post-cuts were collected into acid-cleaned Teflon beakers. The collected samples were dried down and were prepared in 2% HNO_3 for ICP-MS analysis. The total procedure blank is <0.02 ng.

5.4 Results and discussions on column chromatography development

As an initial step, the first column chromatography protocol, the Bio-Rad Poly-Prep column chromatography, was tested to separate Li from Na. Efficient Li and Na separation are essential to obtain accurate and precise δ^7Li analysis. We tested three synthetic solutions with different Na/Li ratios (1000, 10000 and 100000). Three different ratios of synthetic solutions were tested because the river water samples used in this study have a broad range of Ni/La ratios. The range of Na/Li ratios was selected to cover the Na/Li of IAPSO, which was used as one of the standards throughout the Li purification of river water samples for this study (Na/Li ratio =61,897). Syn-1 has a Na/Li ratio of 952. Consequently, we selected a range of Na/Li that covers

our samples and standards. The results of Li, Na concentrations and Na/Li mass ratios are shown in Table 4. The Bio-Rad Poly-Prep column chromatography did not allow good separation of Li from Na. When the initial Na/Li mass ratios are compared to the collected Na/Li mass ratios, these ratios are decreased by about half. However, the collected Na/Li mass ratio remains well above 3, the maximum limit to avoid interferences and matrix effect during MC-ICP-MS analysis of Li isotope measurements (Liu & Li, 2019). This step demonstrated that the Bio-Rad Poly-Prep column chromatography did not provide an efficient protocol to purify Li from Na. Rather than modifying the protocol and considering how poorly this set-up separated Na and Li, we decided to pursue a different column chromatography set-up.

Table 4: The results of ICP-MS for the Bio-Rad Poly-Prep column. The sample number (1000, 10000, and 100000) indicates the Na/Li ratio before chromatography, and ME represents matrix elution. The elution of ME1 is collected in the first 2 ml 0.2 N HCl. The ME2 elution is collected between 3-5 ml 0.5 N HCl, and then 1 ml 0.5 N HCl of the Pre elution is collected. The Li elution is collected between 7-18 ml 0.5 N HCl, and 1 ml 0.5 HCl of the Post elution is collected.

Sample	**Initial Na/Li mass ratio**	**Collected Li (ppb)**	**Collected Na (ppb)**	**Collected Na/Li mass ratio**
1000-ME1		0	0	0
1000-ME2		0	0	0
1000-Pre		0.3	0	0
1000-Li	1018	50.1	26047	520
1000-Post		0	13	0
10000-ME1		0	0	0
10000-ME2		0	0	0
10000-Pre		0.3	0	0
10000-Li	10456	53.1	258835	4877
10000-Post		0	6	0
100000-ME1		0	0	0
100000-ME2		0.1	0	0
100000-Pre		3	0	0
100000-Li	102116	23.6	570276	24144
100000-Post		0	8	0

The Bio-Rad Econo-Pac column chromatography has already been used to separate Li from Na (Liu & Li, 2019). However, this set-up usually requires multiple paths to separate Li from Na efficiently. As an initial step to assess the ability of this system to separate Na from Li, three IAPSO standards were eluted through the columns (Fig.16). The eluents were collected every 5 ml during the chromatography, and the Li recovery of the samples was 99.4%, 99.6%

and 100.7%, respectively. It is clear from the obtained elution profiles that this column chromatography set-up was not efficient in separating Na from Li from IAPSO standards. In particular, the separation between the Li elution curve and the Na elution curve was not sufficient and overlapped (Fig.16). We also observed that the elution curve of IP1 was delayed compared to the other elution curves. This problem arose from an issue with the column packing and was corrected in further experiments. The elution profiles of Li and Na overlapped, and the Na/Li mass ratio of the Li elution was still higher than 3,000. The collected Na/Li mass ratios are still 3 orders of magnitude too high for Li isotope analysis. This indicates that the Bio-Rad Econo-Pac column chromatography either requires an additional column path to purify Li from Na further, that more resin needs to be added to the column or that a longer column needs to be used. As this column chromatography set-up already took more than 6 hours to elute Li, we decided that this set-up was not appropriate to develop an efficient single column Li chromatography protocol.

We then decided to test the Savillex column instead of the previous test, the Bio-Rad Econo-Pac column. The Savillex column has a narrow inner diameter of 6.4 mm and a long capillary of 18 cm. Increasing the aspect ratio of the column makes elution curves narrower and provides better separation between Li and Na. However, this column packed with resin also leads to a very slow flow rate and long elution time. To develop the most efficient protocol, we changed the type and molarity of acid from 0.7 N HNO_3 to 0.2 N HCl for the Savillex column chromatography. We changed the acid type and molarity based on the previous set-up described in the literature (Li et al., 2019). HCl has a better separation factor for Li/Na than HNO_3, and low molarity HCl facilitates a more rapid elution of Li and Na, which is also important when using high aspect ratio columns. Li et al. (2019) conducted Li purification from Na for various geological samples using the mixed eluent (1.5 mol/L HNO_3 + 70% methanol) and observed an early breakthrough of Na during Li fractions resulting in unsatisfactory purification. They also performed the Li purification with 0.2 N HCl, which still shows an incomplete Li separation from Na, but Na only started eluting out at the final stage of Li elution. Therefore, the Savillex

column chromatography was adapted from Li et al. (2019) but needed to be calibrated for water standards before the sample purification.

The Savillex column chromatography has two advantages compared to the Bio-Rad Econo-Pac column chromatography; (1) it requires less amount of resin (2.9 ml of resin is loaded onto the Savillex column, while 17 ml of resin was loaded onto the Bio-Rad Econo-Pac column) and (2) it reduces the retention time by an hour or two.

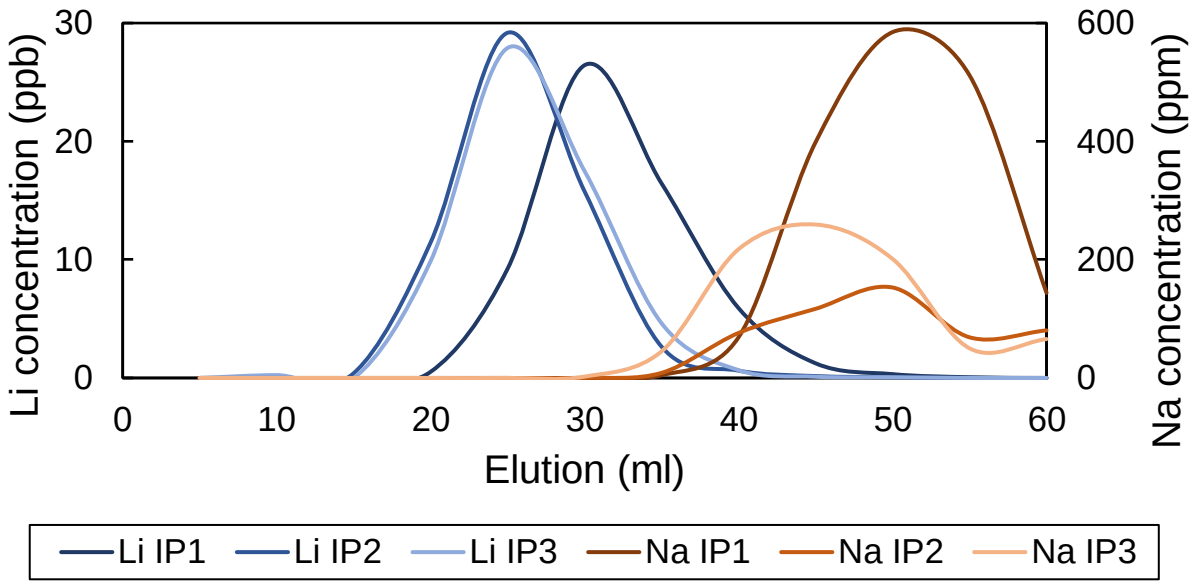

Figure 16: The elution curves of Li and Na on the Bio-Rad Econo-Pac column.

As for the previous chromatography experiment, several IAPSO samples were eluted through the Savillex column chromatography. After a single path in this column set-up, Li and Na were completely separated and did not overlap, providing a complete recovery (~100 %) and a satisfactory Na/Li ratio (close to 0), as seen in Table 5. The column used for IP3 was re-calibrated afterwards. The Savillex column chromatography results indicate that any water samples with an initial Na/Li ratio of less than 61,897 and a sample volume used to retain 60 ng Li can be properly purified for Li.

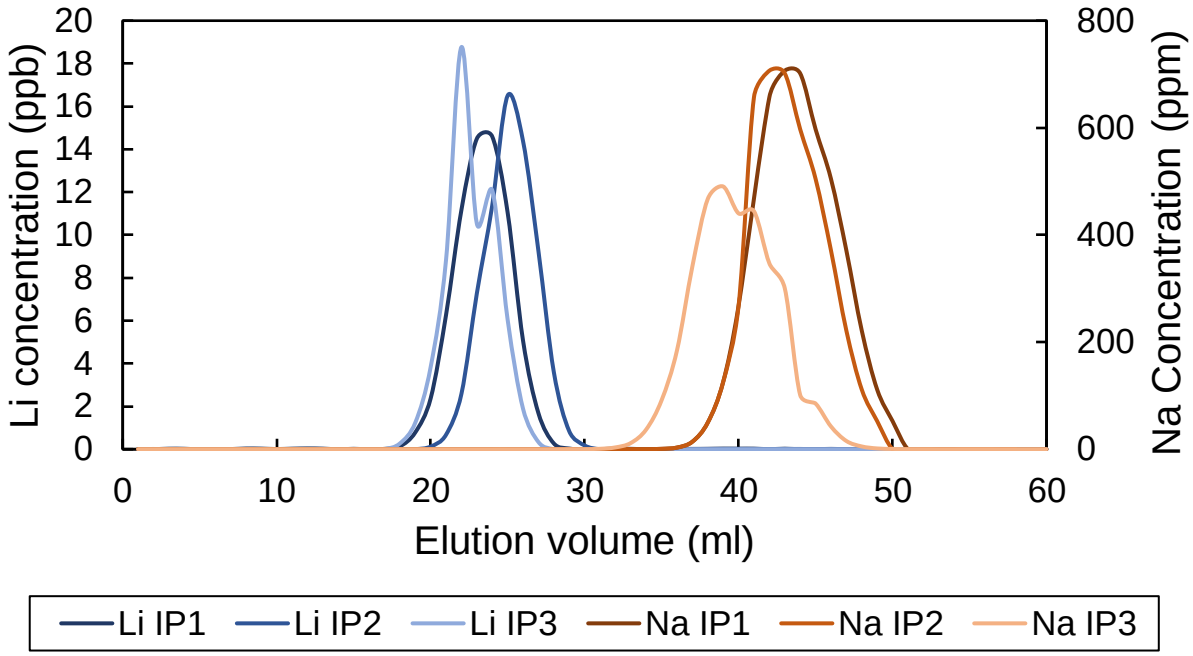

Figure 17: The elution curves of Li and Na on the Savillex column.

Table 5: Li recovery and Na/Li ratios before and after the Savillex column chromatography with 60 ng Li of IAPSO standards.

Sample type	Initial Na/Li ratio	Li mass added (ng)	Li mass collected (ng)	Na mass collected (ng)	Collected Na/Li ratio	Li Recovery (%)
IAPSO (IP1)	61,897	66.4	67.9	0.2	0	102.3
IAPSO (IP2)	61,897	66.4	66.8	0.1	0	100.5
IAPSO (IP3)	61,897	66.8	63.8	0.1	0	95.6

In order to test the sensitivity of the single column to concentrations and the possibility of elution shift, we eluted a series of IAPSO samples with double the mass tested initially (120 ng Li). Table 6 shows the results of sensitivity testing. In this case, the single-column Savillex column chromatography set-up did not provide satisfactory Li purification as the Na/Li mass

ratio of the eluted sample was higher than 50. We then re-eluted the samples through a second column path. With two paths, the Li was completely purified from Na with a complete recovery.

Table 6: Li recovery and Na/Li ratios before and after single-column chromatography with doubled-mass (120 ng Li) of IAPSO standards.

Sample type	Li mass added (ng)	Li mass collected (ng)	Na mass collected (ng)	Collected Na/Li ratio	Li Recovery (%)	δ^7Li	2SD
1st column elution							
IAPSO (IP1)	123.8	141.6	17044.3	120.4	114.4		
IAPSO (IP2)	123.1	137.8	5738.3	41.6	111.9		
IAPSO (IP3)	123.7	129	44929.4	348.2	104.3		
IAPSO (IP4)	123.1	140.8	6263.7	44.5	114.3		
2nd column elution							
IAPSO (IP1)	123.8	122.5	0	0	99		
IAPSO (IP2)	123.1	131.8	0	0	107.1	29.2	1.09
IAPSO (IP3)	123.7	126.7	0	0	102.4	32.4	0.61
IAPSO (IP4)	123.1	131.2	0	0	106.6	32.5	0.07

To further refine the mass of Li purifiable and improve the Li and Na separation, we attempted to purify 80 ng Li from IAPSO samples. Additionally, the concentration of HCl was changed from 0.20 N to 0.18 N to widen the gap between Li and Na elution curves due to the weaker extraction ability of a lower concentration of HCl. The single-column system testing with 80 ng Li shows a complete Li recovery and a satisfactory Na/Li mass ratio (Table 7).

In the next step, we verified the ability of this column chromatography set-up to provide accurate and precise δ^7Li values for a range of standards, including IAPSO, Syn-1 and BHVO-2. The measured δ^7Li of Syn-1 is 55.9 ± 1.32 ‰ (n=6) and IAPSO is 30.89 ± 2.62 ‰ (n=6). Both standards provide reproducible results and fall on the value provided by the literature within uncertainty. However, the measured δ^7Li values from BHVO-2 fall slightly outside the range suggested in the literature 4.7 ± 0.20 ‰ (Brand et al., 2014), and both BHVO-2 standards tested on the Savillex column chromatography do not agree with the published data within the analytical error. BHVO-2 has a much higher Na/Li ratio than either IAPSO or Syn-1. The eluted sample after one column pass shows Na/Li>3 (Table 7). This suggests that proper purification of Li for silicate samples require a second column pass of the eluted fraction or the development of a silicate specific column with more resin. As the focus of this thesis is not on silicate rocks, we decided not to inquire further about the development of a single column procedure for this substrate.

The standard deviation of the measured δ^7Li of IAPSO is high (30.89 ± 2.62 ‰) compared to the published data. The accuracy and external reproducibility were determined from repeat measurements (n=33) of IAPSO, which yielded δ^7Li = 31.10 ± 0.68 ‰, over a period of 8 months.

We developed a new single Savillex column chromatography column able to separate Li from Na for water samples. We recommend this methodology when studying δ^7Li values in freshwater and brine samples. For any samples with an initial Na/Li mass ratio lower than 61,897, the Savillex column chromatography can extract 80 ng Li with satisfactory separation of matrix and Na. Other types of samples with higher Na/Li, such as some silicates, would require a two-column pass or a lower amount of Li extracted.

Table 7: Li recovery and Na/Li ratios before and after single-column chromatography with 80 ng Li of IAPSO, Syn-1 and BHVO-2 standards. Standards start with 2- and 3- were run along with the river water samples.

Sample type	Li mass added (ng)	Li mass collected (ng)	Na mass collected (ng)	Collected Na/Li ratio	Li recovery (%)	δ^7Li	2SD
IAPSO (IP1)	80.9	89.7	831.8	9.3	110.8	32.0	1.16
IAPSO (IP2)	81.0	86.5	0	0	106.8	30.1	0.46
IAPSO (IP3)	81.0	87.9	0	0	108.5		
IAPSO (IP4)	81.2	83.8	0	0	103.3	29.2	1.07
Syn-1 (HW1)	80.2	82.7	0	0	103.0	56.6	0.47
Syn-1 (HW2)	80.2	84.3	0	0	105.1	56.3	0.15
Syn-1 (HW3)	80.3	81.2	58.8	0.7	101.2	56.0	0.06
BHVO-2 (BH1)	83.8	83.5	1171	14.0	99.6	5.6	0.22
BHVO-2 (BH2)	83.6	83.0	1077	13.0	99.3	6.5	0.61
IAPSO (2-IP1)	80.1	81.8	0	0	102.1	30.3	0.73
IAPSO (2-IP2)	80.6	82.4	0	0	102.2	30.5	0.77
Syn-1 (2-HW1)	81.0	83.4	0	0	103.0	54.9	0.81
Syn-1 (2-HW2)	81.1	84.2	0	0	103.8	55.3	0.60
IAPSO (3-IP1)	81.3	84.0	0	0	103.4	31.8	0.37
Syn-1 (3-HW1)	81.2	81.3	0	0	100.2	56.3	0.41

6. Results

The information on sample location, main cation concentrations, Li and Sr isotope data, and environmental, geological and climatological results are attached in the Appendix.

6.1 Geochemical Data and PCA

We started our data analysis by applying Principal Component Analysis (PCA) on a subset of geochemical variables of interest (Fig.18). We used the $^{87}Sr/^{86}Sr$, δ^7Li, Li, Sr, Ca, Mg, Ca and Na concentrations and calculated X/Na molar ratio. The Sr, Ca, Mg, Ca, and Na concentrations are given in Table 8, and the X/Na molar ratios of 102 rivers are plotted in Fig.19. We focused on these variables because they inform about carbonate and silicate weathering and weathering intensity, two major variables to understand weathering processes on the Yukon River Basin (Brennan et al., 2014).

The PCA axes explain close to 70% of the variation observed in the geochemical data. We observe two distinct groups of variables: X/Na ratios, except for Li/Na, predominantly drive variations along the x-axis, whereas δ^7Li, 1/Li and Li/Na vary along the y-axis. While the PCA does not incorporate all the geochemical variance, these variables likely reflect similar processes. In addition, when looking at individual tributaries, some plot on positive values on the x-axis (e.g., Koyukuk), whereas others have negative values (e.g., White, Upper Yukon). Some basins also plot with positive y-axis values (e.g., Koyukuk), whereas other plots on negative y-axis values (e.g., Porcupine and Kantishna). This observation suggests that weathering processes differ between tributaries, which would be expected for such a large watershed with different geoenvironmental conditions.

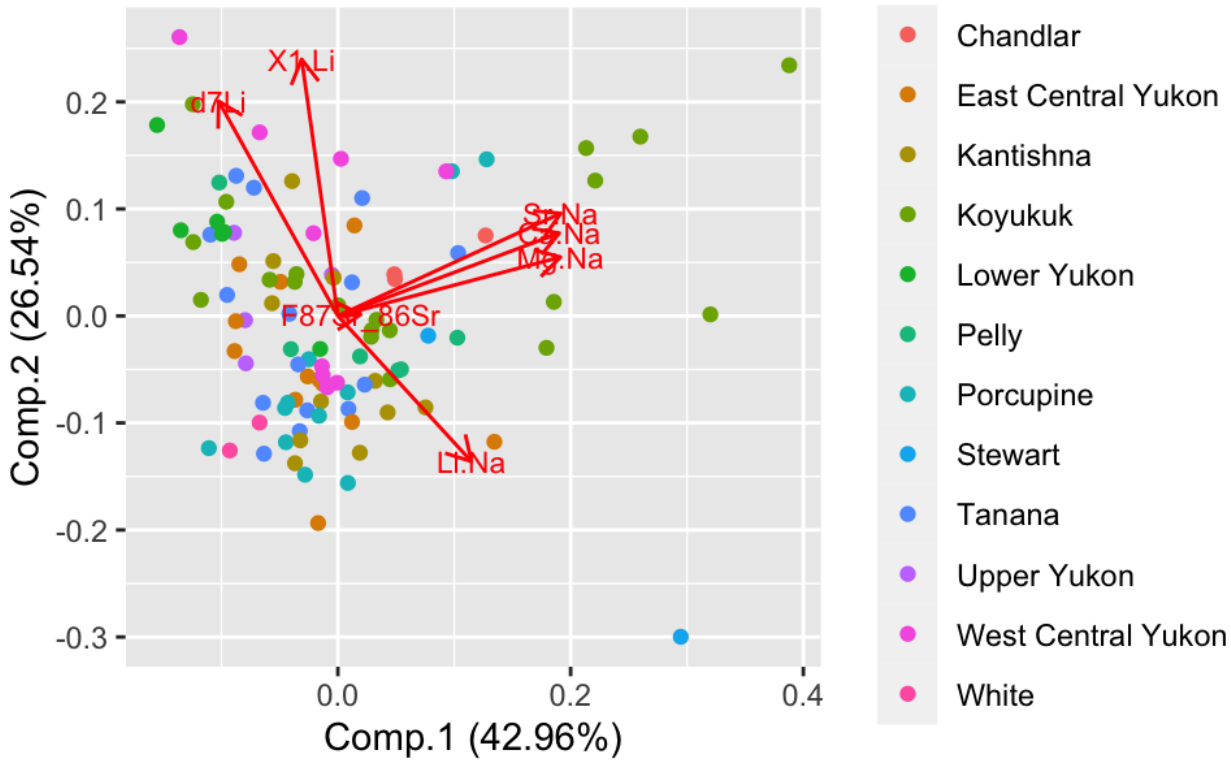

Figure 18: PCA of isotope measurements and molar ratios of Yukon River samples.

6.2 Mixing between carbonate and silicate weathering sources

Based on this PCA analysis, we first focused our result description on the variable dominating the x-axis variance, including X/Na and $^{87}Sr/^{86}Sr$. These variables are commonly used in the literature to assess the contribution of silicate and carbonate weathering on geochemical variations of the dissolved load.

Ca and Sr concentrations in the Yukon River Basin show a typical positive correlation (r = 0.82) (Fig.19A). The Ca/Sr ratios of the river samples varied from 197 to 1130 and were plotted between endmembers ratios representing mono-lithological catchments draining carbonates, mafic silicates and felsic silicates (Meybeck, 1986; Brennan et al., 2014). The goal of this plot is to help quantify the contribution of these different endmembers to the sampled catchments. Most of the sampled rivers plot between the carbonate and silicate endmembers, with some catchments forming distinct groups. Most of the Koyukuk catchment samples are closer to the silicate endmember, whereas Porcupine samples are closer to carbonates.

Catchments such as the Lower Yukon, Koyukuk, and Tanana display large variations between these endmembers, likely indicating intra-catchment changes of dominant weathering sources.

We used a ternary diagram to assess further carbonate contribution vs. silicate contribution in the collected rivers (Fig.19B). Rivers plotting closer to the Na+K apex indicates increased contribution of silicate weathering, and samples plotting closer to the Ca-Mg line indicates a stronger contribution from carbonate weathering. A few rivers show a strong contribution of silicate weathering, but overall, the ternary diagram does not help distinguish between tributaries. Most tributaries are dominated by a mixing of silicates and carbonates weathering.

We then used log-log plots of Sr/Na and Mg/Na ratios versus Ca/Na ratios to further identify mixing between silicate and carbonate in a different river. We found strong relationships between Sr/Na and Mg/Na ratios versus Ca/Na ratios ($r = 0.89$ and $r = 0.84$, respectively) with the data plotting between the published silicate and carbonate endmember values (Fig.19C-D) (Gaillardet et al., 1999; Brennan et al., 2014). Both plots indicate a mixed contribution of carbonate (high X/Na ratios) and silicate (low X/Na ratios) weathering sources across the entire basin.

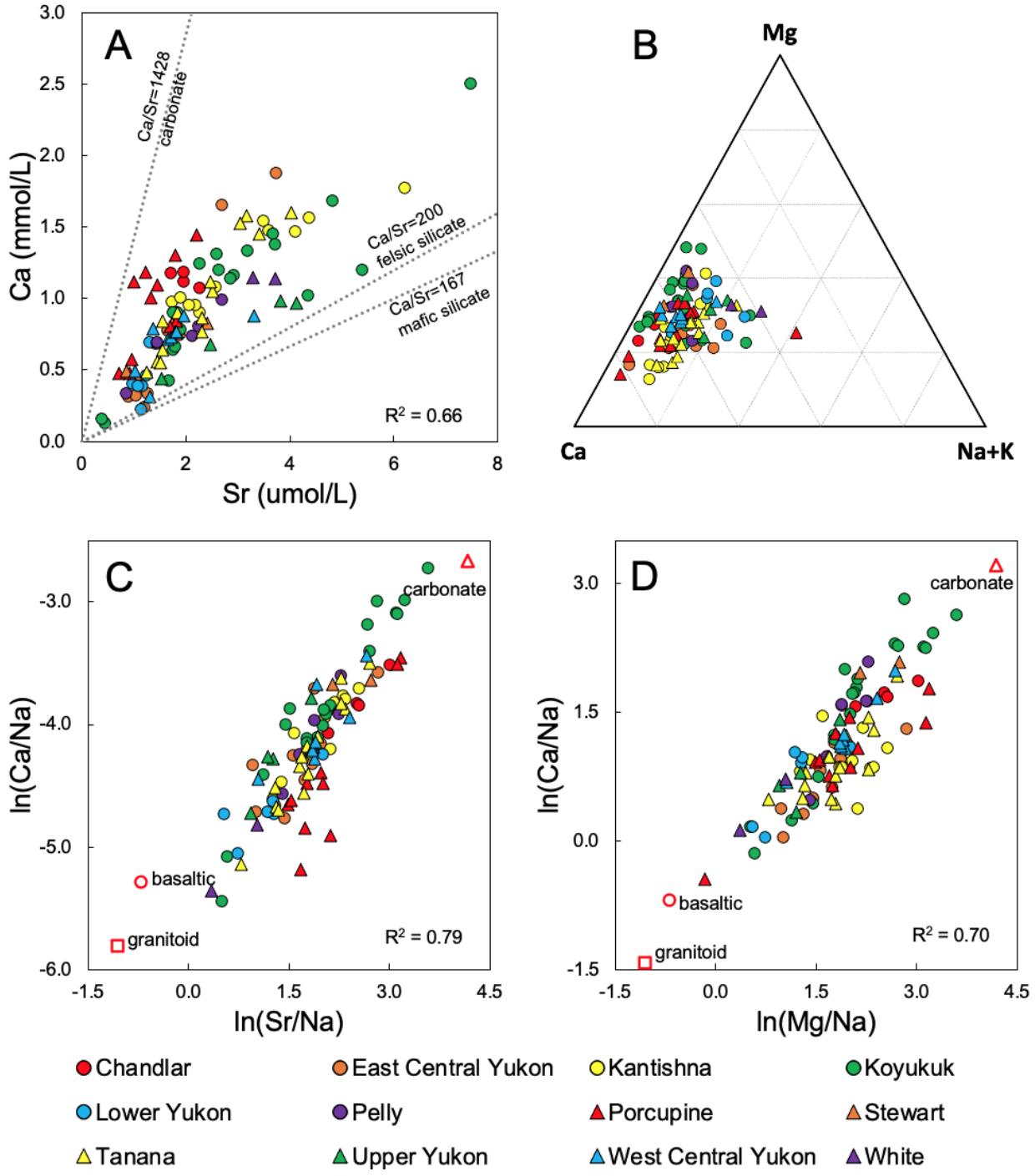

Figure 19: A) Ca versus Sr concentrations for rivers draining the Yukon River Basin classified into the major drainage basins. Dotted lines indicate monolithic catchments of pure carbonates (Ca/Sr = 1428), felsic silicates (Ca/Sr = 200) and mafic silicates (Ca/Sr = 167) (Meybeck, 1986; Brennan et al., 2014). B) Mg-Ca-Na+K ternary diagram for rivers draining the Yukon River Basin. C & D) Log-log plots of X/Na ratios. Published endmembers are (J. Gaillardet et al.,

1999; Brennan et al., 2014): felsic silicate (open red square), mafic silicate (open red circle) and carbonate (open red triangle).

Elemental data plots did not appear sufficient to quantify the contribution of different lithologies in controlling river hydrochemistry. We used elemental data combined with the $^{87}Sr/^{86}Sr$ ratio to assess carbonate vs. silicate contribution further. We constructed hyperbolic mixing models of rivers draining a mixture of carbonates vs. silicates to illustrate the change in bedrock sources of rivers. We compared the mixing values found in the Yukon River with theoretical mixing lines of pure carbonates with an increasingly $^{87}Sr/^{86}Sr$ ratio in silicates (EM1 to EM5) (Fig.20A). Increasing $^{87}Sr/^{86}Sr$ ratios in silicates usually correspond to rock units that are increasingly felsic (e.g., granites) and increasingly old (e.g., cratonic). As the Yukon River Basin displays silicate lithology with a whole range of age and type, using the $^{87}Sr/^{86}Sr$ ratio is probably a more effective technique than molar ratios to assess the influence of lithology on geochemical data.

We find that the White, Upper Yukon, Koyukuk and the majority of West Central Yukon and Lower Yukon samples are scattered along or between the mixing lines of less radiogenic Silicate EM1 and EM2. The other drainage basins are scattered along the mixing lines of more radiogenic Sil EM3-5. Most of the other drainage basins are scattered along or between mixing lines of Sil EM3 ($^{87}Sr/^{86}Sr = 0.719$) and EM4 ($^{87}Sr/^{86}Sr = 0.732$), but the East Central Yukon and Tanana are scattered along with the Sil EM5 ($^{87}Sr/^{86}Sr = 0.78$) mixing line, indicating more radiogenic Sr source than other drainage basins (Fig.20A). A plot of $^{87}Sr/^{86}Sr$ against Ca/Sr ratios show a similar mixing between silicate and carbonate endmembers (Fig.20B). The Porcupine drainage basin plots close to carbonate endmember, as seen in Fig.19.

Table 8: Silicate and carbonate endmembers used to plot hyperbolic mixing lines in Figure 20A.

End Member	**Ca/Na**	**Sr/Na**	**Mg/Na**	**$^{87}Sr/^{86}Sr$**	**Reference**
Silicate EM1	0.5	0.005	0.5	0.703	(Gaillardet et al., 1999; Ingram & Weber, 1999; Brennan et al., 2014)
Silicate EM2	0.35	0.003	0.24	0.707	(Gaillardet et al., 1999; Ingram & Weber, 1999; Brennan et al., 2014)
Silicate EM3	0.35	0.003	0.24	0.719	(Gaillardet et al., 1999; Brennan et al., 2014; Keller et al., 2007)
Silicate EM4	0.35	0.003	0.24	0.732	(Goldfarb et al., 1997; Gaillardet et al., 1999; Douglas et al., 2013; Brennan et al., 2014)
Silicate EM5	0.35	0.003	0.24	0.78	(Gaillardet et al., 1999; Millot et al., 2003; Brennan et al., 2014)
Carbonate EM	65	0.07	25	0.708	(Gaillardet et al., 1999; Brennan et al., 2014)

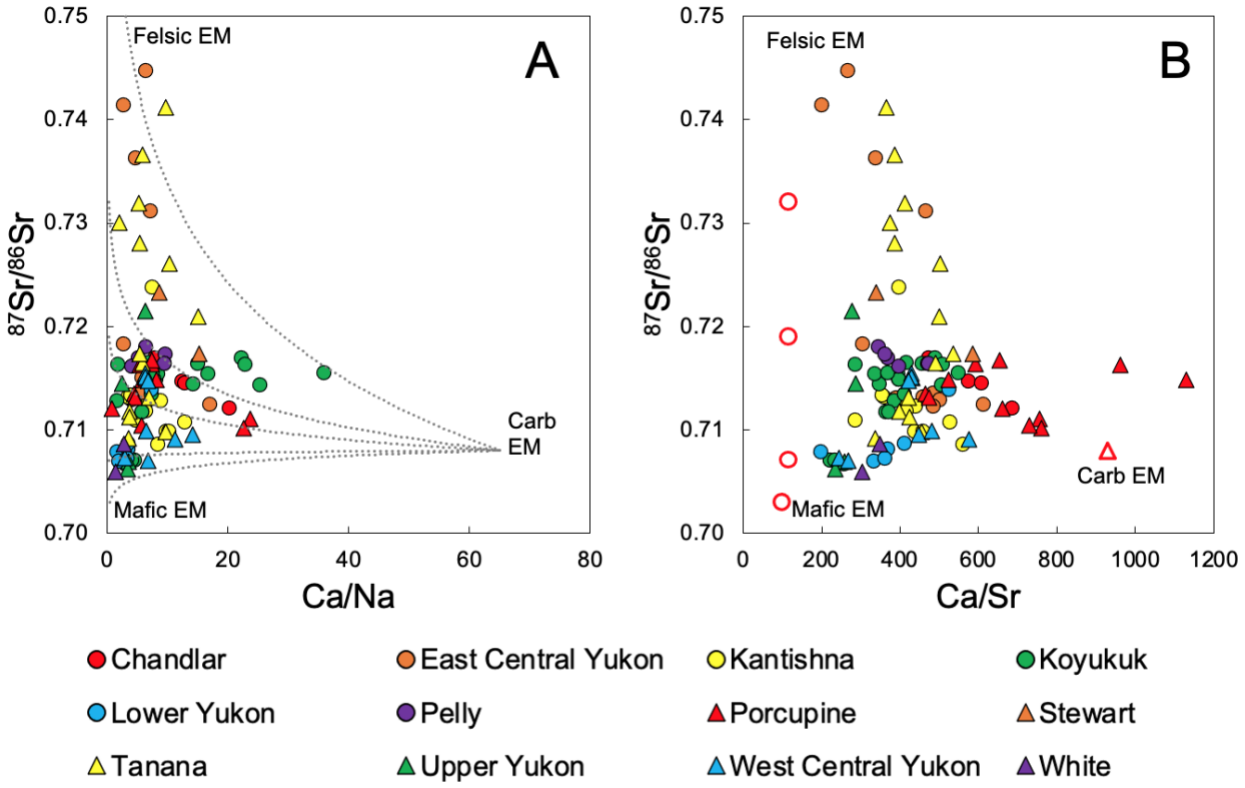

Figure 20: (A) Hyperbolic mixing plots of $^{87}Sr/^{86}Sr$ versus Ca/Na ratios of the Yukon River. Dotted lines are hyperbolic mixing lines between five silicate endmembers and a carbonate endmember. B) Ca/Sr versus $^{87}Sr/^{86}Sr$ ratios with silicate endmembers (open red circle) and a carbonate endmember (open red triangle).

6.3 Spatial patterns of Li and Sr isotope variations and the influence of geological variables

In this section, we describe the spatial patterns of $^{87}Sr/^{86}Sr$ and $\delta^{7}Li$ values as well as the lithological, geological and environmental characteristics of the catchments. A great variation of riverine $^{87}Sr/^{86}Sr$ ratios (0.707 to 0.745) and $\delta^{7}Li$ values (8 to 33‰) is observed across the Yukon River Basin (Fig.21A and B).

The headwater and its surrounding regions are a mountainous area (Fig.6) underlain by sporadic permafrost (Fig.12), where the mean annual ground temperature is the highest within the Yukon River Basin (Fig.9). While crysols, a thick soil layer, dominantly cover the Yukon River Basin, the headwater and its surrounding regions are covered with a weakly developed soil layer, brunisols (Fig.8). The headwater region is extensively covered with younger siliciclastic

rock units and volcanic rocks of the Stikine terrane (Gaillardet et al., 2003). Most of the tributaries in the headwater display low riverine $^{87}Sr/^{86}Sr$ (<0.710) and intermediate riverine δ^7Li values (16 to 24‰). The Stewart and Pelly rivers have a higher proportion of carbonate units that the rest of the headwater region. These rivers and their tributaries display intermediate riverine $^{87}Sr/^{86}Sr$ (0.710-0.720) and low riverine δ^7Li values (<16‰).

As the Yukon River flows westward to the Canada/Alaska boundary, it drains order metamorphic rock units of the Yukon-Tanana terrane. The Yukon-Tanana terrane is mountainous regions (Fig.6) underlain by discontinuous permafrost and locally continuous permafrost (Fig.12). The mean annual ground temperature is higher than the headwater regions (Fig.9). The Tintina Fault dissects the Yukon-Tanana terrane from the north (Dusel-Bacon et al., 2013), displaying completely different lithologies. The north region of the Yukon-Tanana terrane is primarily composed of carbonate and siliciclastic rock units, displaying lower riverine $^{87}Sr/^{86}Sr$ than the Yukon-Tanana terrane. The south of the Yukon-Tanana terrane, which is dissected by the Denali Fault, show low riverine $^{87}Sr/^{86}Sr$ derived from siliciclastic and carbonate rock units. Within the Yukon Tanana area, tributaries haves higher riverine $^{87}Sr/^{86}Sr$ (>0.720) from these radiogenic rock units. The upper part of the Tintina Fault within the Yukon-Tanana terrane displays low riverine δ^7Li values, whereas the rivers draining the metamorphic rock units of the Yukon-Tanana terrane show slightly higher riverine δ^7Li values. These regions are underlain by discontinuous to continuous permafrost (Fig.12). The western part of the Yukon-Tanana terrane displays very high riverine δ^7Li values (>28‰), where it is underlain by sporadic to isolated patches of permafrost (Fig.12). The lower part of the Denali Fault shows low riverine δ^7Li values primarily derived from the siliciclastic and carbonate rock units.

The northern part of the basin, which comprises the Porcupine, Chandalar and mountainous regions of Koyukuk drainage basins (Fig.5B), is predominantly underlain by continuous permafrost (Fig.12) and is mostly covered with carbonate and siliciclastic rock units. These rivers show intermediate riverine $^{87}Sr/^{86}Sr$ and low riverine δ^7Li values. Locally, when some volcanic rock units are present within the Chalandar drainage basin (Fig.21A), rivers display low riverine $^{87}Sr/^{86}Sr$ and higher riverine δ^7Li values.

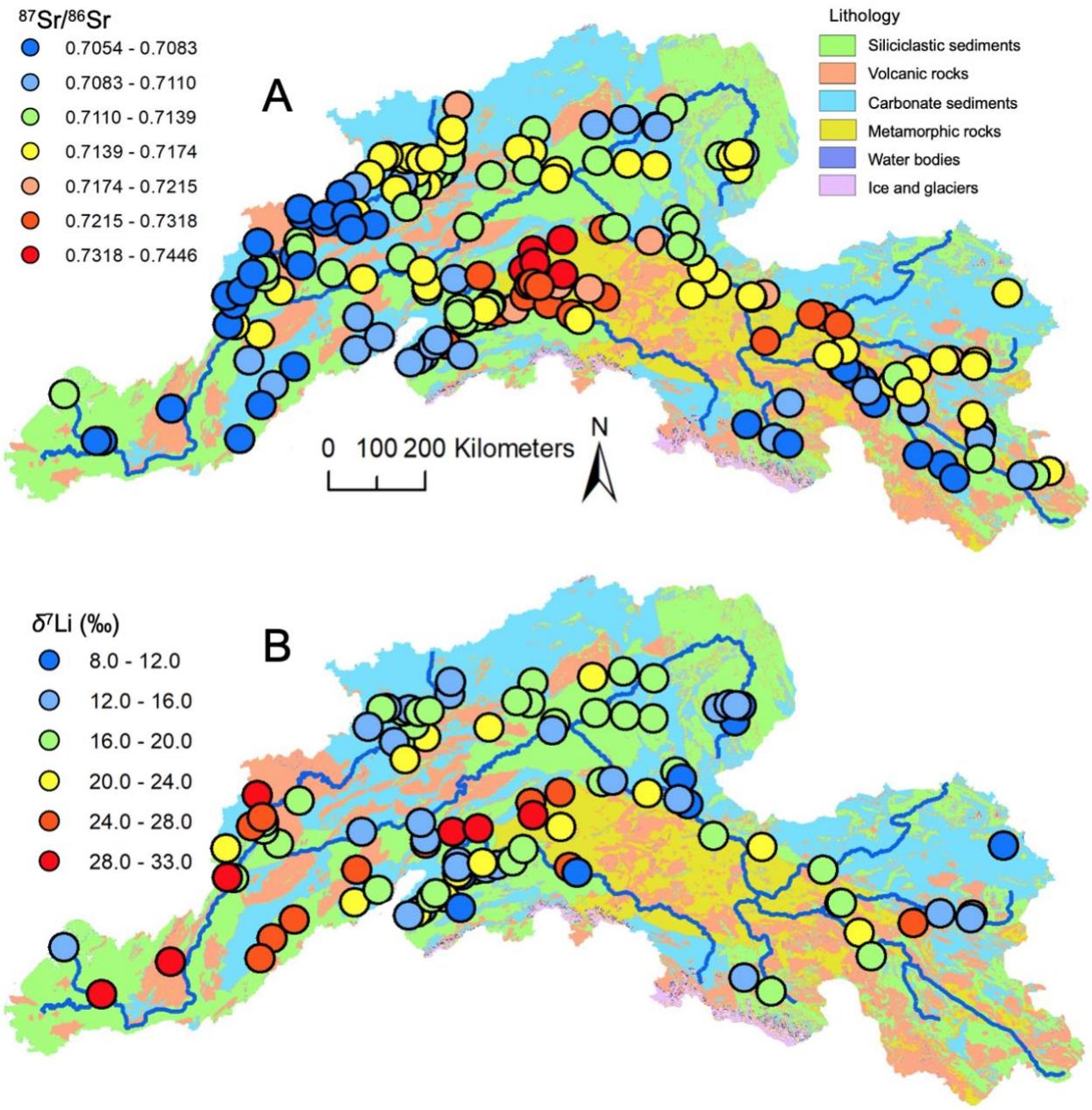

Figure 21: The variation of (A) riverine $^{87}Sr/^{86}Sr$ and (B) riverine δ^7Li plotted on lithology map.

In addition to the spatial trend in δ^7Li and $^{87}Sr/^{86}Sr$ variations, we observe some covariations between δ^7Li and $^{87}Sr/^{86}Sr$ (Fig.22). We grouped rivers into three main categories of $^{87}Sr/^{86}Sr$ ratios (Fig.21A); rivers draining young volcanic rocks and terranes (e.g., headwaters, lower Yukon, lower Koyukuk) display low riverine $^{87}Sr/^{86}Sr$ (<0.710) and high δ^7Li (blue shaded area on Fig.22). Rivers predominately covered with marine silicates and carbonates (e.g., Pelly,

Kantishna, Porcupine, Koyukuk, Chandalar) display intermediate riverine $^{87}Sr/^{86}Sr$ (0.710-0.720) and low δ^7Li (green shaded area on Fig.22). Rivers draining old metamorphic rocks (e.g., Tanana, East Central Yukon, Dawson Range tributaries) display the highest riverine $^{87}Sr/^{86}Sr$ (>0.720) and high δ^7Li (orange area on Fig.22).

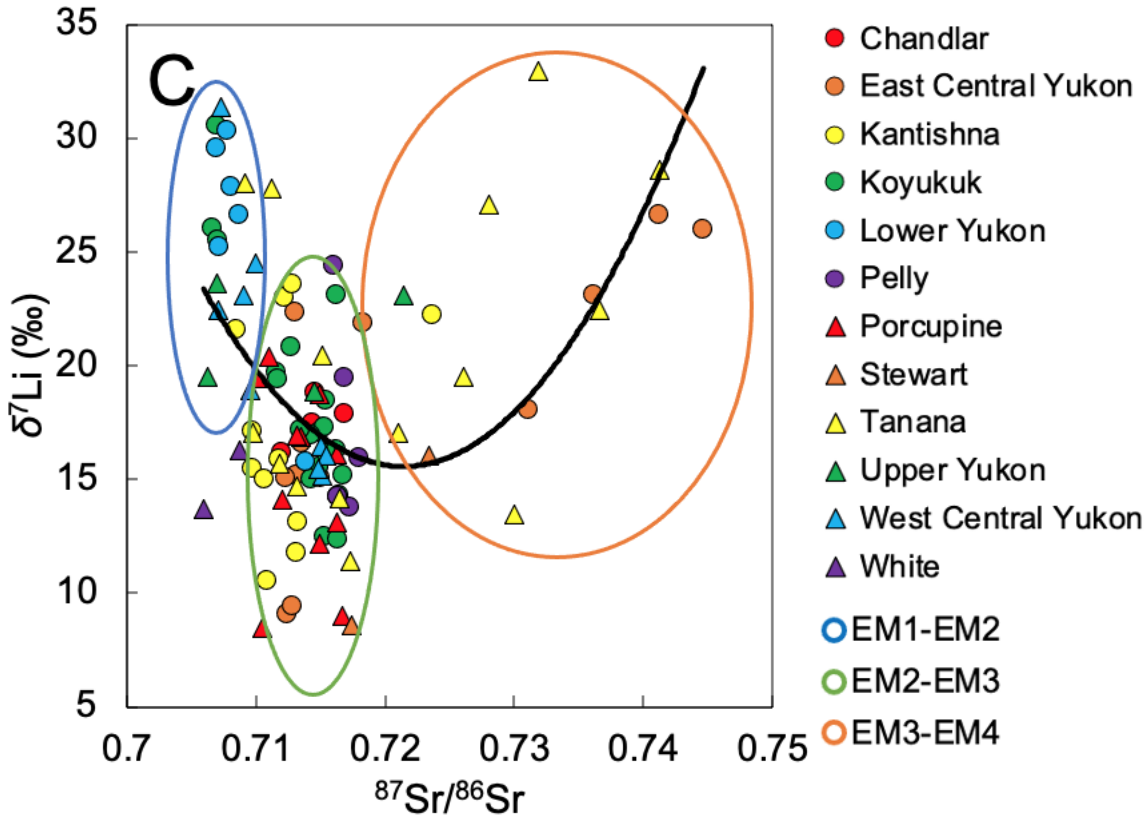

Figure 22: δ^7Li versus $^{87}Sr/^{86}Sr$ for rivers draining the Yukon River Basin. The Yukon River Basin can be classified into three silicate endmembers (Table 8): Lower Yukon and lowlands of Koyukuk in EM1-EM2 (blue region), uplands of Tanana and East Central Yukon in EM3-EM4 (orange region) and other drainage basins in EM2-EM3 (green region).

6.4 PCA of environmental, climatic and geological predictors to Li and Sr isotopes

This section now incorporates the environmental, geological, and climatic conditions on each sampled catchment to show how the hydrochemistry relates to these variables. We first perform a PCA between isotopic data and various environmental, climatic and geological

variables calculated using GIS methods (see Methods 4.4). We find that the two main axes of the PCA explain ~40% of the variance. While this is not the totality of the variance, the visualization on the PCA plots helps understand how different variables covary. δ^7Li values vary dominantly along the x-axis with the percentage of carbonates on the sampled watershed, average permafrost probability, the average mean air temperature, the average mean ground temperature, the slope of the channel. Conversely, $^{87}Sr/^{86}Sr$ ratios of sampled rivers vary dominantly along the y-axis with metamorphic and silicate percentages on the sampled watershed, the average aerosol deposition, and the average soil pH. Other variables, including average soil cation exchange capacity and soil clay content, vary along both axes equally.

As observed with the PCA on geochemistry data, rivers do not vary along the same axis relative to these variables. The Porcupine, Koyukuk and West Central Yukon drainage basins display large variations along the x-axis. Other rivers, such as the Tanana and East Central Yukon, display greater variations along the y-axis.

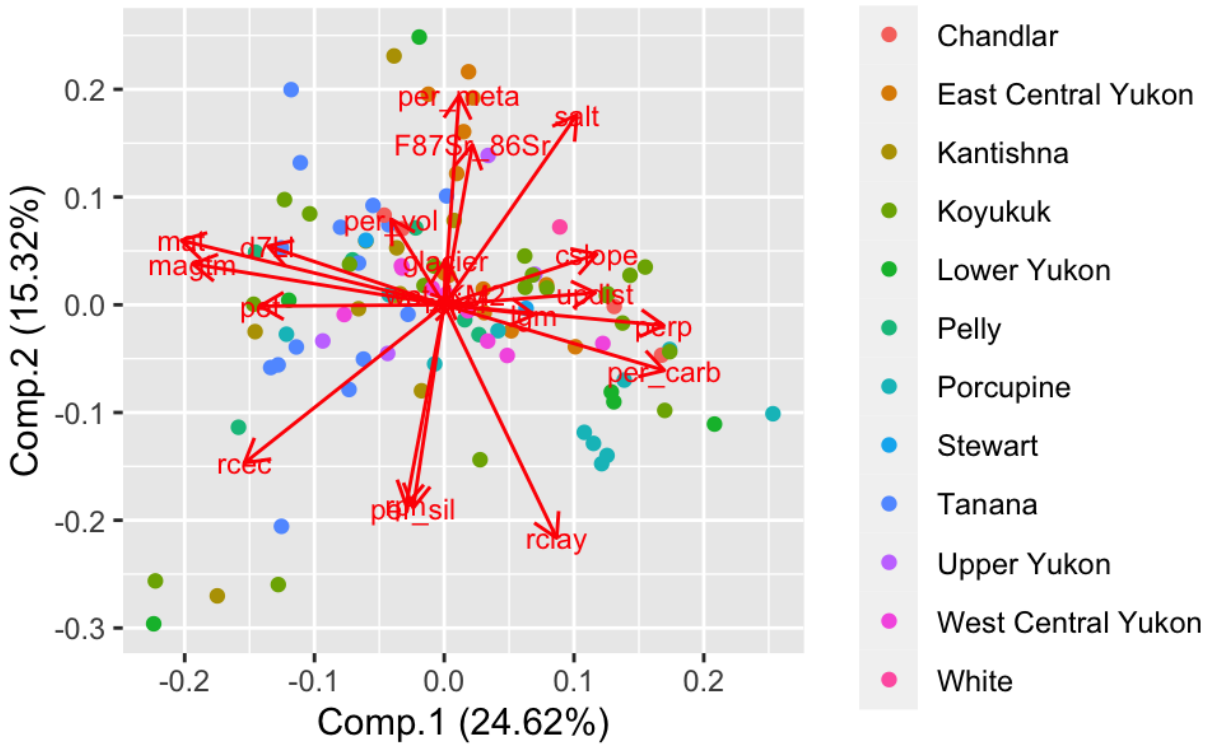

Figure 23: PCA of isotope measurements, environmental, climatic and geological predictors.

6.5 General trends in each sub-basin of the Yukon River Basin and the overall trend

The following section focuses on describing the δ^7Li variations across the Yukon River Basin, as this is a strong proxy for weathering processes (see section 2). We compare the Li and δ^7Li geochemistry of the Yukon River to other north latitude basins, including the Lena River (Murphy et al., 2019), Mackenzie River (Millot et al., 2010) and Lake Myvatn, Iceland (Pogge von Strandmann et al., 2016) to infer the role of climatic and geological factors on the Yukon River geochemistry. Li concentrations in the Yukon River Basin range from 98 to 3737 nM, and the riverine δ^7Li values range +8.5 to +33.0 ‰. The Li concentration of the mainstream Yukon River (average ~430 nM; 235 nM at the mouth) is twice as higher as the global mean of 215 nM (Huh et al., 1998; Murphy et al., 2019). The mean of riverine δ^7Li in the Yukon River Basin is 18.3 ± 3.5 ‰. The Lower Yukon, which displays a distinctive higher mean riverine δ^7Li value of 25.9 ‰. A general positive relationship of δ^7Li and 1/[Li] is observed (r = 0.66) for rivers across the Yukon River Basin (Fig.24A), showing increasing δ^7Li with decreasing Li concentration in the dissolved load. A strong positive relationship can be observed in the Tanana, Koyukuk, East Central Yukon and Porcupine catchments (Fig.24A). Other catchments underlain by continuous permafrost, such as the Porcupine and mountainous Koyukuk, also show a strong positive relationship (Fig.24A). The Chalandar drainage basin, underlain by continuous permafrost, is the only basin that does not display a significant positive relationship. Overall, most of the Yukon River catchments do not display a simple relationship between δ^7Li and Li concentration, suggesting a range of processes influencing a variation of δ^7Li and Li concentrations (Fig.24A). Li concentrations and δ^7Li values of the Lena River, Mackenzie River and Lake Myvatn are 12-1524 nM (7.1-41.9 ‰), 50-1290 nM (9.3-29.0 ‰) and 91-10050 nM (4.9-27.2 ‰), respectively. When comparing δ^7Li vs. Li concentration trend between the Yukon River and other northern basins, we find that the Yukon River has the steepest slope and does not display a flattening of the curve for lower Li concentration (Fig.24B).

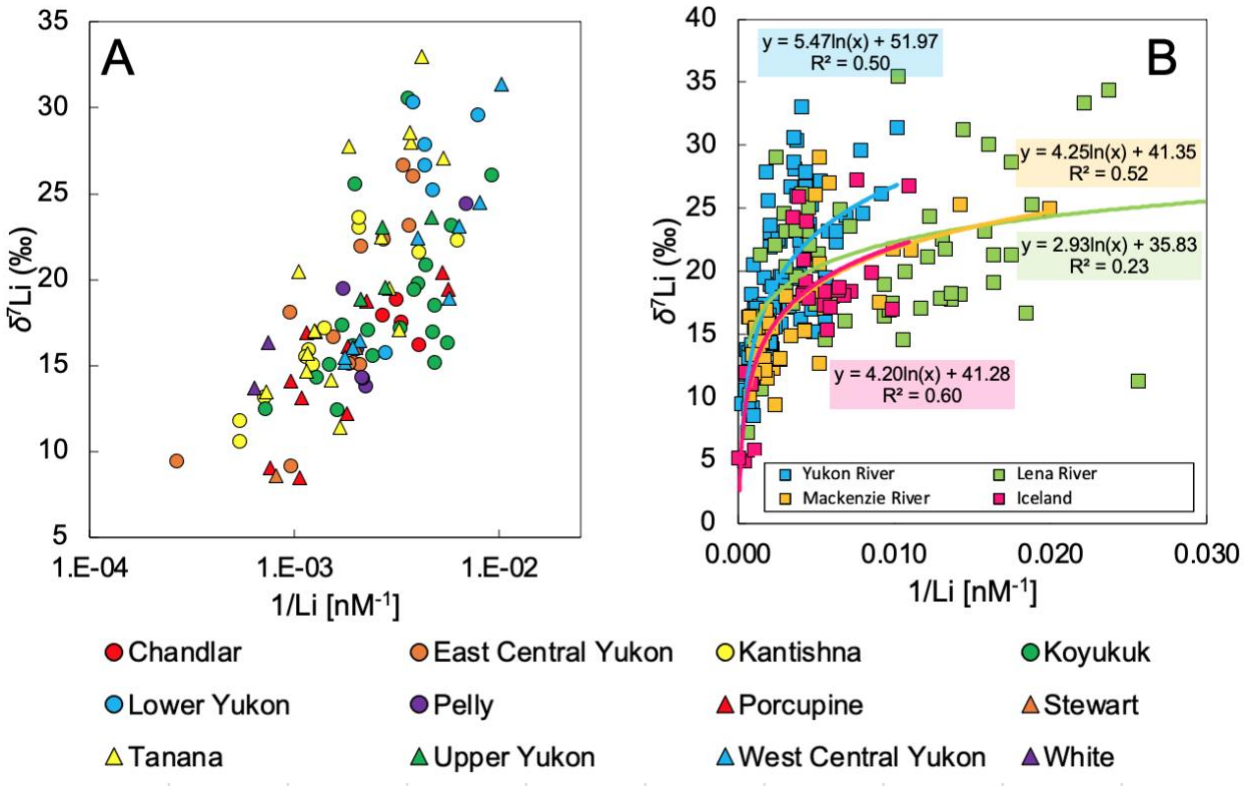

Figure 24: δ^7Li versus the inverse of dissolved Li concentrations. (A) rivers classified into major drainage basins across the Yukon River Basin. (B) comparison of the Yukon River to a similar environmental setting: Lena River (Murphy et al., 2019), Mackenzie River (Millot et al., 2010) systems and Lake Myvatn, Iceland (Pogge von Strandmann et al., 2016).

6.6 Li isotopes variations and climate control

The riverine δ^7Li values show a broad positive relationship with permafrost cover and mean air temperature. However, the relationship is not linear. The riverine δ^7Li values observed in the catchments underlain by continuous permafrost (the Porcupine and mountainous Koyukuk) range from +4 to +26‰. However, for these catchments cover with continuous permafrost, δ^7Li values remain on average around 15‰ until they reach a threshold of ~-6°C. Above this threshold, δ^7Li values increase linearly (Fig.25). Catchments underlain by discontinuous permafrost (the lowlands of Koyukuk, East Central Yukon, Kantishna, and part of Tanana) show higher values and a greater variability (+4 to +30‰). Catchments covered with

sporadic permafrost (the West Central Yukon, Lower Yukon, Pelly and part of Tanana) display the highest δ^7Li values and largest variations (+4 to +34‰).

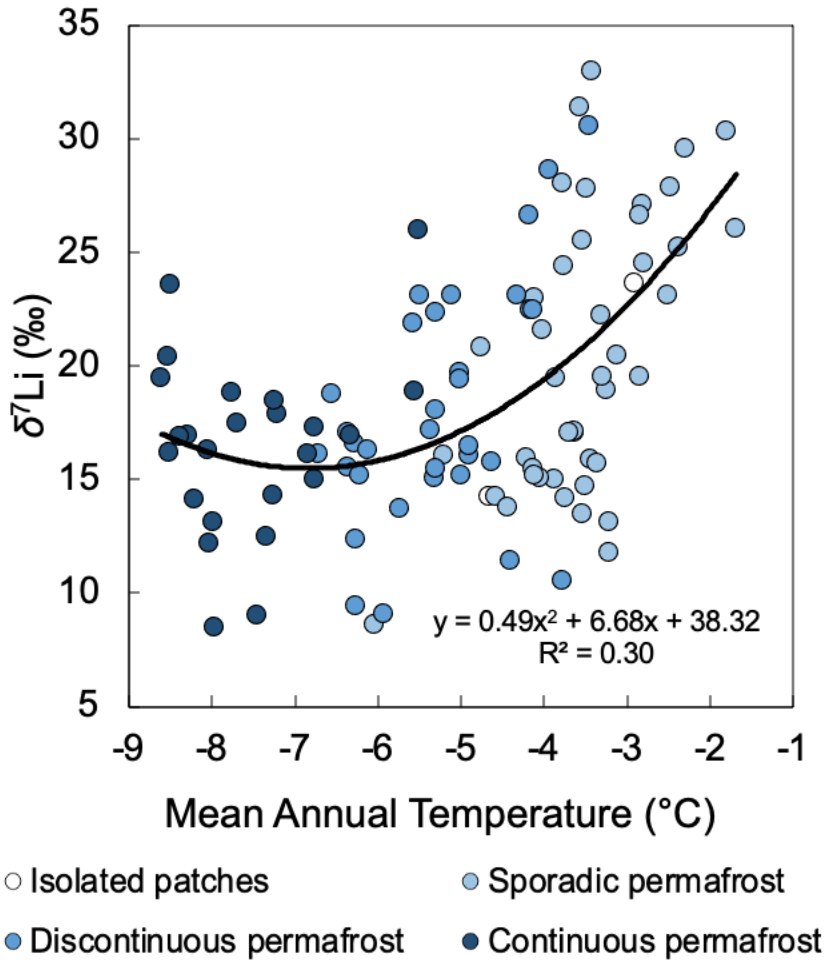

Figure 25: The riverine δ^7Li values plotted against mean air temperature. The gradient of color in the symbols indicate different coverage of permafrost dark blue to lower permafrost coverage light blue.

The spatial riverine δ^7Li variations are compared to permafrost coverage across the Yukon River Basin (Fig.26). The headwater and its surrounding regions are underlain by sporadic permafrost and brunisols (Fig.8 and 12). The headwater of the Yukon River displays intermediate riverine δ^7Li values (+16 to +24‰), with one tributary having high δ^7Li values of

~24‰ and most other tributaries having δ^7Li values lower than 20‰. The surrounding region of headwater, including the Stewart and Pelly rivers, displays low riverine δ^7Li values (<16‰). As the Yukon River flows westward, the permafrost coverage increases from sporadic to discontinuous/continuous permafrost. In this region, the riverine δ^7Li values are very variable, ranging from +8 to +24‰. The northern part of the basin, including the Porcupine, Chalandar, and mountainous Koyukuk, is mostly underlain by continuous permafrost. The regions dominated by continuous permafrost have low riverine δ^7Li values ranging from +8 to +16‰, and the regions with discontinuous permafrost have slightly greater riverine δ^7Li variations from +12 to +24‰. The Tanana, underlain by mostly discontinuous permafrost, displays a great variation of riverine δ^7Li values (+11 to +24‰) though low values dominate the headwaters. The highest riverine δ^7Li values are observed in the Chena River, a tributary of the Tanana (+22 to +33‰). The Lower Yukon and lowlands of the Koyukuk are underlain by sporadic to discontinuous permafrost, displaying high and variable riverine δ^7Li values (+16 to +33‰).

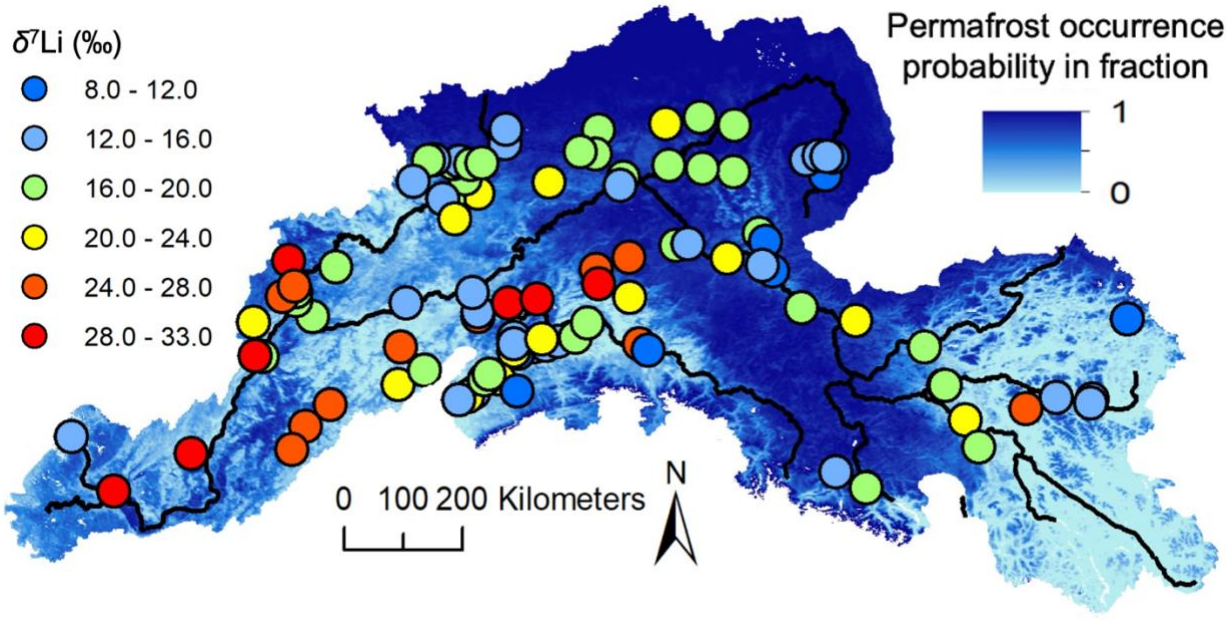

Figure 26: The variation of riverine δ^7Li plotted on different permafrost coverage displayed from dark (permafrost-dominated) to light colour (no permafrost) across the Yukon River Basin. The black line represents the main Yukon River.

6.7 Random forest regression results

The trained random forest regression model using the VSURF procedure identified two dominant predictors, mean air temperature and glacier cover (Fig.27), to predict riverine δ^7Li variations among the 21 tested environmental variables (Table 2). After the 10-fold cross-validation, the model explains 67% of the variance with an RMSE of 3.34‰ over the testing datasets (Fig.28).

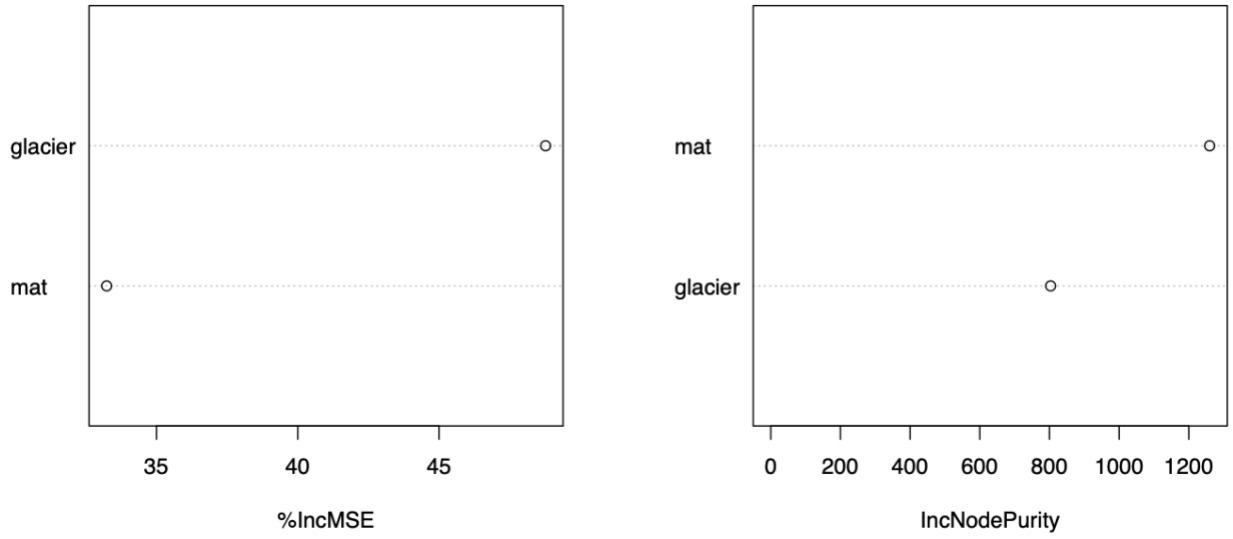

Figure 27: Variable importance plots for the best performing random forest models. (A) shows the increase of the Mean Squared Error in %. The higher the percentage, the more important variable it is. (B) shows the mean decrease gini score. The higher the score, the more important variable to the model.

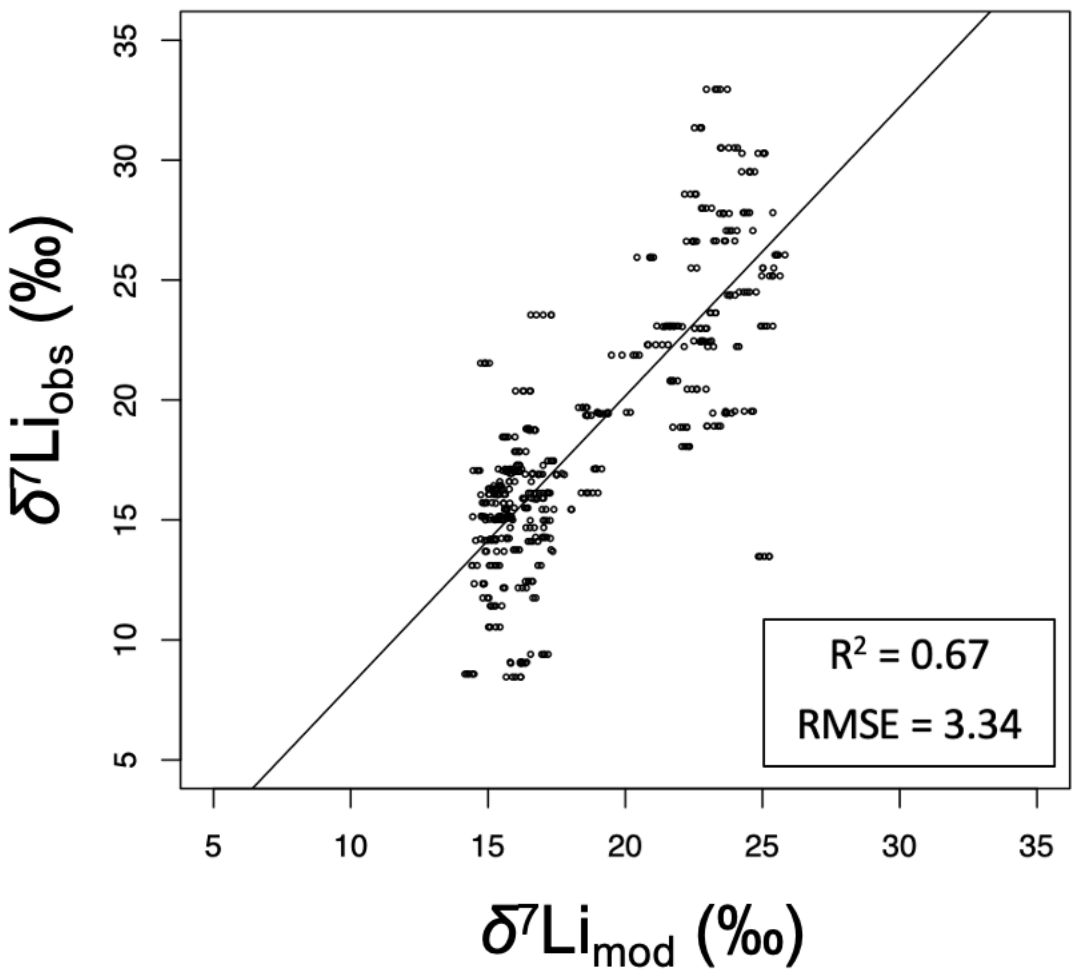

Figure 28: Scatter plots of observed vs. predicted riverine δ^7Li values. R^2 = coefficient of determination; RMSE = root mean square error.

7. Discussion

This thesis aims to demonstrate a better understanding of the weathering processes across the Yukon River Basin using elemental and isotopic data. This includes evaluating how lithological and topographic controls weathering processes across the Yukon River Basin but also assessing the potential role of permafrost cover on weathering processes by comparing the riverine δ^7Li sampled from catchments with different permafrost cover. In this discussion, we will first focus on untangling the geological and topographic controls of weathering processes and will then focus on the sensitivity of weathering intensity to temperature and permafrost cover.

7.1 Sources of dissolved Li and Sr in the Yukon River and the role of geology

In this section, we summarize the role of geology in controlling the hydrochemistry of the Yukon River Basin. In this study, we first note that we did not analyze anion concentrations in river samples and could not calculate the contribution of atmospheric sources in the river. Other studies on large northern rivers, including the Mackenzie River (Millot et al., 2010), Amazon River (Dellinger et al., 2015) and Lena River (Murphy et al., 2019), demonstrated that the atmospheric input to river waters is negligible. While the measured elemental data have not been corrected for the atmospheric input, we assumed that this effect is negligible.

As seen for other large river basins, the Mackenzie (Millot et al., 2010), the Amazon (Dellinger et al., 2015) and the Ganges (Pogge von Strandmann et al., 2017), the Yukon River weathering is controlled by mixing of carbonate and silicate sources. The differential contribution of these lithological sources exerts a major influence on the spatial hydrochemical patterns of the Yukon River. The presence of marine carbonate units and other marine sediments exert a strong control on alkali earth metal concentrations in different tributaries. Conversely, the type and age of silicate rock units, the presence of easily weatherable volcanic rocks exert a strong impact on the concentrations of other major elements (e.g., Na, K). In general, the Yukon River is a basin where both carbonate and silicate rock units contribute to the hydrochemistry throughout the basin. The elemental ratio plots (Fig.19A-D) show clear evidence for mixing between silicate and carbonate weathering in all the tributaries. Tributaries dominated by carbonate and marine sediments bedrock (e.g., Porcupine) tend to have a composition that

resembles more carbonate endmembers, whereas other tributaries dominated by silicates (e.g., Tanana) tend to plot towards the siliciclastic endmembers. This is consistent with other large rivers basins in the Arctic and elsewhere where the dissolved components are always reflecting a mixture of silicate and carbonate rocks in the Mackenzie (Millot et al., 2010), the Amazon (Dellinger et al., 2015), and the Ganges Rivers (Pogge von Strandmann et al., 2017).

Strontium isotopes allow us to distinguish further the contribution of carbonate vs. different silicate units on the basin (Fig.20A). Hyperbolic mixing lines show some interesting patterns related to the geology of each catchment, regional trends with a different proportion of three endmembers of carbonates, radiogenic silicates and non-radiogenic silicates (Fig.20A). The Lower Yukon and a part of West Central Yukon and lowlands Koyukuk show a significant contribution of less radiogenic silicates (Fig.21A) consistent with the presence of younger volcanic, volcaniclastic, and plutonic rocks ranging from Late Paleozoic to Early Cretaceous in age (Patton & Box, 1989). The rock units of this Koyukuk terrane are young and have low $^{87}Sr/^{86}Sr$ ratios, which are propagated into the rivers draining these areas. These catchments tend to plot closer to the unradiogenic silicate endmembers on the hyperbolic mixing lines (Fig.21A). This observation likely reflects the higher weathering rate of young volcanic rock units relative to other silicate rock units (Hartmann et al., 2014).

The Tanana River and other rivers in the Dawson Range region mostly drain the Yukon-Tanana terrane. This terrane is composed of an old felsic Precambrian metamorphic unit with very high $^{87}Sr/^{86}Sr$ ratios (Fig.21A). The Dawson Range region was not glaciated during the last glacial maximum, and as a result, deep flow paths have developed in this region with a fractured aquifer (Verplanck et al., 2008). This allows a strong connection with deep groundwater, which may explain the high elemental data and significantly high riverine $^{87}Sr/^{86}Sr$ (>0.720) on the western part of the Yukon-Tanana terrane. Bataille et al. (2014) and Brennan et al. (2014) had also identified this zone of extremely radiogenic rivers around the Yukon-Tanana terrane.

The upper and lower Koyukuk display varied geology on its catchment (Fig.7), coinciding with varied geochemistry and riverine $^{87}Sr/^{86}Sr$ and $\delta^{7}Li$ values (Fig.21). The upper Koyukuk is underlain by discontinuous permafrost (Fig.12) and is primarily composed of Paleozoic siliciclastic and carbonate rock units in the Brooks Range (Fig.21). In contrast, the lower Koyukuk has lowlands (Fig.6) that are predominantly composed of volcanic units of the

Koyukuk terrane (Fig.21) and underlain by sporadic permafrost (Fig.12). The distribution and influences of topography and climatic controls will be discussed in the following sections. We observed an increased contribution of carbonate weathering for rivers located at a high elevation within the Koyukuk drainage basin (Fig.19 and 20). Brennan et al. (2014) demonstrated in Alaska that the tributaries located in lowlands display less carbonate weathering relative to the rivers at higher elevation due to the increased physical erosion rates at high relief, promoting the exposure of carbonates (Beikman, 1980; Wilson et al., 1998; Brennan et al., 2014). However, in the Brooks Range, the higher contribution of carbonates does not lead to lower $^{87}Sr/^{86}Sr$; rather, $^{87}Sr/^{86}Sr$ tend to remain high even in carbonate dominated catchments (Fig.20). This observation is a bit unusual as carbonates are usually unradiogenic (~0.708) (Veizer et al., 1999). In this case, radiogenic carbonates appear to contribute to the riverine $^{87}Sr/^{86}Sr$. Radiogenic carbonates can occur when metamorphism exchanges radiogenic strontium with surrounding silicate lithologies (e.g., Himalaya) (Bickle et al., 2001). As the Brooks Range contains some significant metalimestone and marble units, it is possible that some of this unit are more radiogenic and contribute to the elevated $^{87}Sr/^{86}Sr$ in mountainous regions of the Brooks Range in addition to the lithological difference between the upper and lower Koyukuk drainage basin (Fig.21A).

Carbonate weathering influences $^{87}Sr/^{86}Sr$ variations, but its impact on δ^7Li values should be minimal as Li is mainly hosted in silicate rocks, and most of the riverine Li is derived from silicate weathering (Kisakurek et al., 2005). Other river basins, including the Himalayan (Kisakurek et al., 2005), the Mackenzie (Millot et al., 2010), the Amazon (Dellinger et al., 2015) and the Ganges Rivers (Pogge von Strandmann et al., 2017), identified that the dissolved Li is mainly derived from silicate weathering and the contribution of carbonate weathering is negligible. We identified some trends between δ^7Li and $^{87}Sr/^{86}Sr$, indicating a possible influence of geology and lithology on δ^7Li variations (Fig.22). To date, it had been assumed that δ^7Li variations in rivers were mostly independent of lithology and reflected weathering intensity (Kisakurek et al., 2005; Millot et al., 2010) through the presence of recycled sediments might contribute to δ^7Li variations (Dellinger et al., 2017). We were not expecting any strong covariation between lithology and δ^7Li values. However, in this study, we show that catchments characterized by intermediate $^{87}Sr/^{86}Sr$ (0.710-0.720) corresponding to a mixture of silicate and carbonate sediments also display relatively low δ^7Li values (+8‰ to +24‰). Conversely, catchments draining very radiogenic metamorphic or unradiogenic igneous rock units (e.g.,

Koyukuk, Tanana) tend to have much higher δ^7Li values. We argue that lithology has a stronger influence than previously recognized on δ^7Li variations over a large scale and influence weathering intensity (Kisakurek et al., 2005; Millot et al., 2010). We hypothesize that this link with lithology on the catchment is probably related to both δ^7Li variations between lithologies and sensitivity to erosion rate. In catchments dominated by igneous lithologies with δ^7Li values ~ 0‰ (e.g., volcanic or meta-igneous rocks), primary mineral supply is high and facilitates the formation of secondary clay minerals favouring high δ^7Li values. Conversely, in regions dominated by reworked sediments with negative δ^7Li values (Dellinger et al., 2017) and away from igneous sources, the supply of fresh primary mineral is more restrained, limiting secondary mineral formation in soils developing on these sediments and leading to lower δ^7Li values. This previously unrecognized lithological control on δ^7Li values in the dissolved load is particularly obvious in the lower Koyukuk and Lower Yukon basins, where young volcanic rock units lead to very high δ^7Li values. In these regions, the rate of clay formation is probably elevated relative to the rest of the basin. The influence of lithology on δ^7Li values is also observable when plotting 1/Li vs. δ^7Li values (Fig.24B). For most of the other Arctic basins, δ^7Li values flatten for lower Li concentrations in more erosion limited areas (Fig.24B). Even when Li concentrations are low in the Yukon River, δ^7Li values remain high likely because glaciers on the basin and young igneous rocks provide a large supply of fresh primary minerals. Other basins studied in the Arctic, such as the Lena and the Mackenzie rivers, drain areas that are flatter and characterized by older and more recycled rock units (Millot et al., 2010; Murphy et al., 2019). The Yukon River Basin has more variable geology juxtaposing very young terrane (e.g., Koyukuk) with cratonic and Precambrian terrane (e.g., Yukon-Tanana). This juxtaposition creates a contrast between the higher weathering intensity of young volcanic and other igneous terranes with a high supply of primary mineral to their floodplains and more catchments draining more recycled rock units (e.g., Porcupine).

We conclude that a large portion of the hydrochemical variations, including δ^7Li variations observed on the Yukon River, is related to geological and lithological controls that are inherent to the geological history of this basin.

7.2 Catchment area and gradient controls on Li isotope fractionation

In addition to geology, catchment area and topography are expected to play a role in controlling the geochemistry of a river. Large catchments tend to have much less variable geochemistry and δ^7Li values, whereas smaller catchments tend to show higher variations. This trend is observed in the Yukon River Basin with δ^7Li values remaining within a tight range (13-20 ‰) for most large rivers, whereas larger variations of δ^7Li values are seen for small catchments (< 11,000 km^2) (Fig.29). Similar patterns were observed in other large rivers such as the Lena River, with great variability of δ^7Li displayed at smaller catchments and relatively constant δ^7Li at large catchments. Murphy et al. (2019) argued that local processes controlling the riverine δ^7Li values within smaller catchments are homogenized at large catchments.

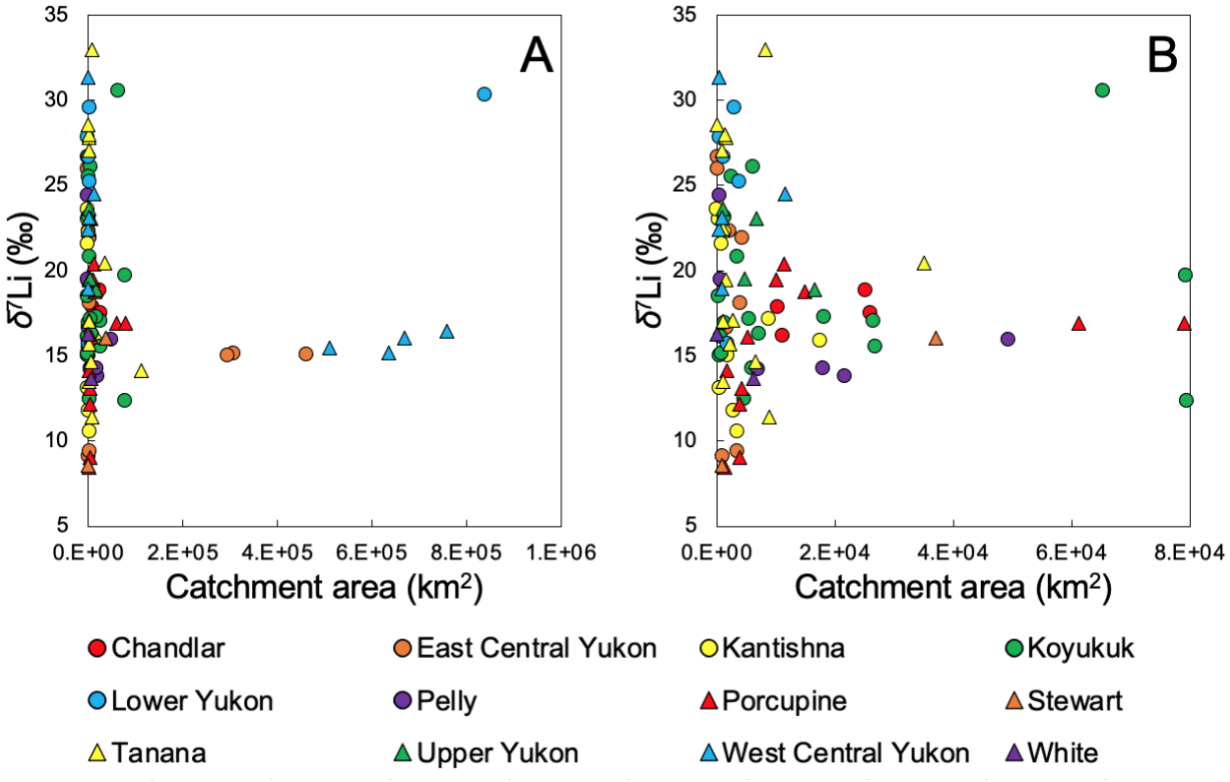

Figure 29: The riverine δ^7Li values plotted against the catchment area. (A) Full dataset. (B) Zoom on smaller catchments.

Topography exerts a direct influence on weathering intensity, and it is directly reflected in riverine δ^7Li values (Fig.3). The Yukon River has a very mountainous catchment, and high mountainous regions have an elevated erosion rate that transports weathered materials downstream in the floodplains. In the headwaters, the dissolution rate of a primary mineral is high leading to high Li flux, but the formation of secondary minerals is limited due to the high erosion rate and limited residence time of minerals (Fig.3). Therefore, the high elevated regions show low riverine δ^7Li values. On the contrary, at low-lying lands, the physical erosion rate is lower, and primary minerals have more time to weather, leading to a higher secondary mineral formation rate (Fig.3). This link between topography, residence time and δ^7Li values has been observed in other rivers with high elevation mountains such as the Ganges River (Pogge von Strandmann et al., 2017) and the Himalaya rivers (Kisakurek et al., 2005). Riverine δ^7Li values in low-lying regions of the Yukon River tend to be higher than those in high mountainous regions.

We calculated the channel slope of the watershed to evaluate further the effect of topography on δ^7Li variations (Fig.30). The channel slope calculation, performed in the ArcGIS, is calculated by dividing the length of each river segment by the elevation from the upstream to downstream points of the segment. The catchments draining mountain zones have a higher channel slope than the low-lying regions. As expected, many of these mountainous catchments (e.g., Koyukuk, Tanana, West Central Yukon, and East Central Yukon) display low δ^7Li values in their headwaters and higher δ^7Li values in their floodplains (Fig.30). In general, we find a negative correlation between δ^7Li values and channel slope though this correlation is relatively weak because of many other factors than topography influence weathering intensity.

The Koyukuk catchments represent a good example of how topography influences weathering and riverine δ^7Li values within the Yukon River Basin. The Koyukuk catchment is bordered by the Brooks Range on the north and has uplands and flats more downstream. The riverine δ^7Li values in tributaries draining high mountains are low (<16‰), whereas those draining the lower Koyukuk floodplains are high (>20‰). The high mountain ranges have a high primary mineral supply from high erosion rates, but weathering reactions are limited due to the low residence time of minerals in these areas and the absence of soils (Fig.3). The secondary mineral formation rate is also low, limiting the fractionation of Li isotopes associated with the

secondary mineral formation and absorption and leading to low riverine δ^7Li values. Conversely, the lower Koyukuk receives a large amount of fresh primary minerals from these eroding mountains. The stored sediments remain on the flatter floodplains for a longer time period and can weather and form secondary minerals (Fig.3) and resulting in high riverine δ^7Li values. This relationship between topography and riverine δ^7Li values is observed in many basins across the world, such as the Amazon River (Dellinger et al., 2015; Fig.4A), where the high riverine Li concentrations and low riverine δ^7Li values are observed in the mountain ranges, and lower riverine Li concentrations with high riverine δ^7Li values are seen in the lowlands. However, the Yukon River Basin does not display the same parabolic relationship observed in the Amazon River, where Li concentration decrease and δ^7Li values decrease closer to the mouth of the river. In this tropical setting, weathering rates are high, thick soils form, and when erosion becomes limited, dissolution of secondary mineral becomes the main source of Li. In the Yukon River, as in other high latitude catchments, this transport-limited regime does not occur because weathering reaction rates are low and erosion rates are high in high latitudes (Murphy et al., 2019; Fig.4B). Rather the Yukon River displays a similar trend to other northern rivers (Fig.24B).

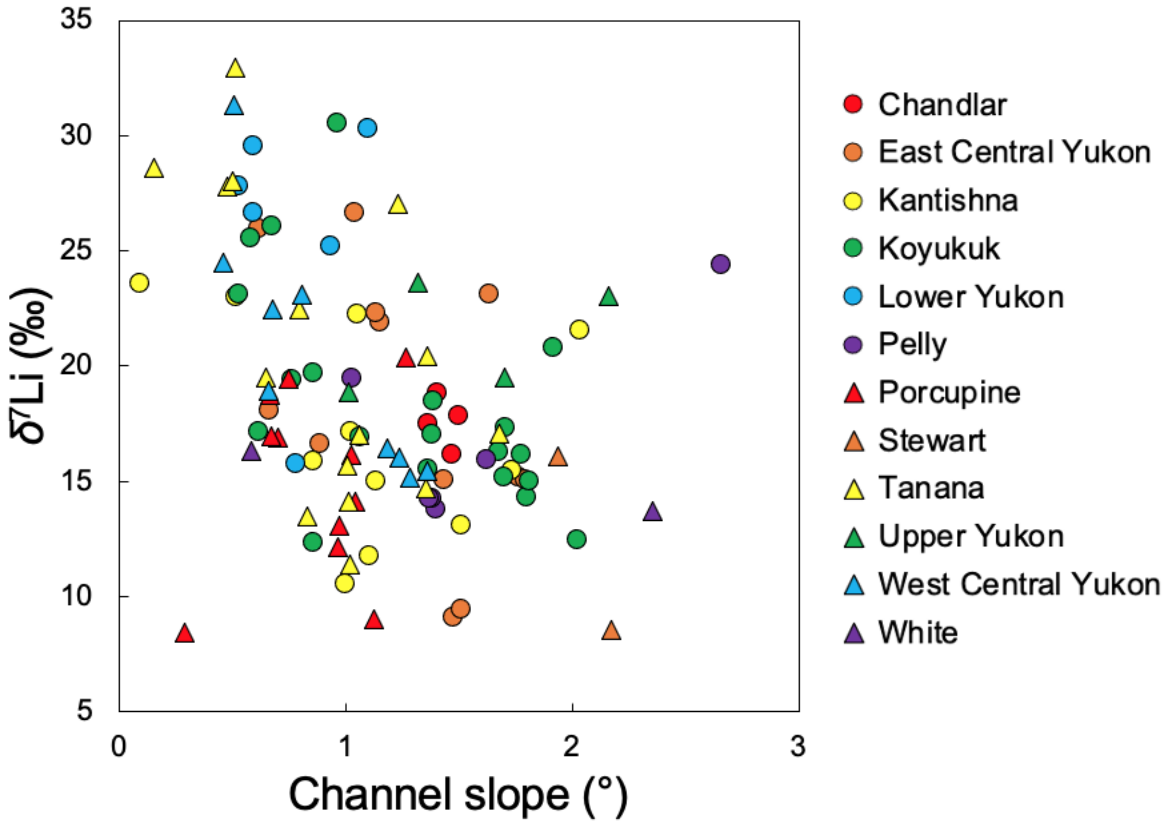

Figure 30: The riverine δ^7Li values plotted against the channel slope.

The covariation between δ^7Li values and residence time is another indication of the role of topography on weathering processes in the Yukon River Basin. Previous studies used a combination of δ^7Li values and Li/Na ratios to infer water-rock interaction time (Millot et al., 2010; Dellinger et al., 2015; Pogge von Strandmann et al., 2017; Murphy et al., 2019). The observed negative correlation between Li/Na ratios and riverine δ^7Li values in Fig.31A agrees with the trends shown in other studies (Millot et al., 2010; Dellinger et al., 2015; Liu et al., 2015; Bagard et al., 2015; Pogge von Strandmann et al., 2017; Murphy et al., 2019) and provide information about the relationship between Li removal into secondary minerals and Li isotopes fractionation (Pogge von Strandmann et al., 2010, 2017; Bouchez et al., 2013; Dellinger et al., 2014; Bagard et al., 2015; Murphy et al., 2019). The fractionation of Li is directly related to the secondary mineral formation rate. During the primary mineral dissolution, Li and Na are assumed to be released congruently to water, and the dissolution does not lead to any Li isotope fractionation (Pistiner & Henderson, 2003; Teng et al., 2007; Qiu et al., 2009; Wimpenny et al.,

2010). Li fractionation occurs during the secondary mineral formation where ^{6}Li from water is absorbed onto the secondary mineral surface or trapped within its interlayer, resulting in increasing δ^{7}Li values of water. Therefore, the Li/Na ratio is progressively diminished with ongoing weathering reactions and secondary mineral formation.

The riverine δ^{7}Li values of the Yukon River increase with decreasing Li/Na ratios (Fig.31A) as observed in rivers and lakes under similar environmental conditions (Pogge von Strandmann et al., 2016; Murphy et al., 2019) (Fig.31B). We used a simple Rayleigh distillation isotopic fractionation model to estimate the fractionation occurring during weathering processes on the Yukon River to identify the type of secondary mineral forming. During secondary mineral formation, ^{6}Li is incorporated into secondary minerals; water becomes depleted in ^{6}Li, which increases the δ^{7}Li of the water. This Rayleigh distillation relationship controlled by the fractionation factor (α) reflects the preferential removal of ^{6}Li with:

$$\delta^{7}Li_{diss} = \delta^{7}Li_{0} + 1000(\alpha - 1)\ln\left(f_{diss}^{Li}\right) \ldots \text{Eq 2}$$

Where $\delta^{7}Li_{diss}$ is the dissolved δ^{7}Li value, and $\delta^{7}Li_{0}$ is the value for Li released into the water, the representative value for the mean upper continental crust, 0‰, is used for a starting isotopic composition ($\delta^{7}Li_{0}$). f_{diss}^{Li} is the fraction of Li remaining in solution, calculated with the following equation:

$$f_{diss}^{Li} = \frac{Li/Na_{diss}}{Li/Na_{0}} \ldots \text{Eq 3}$$

Where the Li/Na_{0} molar ratio is 0.0105, the highest dissolved value found in the Yukon River, and a value of 0.1, which is that of the upper continental crust (Taylor & McLennan, 1995; Murphy et al., 2019), were used in the model calculations. Six fractionation lines were generated (Fig.31A) using 0.0105 and 0.1 as the Li/Na_{0} molar ratios.

All data, except one outlier, fall within α values ranging between 0.990 and 0.997. The experimentally determined values for secondary minerals within α range in the Yukon River

Basin include $\alpha_{smectite}$ = 0.983-0.997, $\alpha_{gibbsite}$ = 0.984-0.993, $\alpha_{ferrihydrite}$ = 0.998 and $\alpha_{kaolinite}$ = 0.992 (Pistiner & Henderson, 2003; Vigier et al., 2008; Wimpenny et al., 2015; Li & Liu, 2020). The range of fractionation factors determined for the Yukon River are in good agreement with the Lena River (Murphy et al., 2019) and fall within the range of swelling clays like smectites. However, Millot et al. (2010) and Wimpenny et al. (2010) also suggested that clay formation is very limited in permafrost-covered areas. Despite this low clay formation rate, some Li fractionation is observed in these permafrost-covered catchments. They hypothesize that fractionation in permafrost-dominated catchments could be associated with the absorption of Li onto Fe/Mn oxyhydroxide mineral surfaces during the secondary mineral formation. The range of observed fractionation in the Yukon River is within that of Fe/Mn oxy-hydroxide like ferrihydrite, which is abundant in most organic Arctic soils (Herndon et al., 2017). It is possible that part of the lithologically driven δ^7Li variations mentioned above is related to the formation of different secondary minerals (Hindshaw et al., 2018). Fe/Mn oxy-hydroxide might be more prevalent in igneous areas, particularly when weathering Fe-rich young mafic rock units.

The range of fractionation factors summarizes the behaviour of Li in the catchment that riverine δ^7Li values increase with increased water-rock interaction (reflected in low Li/Na ratio). The catchments located in high mountainous regions display low riverine δ^7Li values with high Li/Na ratios because of high physical erosion rates in these regions resulting in short water-rock interaction time. Low weathering intensity and low secondary mineral formation rates at high mountainous regions result in less Li fractionation as reflected on low riverine δ^7Li values. In contrast, the catchments in the lowlands have an increased secondary mineral formation rates as the sediments in the flattened floodplains allow a longer water-rock interaction time resulted from high weathering intensity and low erosion rates. This is reflected in high riverine δ^7Li values with low Li/Na ratios. However, other local processes might affect the variations of fractionation factors of the riverine Li isotope compositions. A possible process that occurs within the local catchment levels and may influence riverine δ^7Li values significantly is groundwater contribution to surface water that causes the mixing of water sources with different Li characteristics (Négrel et al., 2010).

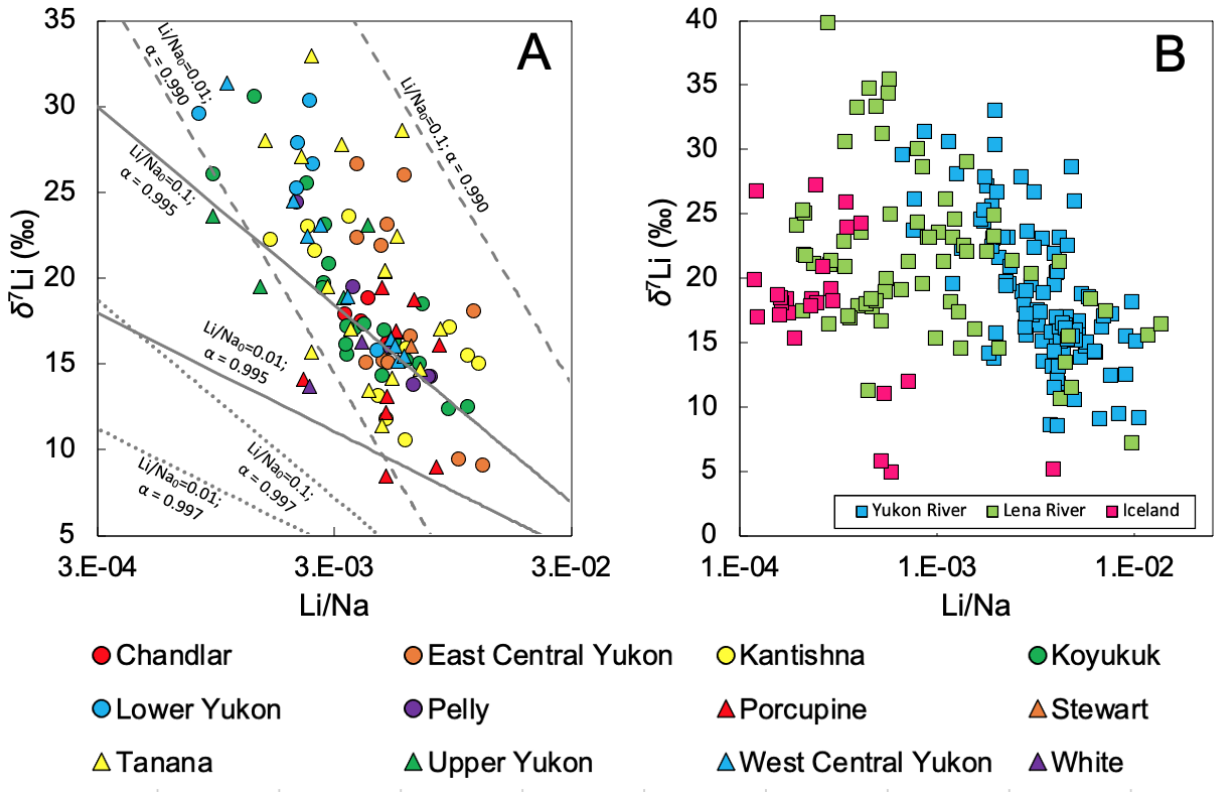

Figure 31: The riverine δ^7Li values versus Li/Na ratios. (A) Major drainages in the Yukon River Basin. (B) Yukon River Basin compared to the Lena River Basin (Murphy et al., 2019) and Lake Myvatn, Iceland (Pogge von Strandmann et al., 2016).

7.3 Climatic and permafrost controls on Li isotope

About a quarter of the northern hemisphere is covered with permafrost (Obu et al., 2019; Fig.2). The Yukon River shows a great range of permafrost cover (Zhang et al., 1999). Previous studies conducted in river systems that are under similar climatic settings, such as the Lena River (Murphy et al., 2019), the Mackenzie River (Millot et al., 2010) and rivers in Iceland (Pogge von Strandmann et al., 2010), suggest that the climatic conditions are not a dominant factor influencing the riverine δ^7Li variations and weathering processes. In this study, we wanted to test this idea by working on a river system with a broad range of permafrost cover. We show that that mean air temperature is correlated with δ^7Li variations (Fig.25). The mean annual temperature is strongly related to permafrost distribution across the Yukon River (Fig.25).

All the Yukon River samples were collected during the summer when the active layer was the deepest. We acknowledge that seasonal variations in weathering processes could explain some of the variability between catchments. However, we tried to minimize the role of hydrology and seasonality between samples by collecting them during similar periods. We assumed that our sampling represents a snapshot of the weathering conditions during the late summer, and we compare the weathering conditions across a gradient of permafrost cover. Catchments with continuous permafrost generally display low riverine δ^7Li though the positive values observed in the dissolved load still demonstrate some fractionation occurs (Fig.26) (e.g., catchments in the Porcupine and mountainous Koyukuk). δ^7Li values in permafrost-dominated catchment tend to converge around 15‰, a value similar to what was observed on a large portion of the permafrost-covered area of the Mackenzie River (Millot et al., 2010). In permafrost-dominated catchments, the erosion rate could be elevated due to freeze-thaw processes, but primary minerals remain shielded from liquid water interactions limiting weathering reactions (Murphy et al., 2019). Consequently, the weathering intensity is low because low temperatures limit the kinetic reactions (Chen & Brantley, 1997). Millot et al. (2010) argued that Li fractionation in these conditions mostly occurs due to absorption on Fe/Mn oxyhydroxide (i.e., ferrihydrite). Additionally, recent work demonstrated that ferrihydrite plays an important role in controlling metal isotope fractionation in permafrost-covered environments (Hirst et al., 2020) and could explain the relatively homogeneous δ^7Li values in permafrost dominated conditions. Ultimately, weathering intensity in the permafrost dominated area is low due to slow reaction kinetics and result in little fractionation of riverine Li isotopes (weathering-limited regime) (Fig.3). Conversely, in regions where the mean annual temperature goes above the threshold of permafrost thawing MAT > -6°C, weathering reactions can proceed in the active layer and non-glaciated areas. The thawing of permafrost favours higher water circulation, and higher soil temperature increase weathering reaction rates. In these non-glaciated soils, weathering intensity is higher than in catchments where permafrost is continuous. Therefore, the rate of secondary mineral formation (clays and Mn/Fe oxy-hydroxide) is promoted with increased weathering intensity, reflected on increased riverine δ^7Li values—the catchments with discontinuous or sporadic permafrost display higher and more variable riverine δ^7Li values than other glaciated catchments (Fig.26).

We conclude that, unlike other basins, permafrost cover and temperature are key factors in controlling regional weathering processes on the Yukon River.

7.4 Random forest regression model

The random forest regression selected glacier cover and temperature as the two most significant controls of δ^7Li variations (Fig.27). Together these two factors explained close to 70% of the majority δ^7Li variance (approximately 80%) across the Yukon River. These two factors summarize the climatic, topographic and geological controls on weathering intensity across the Yukon River. Glaciers are mostly present on very high mountain ranges (i.e., Alaska Range) and are thus highly correlated with topography. Consequently, the importance of glaciers as a predictor can be seen as a strong topographic predictor of δ^7Li variations. In addition, glaciers contribute to increasing erosion rates, further moving the system towards a weathering-limited regime. The high denudation rates on glacier-covered catchments would promote the release of cations to water by silicate weathering, but secondary mineral formation does not have time to proceed to the low residence time (Anderson et al., 1997). In contrast, the lower lands with no glacier have higher silicate weathering intensity due to decreased erosion rates and display higher riverine δ^7Li values (Fig.32A). We compared the riverine δ^7Li values of catchment glaciated today as well as during the last glacial maximum (Fig.32B). δ^7Li values are low in catchments containing glaciers today or that had glaciers in the LGM, suggesting that glacial cover increased erosion and lower weathering intensity across a longer timescale.

Another important control, temperature, is closely related to permafrost coverage, and both are strongly associated with weathering intensity. The influence of temperature on riverine δ^7Li values shows that the warmer the temperature, the higher the riverine δ^7Li variation becomes (Fig.25). In permafrost dominated catchments, weathering intensity is low due to the low temperature and to the absence of water-rock interactions on the surface. This results in a decrease in secondary mineral formation rates, reflecting low riverine δ^7Li values. The Porcupine catchments that are underlain by continuous permafrost display low riverine δ^7Li values (+8 to +16‰) (Fig.26). In contrast, in the catchments underlain by discontinuous permafrost, the weathering intensity increases with increasing temperature. The increased weathering intensity

promotes secondary mineral formation and formation of soils by increasing water-rock interaction time.

The two significant predictors of the random forest regression, glacier cover and temperature, suggest a strong control of climate variables on the riverine δ^7Li variation across the Yukon River Basin. However, each of these climatic predictors does not influence riverine δ^7Li values independently. They interact with other environmental, geological or climatic variables.

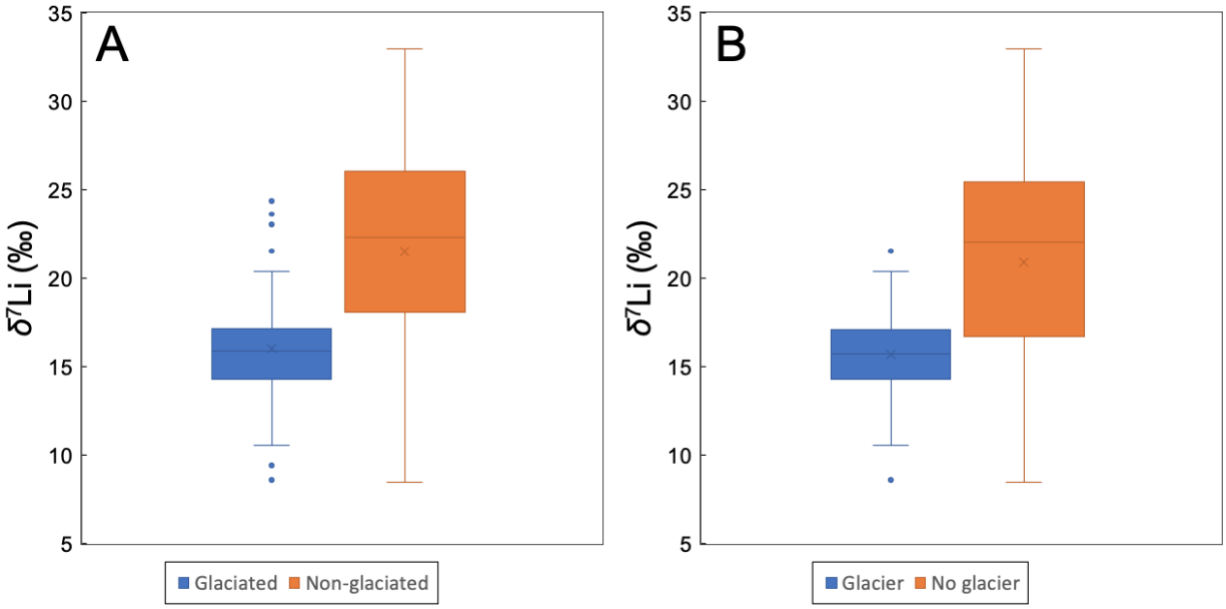

Figure 32: The riverine δ^7Li variations of (A) glacier rivers and non-glacier rivers and (B) glaciated and non-glaciated regions during the last glacial maximum.

8. Conclusion

This thesis explored the various environmental factors that influence weathering processes across the Yukon River Basin using lithium and strontium isotopes as geochemical tracers. The Yukon River Basin is a large catchment underlain by various geology, mountainous topography and a broad range of permafrost cover. However, the climate is rapidly changing across the Yukon River Basin and might influence the hydrochemistry and ecosystems. This thesis aimed to evaluate how weathering processes might change in the future with lower permafrost cover, lower alpine glacier cover and higher temperature.

We demonstrated that geological and lithological variables control a large part of the spatial hydrochemical variations observed across the Yukon River during the late summer. Strontium isotope data, coupled with elemental data, demonstrated that the hydrochemistry of tributaries across the Yukon River reflected their geology. The interplay between carbonate and silicate weathering observed in all rivers is modulated by the lithology of silicates (e.g., mafic vs. felsic) and by other topographic, climatic and environmental controls. Riverine Li isotopes also show some lithological controls with regions dominated by igneous lithology having higher δ^7Li values relative to regions dominated by siliciclastic sediments suggesting higher weathering intensity in this geological setting. This higher weathering intensity is possibly linked to the higher supply of fresh primary minerals available for weathering reactions in watersheds cover by igneous and metamorphic rock units. Conversely, in watershed draining recycled sedimentary units from older formations, fresh primary minerals are less available, leading to lower weathering intensity. The Yukon River Basin has a high proportion of igneous and metamorphic rock units relative to other areas on the globe, in part due to the successive accretion of arc terranes to the North American craton. This igneous-rich geology makes the Yukon River more susceptible to change in weathering intensity than other studied Arctic Rivers (e.g., Lena, Mackenzie).

Besides having dominantly igneous geology, the Yukon River is also a very mountainous watershed with some of the largest mountain ranges in the world. These mountains are covered by alpine glaciers that favour very high erosion rates. Both of these variables exert a strong influence on weathering processes. Mountain streams deliver a huge amount of fresh primary minerals to the floodplains of the Yukon River. This elevated erosion rate also favours an

elevated weathering intensity and weathering rate across the Yukon River Basin, particularly in areas with discontinuous permafrost.

Permafrost cover and temperature further modulate weathering processes on the floodplains. Despite the high supply of primary minerals due to high topography, glaciers and high igneous rock unit abundances, surface weathering is largely inhibited by low temperature and limited water rock-interactions in most areas covered by continuous permafrost. Only regions with mean annual temperature superior to -4°C show increasing and more variable weathering intensity with the formation of clays. As the temperature continues to increase across the basin and permafrost cover changes, we expect weathering intensity to continue increasing across the Yukon River. We predict that surface weathering will increasingly contribute to the hydrochemistry of the Yukon River, particularly in the late summer.

Bibliography

Ai, G., Sun, T., & Dong, X. (2014). Gas chromatography/isotope ratio mass spectrometry: Analysis of methanol, ethanol and acetic acid by direct injection of aqueous alcoholic and acetic acid samples. *Rapid Communications in Mass Spectrometry*, *28*(15), 1674–1682. https://doi.org/10.1002/rcm.6948

Albarède, F., Telouk, P., Blichert-Toft, J., Boyet, M., Agranier, A., & Nelson, B. (2004). Precise and accurate isotopic measurements using multiple-collector ICPMS. *Geochimica et Cosmochimica Acta*, *68*(12), 2725–2744. https://doi.org/10.1016/j.gca.2003.11.024

Angino, E. E., & Billings, G. K. (1966). Lithium content of sea water by atomic absorption spectrometry. *Geochimica et Cosmochimica Acta*, *30*(2), 153–158. https://doi.org/10.1016/0016-7037(66)90104-9

Ayotte, J. D., Gronberg, J. A. M., & Apodaca, L. E. (2011). Trace elements and radon in groundwater across the United States, 1992-2003. *Scientific Investigations Report (United States Geological Survey)*, *2011–5059*, i–xi, 1–115.

Bagard, M. L., Chabaux, F., Pokrovsky, O. S., Viers, J., Prokushkin, A. S., Stille, P., Rihs, S., Schmitt, A. D., & Dupré, B. (2011). Seasonal variability of element fluxes in two Central Siberian rivers draining high latitude permafrost dominated areas. *Geochimica et Cosmochimica Acta*, *75*(12), 3335–3357. https://doi.org/10.1016/j.gca.2011.03.024

Bagard, M. L., West, A. J., Newman, K., & Basu, A. R. (2015). Lithium isotope fractionation in the Ganges-Brahmaputra floodplain and implications for groundwater impact on seawater isotopic composition. *Earth and Planetary Science Letters*, *432*, 404–414. https://doi.org/10.1016/j.epsl.2015.08.036

Bataille, Clément P., & Bowen, G. J. (2012). Mapping 87Sr/ 86Sr variations in bedrock and water for large scale provenance studies. *Chemical Geology*, *304–305*, 39–52. https://doi.org/10.1016/j.chemgeo.2012.01.028

Bataille, Clément P., Brennan, S. R., Hartmann, J., Moosdorf, N., Wooller, M. J., & Bowen, G. J. (2014). A geostatistical framework for predicting variability in strontium concentrations and isotope ratios in Alaskan rivers. *Chemical Geology*, *389*, 1–15. https://doi.org/10.1016/j.chemgeo.2014.08.030

Bataille, Clement P., von Holstein, I. C. C., Laffoon, J. E., Willmes, M., Liu, X. M., & Davies, G. R. (2018). A bioavailable strontium isoscape for Western Europe: A machine learning approach. *PLoS ONE*, *13*(5), 1–27. https://doi.org/10.1371/journal.pone.0197386

Beikman, H. M. (1980). *Geologic Map of Alaska. U.S. Geological Survey, 1 sheet, scale 1: 2,500.000*.

Bentley, R. A. (2006). Strontium isotopes from the earth to the archaeological skeleton: A review. *Journal of Archaeological Method and Theory*, *13*(3), 135–187. https://doi.org/10.1007/s10816-006-9009-x

Berner, R. A. (1978). Rate control kinetic in Calcite dissolution under Earth surface conditions. In *American Journal of Science* (Vol. 278, pp. 1235–1252).

Bickle, M. J., Harris, N. B. W., Bunbury, J. M., Chapman, H. J., Fairchild, I. J., & Ahmad, T. (2001). Controls on the 87Sr/86Sr ratio of carbonates in the Garhwal Himalaya, Headwaters of the Ganges. *Journal of Geology*, *109*(6), 737–753. https://doi.org/10.1086/323192

Biskaborn, B. K., Smith, S. L., Noetzli, J., Matthes, H., Vieira, G., Streletskiy, D. A., Schoeneich, P., Romanovsky, V. E., Lewkowicz, A. G., Abramov, A., Allard, M., Boike, J., Cable, W. L., Christiansen, H. H., Delaloye, R., Diekmann, B., Drozdov, D., Etzelmüller, B., Grosse, G., … Lantuit, H. (2019). Permafrost is warming at a global scale. *Nature Communications*, *10*(1), 1–11. https://doi.org/10.1038/s41467-018-08240-4

Bohlin, M. S., Misra, S., Lloyd, N., Elderfield, H., & Bickle, M. J. (2018). High-precision determination of lithium and magnesium isotopes utilising single column separation and multi-collector inductively coupled plasma mass spectrometry. *Rapid Communications in Mass Spectrometry*, *32*(2), 93–104. https://doi.org/10.1002/rcm.8020

Bostock, H. S. (1970). *Physiographic regions of Canada*. https://doi.org/10.4095/108980

Bouchez, J., Von Blanckenburg, F., & Schuessler, J. A. (2013). Modeling novel stable isotope ratios in the weathering zone. *American Journal of Science*, *313*(4), 267–308. https://doi.org/10.2475/04.2013.01

Brabets, T. P., Browen, W., & Meade, R. H. (2000). *Environmental and Hydrologic Overview of the Yukon River Basin, Alaska and Canada Water-Resources Investigations Report 99-4204*.

Brabets, T. P., & Walvoord, M. A. (2009). Trends in streamflow in the Yukon River Basin from 1944 to 2005 and the influence of the Pacific Decadal Oscillation. *Journal of Hydrology*, *371*(1–4), 108–119. https://doi.org/10.1016/j.jhydrol.2009.03.018

Brand, W. A., Coplen, T. B., Vogl, J., Rosner, M., & Prohaska, T. (2014). Assessment of international reference materials for isotope-ratio analysis (IUPAC technical report). *Pure and Applied Chemistry*, *86*(3), 425–467. https://doi.org/10.1515/pac-2013-1023

Brass, G. W. (1976). The variation of the marine 87Sr86Sr ratio during Phanerozonic time: interpretation using a flux model. *Geochimica et Cosmochimica Acta*, *40*(7), 721–730. https://doi.org/10.1016/0016-7037(76)90025-9

Brennan, S. R., Fernandez, D. P., Mackey, G., Cerling, T. E., Bataille, C. P., Bowen, G. J., & Wooller, M. J. (2014). Strontium isotope variation and carbonate versus silicate weathering in rivers from across Alaska: Implications for provenance studies. *Chemical Geology*, *389*, 167–181. https://doi.org/10.1016/j.chemgeo.2014.08.018

Brenot, A., Cloquet, C., Vigier, N., Carignan, J., & France-Lanord, C. (2008). Magnesium isotope systematics of the lithologically varied Moselle river basin, France. *Geochimica et Cosmochimica Acta*, *72*(20), 5070–5089. https://doi.org/10.1016/j.gca.2008.07.027

Brown, J., Ferrians, O. J., Heginbottom, J. A., & Melnikov, E. S. (1997). Circum-Arctic map of permafrost and ground-ice conditions. In *Circum-Pacific Map*. https://doi.org/10.3133/cp45

Bryant, C. J., McCulloch, M. T., & Bennett, V. C. (2003). Impact of matrix effects on the accurate measurement of Li isotope ratios by inductively coupled plasma mass spectrometry (MC-ICP-MS) under "cold" plasma conditions. *Journal of Analytical Atomic Spectrometry*,

18(7), 734–737. https://doi.org/10.1039/b212083f

Burn, C. R. (2002). Tundra lakes and permafrost, Richards Island, Western Arctic coast, Canada. *Canadian Journal of Earth Sciences*, *39*(8), 1281–1298. https://doi.org/10.1139/e02-035

Capo, R. C., Stewart, B. W., & Chadwick, O. A. (1998). Strontium isotopes as tracers of earth surface processes: theory and methods. *Geoderma*, *82*, 197–225.

Casey, W. H., & Cheney, M. A. (1993). Brønsted reactions on oxide mineral surfaces and the temperature-dependence of their dissolution rates - Dedicated to Paul W. Schindler on his retirement. *Aquatic Sciences*, *55*(4), 304–313. https://doi.org/10.1007/BF00877275

Chan, L. H., Leeman, W. P., & You, C. F. (1999). Lithium isotopic composition of Central American Volcanic Arc lavas: Implications for modification of subarc mantle by slab-derived fluids. *Chemical Geology*, *160*(4), 255–280. https://doi.org/10.1016/S0009-2541(99)00101-1

Chan, Lui Heung, Alt, J. C., & Teagle, D. A. H. (2002). Lithium and lithium isotope profiles through the upper oceanic crust: A study of seawater-basalt exchange at ODP Sites 504B and 896A. *Earth and Planetary Science Letters*, *201*(1), 187–201. https://doi.org/10.1016/S0012-821X(02)00707-0

Chen, Y., & Brantley, S. L. (1997). Temperature- and pH-dependence of albite dissolution rate at acid pH. *Chemical Geology*, *135*(3–4), 275–290. https://doi.org/10.1016/S0009-2541(96)00126-X

Choi, M. S., Ryu, J. S., Park, H. Y., Lee, K. S., Kil, Y., & Shin, H. S. (2013). Precise determination of the lithium isotope ratio in geological samples using MC-ICP-MS with cool plasma. *Journal of Analytical Atomic Spectrometry*, *28*(4), 505–509. https://doi.org/10.1039/c2ja30293d

Coplen, T. B., Böhlke, J. K., De Bièvre, P., Ding, T., Holden, N. E., Hopple, J. A., Krouse, H. R., Lamberty, A., Peiser, H. S., Révész, K., Rieder, S. E., Rosman, K. J. R., Roth, E., Taylor, P. D. P., Vocke, R. D., & Xiao, Y. K. (2002). Isotope-abundance variations of selected elements (IUPAC technical report). *Pure and Applied Chemistry*, *74*(10), 1987–2017. https://doi.org/10.1351/pac200274101987

Crites, H., Kokelj, S. V., & Lacelle, D. (2020). Icings and groundwater conditions in permafrost catchments of northwestern Canada. *Scientific Reports*, *10*(1), 1–11. https://doi.org/10.1038/s41598-020-60322-w

Dellinger, M., Bouchez, J., Gaillardet, J., Faure, L., & Moureau, J. (2017). Tracing weathering regimes using the lithium isotope composition of detrital sediments. *Geology*, *45*(5), 411–414. https://doi.org/10.1130/G38671.1

Dellinger, M., Gaillardet, J., Bouchez, J., Calmels, D., Louvat, P., Dosseto, A., Gorge, C., Alanoca, L., & Maurice, L. (2015). Riverine Li isotope fractionation in the Amazon River basin controlled by the weathering regimes. *Geochimica et Cosmochimica Acta*, *164*, 71–93. https://doi.org/10.1016/j.gca.2015.04.042

Dellinger, M., Gaillardet, J. Ô., Bouchez, J., Calmels, D., Galy, V., Hilton, R. G., Louvat, P., & France-Lanord, C. (2014). Lithium isotopes in large rivers reveal the cannibalistic nature of

modern continental weathering and erosion. *Earth and Planetary Science Letters*, *401*, 359–372. https://doi.org/10.1016/j.epsl.2014.05.061

Derksen, C., Smith, S. L., Sharp, M., Brown, L., Howell, S., Copland, L., Mueller, D. R., Gauthier, Y., Fletcher, C. G., Tivy, A., Bernier, M., Bourgeois, J., Brown, R., Burn, C. R., Duguay, C., Kushner, P., Langlois, A., Lewkowicz, A. G., Royer, A., & Walker, A. (2012). Variability and change in the Canadian cryosphere. *Climatic Change*, *115*(1), 59–88. https://doi.org/10.1007/s10584-012-0470-0

Douglas, T. A., Blum, J. D., Guo, L., Keller, K., & Gleason, J. D. (2013). Hydrogeochemistry of seasonal flow regimes in the Chena River, a subarctic watershed draining discontinuous permafrost in interior Alaska (USA). *Chemical Geology*, *335*, 48–62. https://doi.org/10.1016/j.chemgeo.2012.10.045

Dürr, H. H., Meybeck, M., & Dürr, S. H. (2005). Lithologic composition of the Earth's continental surfaces derived from a new digital map emphasizing riverine material transfer. *Global Biogeochemical Cycles*, *19*(4). https://doi.org/10.1029/2005GB002515

Dusel-Bacon, C., Day, W. C., & Aleinikoff, J. N. (2013). Geochemistry, petrography, and zircon U-Pb geochronology of paleozoic metaigneous rocks in the mount veta area of east-central Alaska: Implications for the evolution of the westernmost part of the Yukon-Tanana terrane. *Canadian Journal of Earth Sciences*, *50*(8), 826–846. https://doi.org/10.1139/cjes-2013-0004

Ehlers, J., & Gibbard, P. L. (2007). The extent and chronology of Cenozoic Global Glaciation. *Quaternary International*, *164–165*, 6–20. https://doi.org/10.1016/j.quaint.2006.10.008

Emery, R., Klopfer, D. C., & Skalski, J. R. (1981). *Incipient toxicity of lithium to freshwater organisms representing a salmonid habitat*. http://inis.iaea.org/Search/search.aspx?orig_q=RN:12638295

Flesch, G. D., Anderson, A. R., & Svec, H. J. (1973). A secondary isotopic standard for 6Li/7Li determinations. *International Journal of Mass Spectrometry and Ion Physics*, *12*(3), 265–272. https://doi.org/10.1016/0020-7381(73)80043-9

Frey, K. E., & McClelland, J. W. (2009). Impacts of permafrost degradation on arctic river biogeochemistry. In *Hydrological Processes* (Vol. 23, Issue 1, pp. 169–182). John Wiley & Sons, Ltd. https://doi.org/10.1002/hyp.7196

Frey, K. E., Siegel, D. I., & Smith, L. C. (2007). Geochemistry of west Siberian streams and their potential response to permafrost degradation. *Water Resources Research*, *43*(3). https://doi.org/10.1029/2006WR004902

Gaillardet, J., Dupré, B., Louvat, P., & Allègre, C. J. (1999). Global silicate weathering and CO2 consumption rates deduced from the chemistry of large rivers. *Chemical Geology*, *159*(1–4), 3–30. https://doi.org/10.1016/S0009-2541(99)00031-5

Gaillardet, Jérôme, Millot, R., & Dupré, B. (2003). Chemical denudation rates of the western Canadian orogenic belt: the Stikine terrane. *Chemical Geology*, *201*, 257–279. https://doi.org/10.1016/j.chemgeo.2003.07.001

Gao, Y., & Casey, J. F. (2012). Lithium Isotope Composition of Ultramafic Geological

Reference Materials JP-1 and DTS-2. *Geostandards and Geoanalytical Research*, *36*(1), 75–81. https://doi.org/10.1111/j.1751-908X.2011.00117.x

Ge, S., Yang, D., & Kane, D. L. (2013). Yukon river basin long-term (1977-2006) hydrologic and climatic analysis. *Hydrological Processes*, *27*(17), 2475–2484. https://doi.org/10.1002/hyp.9282

Genuer, R., Poggi, J.-M., & Tuleau-Malot, C. (n.d.). *VSURF: An R Package for Variable Selection Using Random Forests*. Retrieved October 15, 2020, from http://cran.r-project.org/package=VSURF.

Gruber, S. (2012). Derivation and analysis of a high-resolution estimate of global permafrost zonation. *Cryosphere*, *6*(1), 221–233. https://doi.org/10.5194/tc-6-221-2012

Hallet, B., Hunter, L., & Bogen, J. (1996). Rates of erosion and sediment evacuation by glaciers: A review of field data and their implications. *Global and Planetary Change*, *12*(1–4), 213–235. https://doi.org/10.1016/0921-8181(95)00021-6

Hartmann, J., & Moosdorf, N. (2012). The new global lithological map database GLiM: A representation of rock properties at the Earth surface. *Geochemistry, Geophysics, Geosystems*, *13*(12). https://doi.org/10.1029/2012GC004370

Hartmann, J., Moosdorf, N., Lauerwald, R., Hinderer, M., & West, A. J. (2014). Global chemical weathering and associated p-release - the role of lithology, temperature and soil properties. *Chemical Geology*, *363*, 145–163. https://doi.org/10.1016/j.chemgeo.2013.10.025

Hellmann, R. (1994). The albite-water system: Part I. The kinetics of dissolution as a function of pH at 100, 200 and 300°C. *Geochimica et Cosmochimica Acta*, *58*(2), 595–611. https://doi.org/10.1016/0016-7037(94)90491-X

Hengl, T., De Jesus, J. M., Heuvelink, G. B. M., Gonzalez, M. R., Kilibarda, M., Blagotić, A., Shangguan, W., Wright, M. N., Geng, X., Bauer-Marschallinger, B., Guevara, M. A., Vargas, R., MacMillan, R. A., Batjes, N. H., Leenaars, J. G. B., Ribeiro, E., Wheeler, I., Mantel, S., & Kempen, B. (2017). SoilGrids250m: Global gridded soil information based on machine learning. In *PLoS ONE* (Vol. 12, Issue 2). https://doi.org/10.1371/journal.pone.0169748

Herndon, E., AlBashaireh, A., Singer, D., Roy Chowdhury, T., Gu, B., & Graham, D. (2017). Influence of iron redox cycling on organo-mineral associations in Arctic tundra soil. *Geochimica et Cosmochimica Acta*, *207*, 210–231. https://doi.org/10.1016/j.gca.2017.02.034

Hijmans, R. J., Cameron, S. E., Parra, J. L., Jones, P. G., & Jarvis, A. (2005). Very high resolution interpolated climate surfaces for global land areas. *International Journal of Climatology*, *25*(15), 1965–1978. https://doi.org/10.1002/joc.1276

Hilley, G. E., & Porder, S. (2008). A framework for predicting global silicate weathering and CO2 drawdown rates over geologic time-scales. *Proceedings of the National Academy of Sciences of the United States of America*, *105*(44), 16855–16859. https://doi.org/10.1073/pnas.0801462105

Hindshaw, R. S., Aciego, S. M., & Tipper, E. T. (2018). Li and U Isotopes as a Potential Tool for

Monitoring Active Layer Deepening in Permafrost Dominated Catchments. *Frontiers in Earth Science*, *6*(July), 1–17. https://doi.org/10.3389/feart.2018.00102

Hindshaw, R. S., Teisserenc, R., Le Dantec, T., & Tananaev, N. (2019). Seasonal change of geochemical sources and processes in the Yenisei River: A Sr, Mg and Li isotope study. *Geochimica et Cosmochimica Acta*, *255*, 222–236. https://doi.org/10.1016/j.gca.2019.04.015

Hinzman, L. D., Bettez, N. D., Bolton, W. R., Chapin, F. S., Dyurgerov, M. B., Fastie, C. L., Griffith, B., Hollister, R. D., Hope, A., Huntington, H. P., Jensen, A. M., Jia, G. J., Jorgenson, T., Kane, D. L., Klein, D. R., Kofinas, G., Lynch, A. H., Lloyd, A. H., McGuire, A. D., … Yoshikawa, K. (2005). Evidence and implications of recent climate change in Northern Alaska and other Arctic regions. *Climatic Change*, *72*(3), 251–298. https://doi.org/10.1007/s10584-005-5352-2

Hirst, C., Andersson, P. S., Kooijman, E., Schmitt, M., Kutscher, L., Maximov, T., Mörth, C. M., & Porcelli, D. (2020). Iron isotopes reveal the sources of Fe-bearing particles and colloids in the Lena River basin. *Geochimica et Cosmochimica Acta*, *269*, 678–692. https://doi.org/10.1016/j.gca.2019.11.004

Holder, R. R., & Senecal-Albrecht, D. (1998). *YUKON RIVER COMPREHENSIVE SALMON PLAN FOR ALASKA for the Yukon River Regional Planning Team*.

Huang, F., Chakraborty, P., Lundstrom, C. C., Holmden, C., Glessner, J. J. G., Kieffer, S. W., & Lesher, C. E. (2010). Isotope fractionation in silicate melts by thermal diffusion. *Nature*, *464*(7287), 396–400. https://doi.org/10.1038/nature08840

Huh, Y., Chan, L. H., & Edmond, J. M. (2001). Lithium isotopes as a probe of weathering processes: Orinoco River. *Earth and Planetary Science Letters*, *194*(1–2), 189–199. https://doi.org/10.1016/S0012-821X(01)00523-4

Huh, Y., Chan, L. H., Zhang, L., & Edmond, J. M. (1998). Lithium and its isotopes in major world rivers: implications for weathering and the oceanic budget. *Geochimica et Cosmochimica Acta*, *62*(12), 2039–2051. https://doi.org/10.1016/S0016-7037(98)00126-4

Ingram, B. L., & Weber, P. K. (1999). Salmon origin in California's Sacramento-San Joaquin river system as determined by otolith strontium isotopic composition. *Geology*, *27*(9), 851–854. https://doi.org/10.1130/0091-7613(1999)027<0851:soicss>2.3.co;2

James, R. H., & Palmer, M. R. (2000). The lithium isotope composition of international rock standards. *Chemical Geology*, *166*(3–4), 319–326. https://doi.org/10.1016/S0009-2541(99)00217-X

Jarvis, A., Reuter, H. I., Nelson, A., & Guevara, E. (2008). *CSI SRTM – SRTM 90m DEM Digital Elevation Database*.

Jeffcoate, A. B., Elliott, T., Thomas, A., & Bouman, C. (2004). Precise, small sample size determinations of lithium isotopic compositions of geological reference materials and modern seawater by MC-ICP-MS. *Geostandards and Geoanalytical Research*, *28*(1), 161–172. https://doi.org/10.1111/j.1751-908X.2004.tb01053.x

Jones, S. H., & Fahl, C. B. (1994). Magnitude and frequency of floods in Alaska and

conterminous basins of Canada. In *Water-Resources Investigations Report*. https://doi.org/10.3133/wri934179

Jorgenson, T. M., Harden, J., Kanevskiy, M., O'Donnell, J., Wickland, K., Ewing, S., Manies, K., Zhuang, Q., Shur, Y., Striegl, R., & Koch, J. (2013). Reorganization of vegetation, hydrology and soil carbon after permafrost degradation across heterogeneous boreal landscapes. *Environmental Research Letters*, *8*(3). https://doi.org/10.1088/1748-9326/8/3/035017

Kavanagh, L., Keohane, J., Cleary, J., Cabellos, G. G., & Lloyd, A. (2017). Lithium in the natural waters of the south east of Ireland. *International Journal of Environmental Research and Public Health*, *14*(6), 14–16. https://doi.org/10.3390/ijerph14060561

Keller, K., Blum, J. D., & Kling, G. W. (2010). Stream geochemistry as an indicator of increasing permafrost thaw depth in an arctic watershed. *Chemical Geology*, *273*(1–2), 76–81. https://doi.org/10.1016/j.chemgeo.2010.02.013

Keller, K., Blum, J. D., & Kling, G. W. (2007). Geochemistry of soils and streams on surfaces of varying ages in arctic Alaska. *Arctic, Antarctic, and Alpine Research*, *39*(1), 84–98. https://doi.org/10.1657/1523-0430(2007)39[84:GOSASO]2.0.CO;2

Kirkpatrick, J. J. R., Enion, D. S., & Burd, D. A. R. (1995). Hydrofluoric acid burns: A review. *Burns*, *21*(7), 483–493. http://ovidsp.ovid.com/ovidweb.cgi?T=JS&PAGE=reference&D=emed3&NEWS=N&AN=1995333444

Kisakurek, B., James, R. H., & Harris, N. B. W. (2005). Li and δ7Li in Himalayan rivers: Proxies for silicate weathering? *Earth and Planetary Science Letters*, *237*(3–4), 387–401. https://doi.org/10.1016/j.epsl.2005.07.019

Kokelj, S. V., & Burn, C. R. (2005). Geochemistry of the active layer and near-surface permafrost, Mackenzie delta region, Northwest Territories, Canada. *Canadian Journal of Earth Sciences*, *42*(1), 37–48. https://doi.org/10.1139/E04-089

Košler, J., Kučera, M., & Sylvester, P. (2001). Precise measurement of Li isotopes in planktonic foraminiferal tests by quadrupole ICPMS. *Chemical Geology*, *181*(1–4), 169–179. https://doi.org/10.1016/S0009-2541(01)00280-7

Košler, J., & Magna, T. (2013). Developments in Clean Lab Practices. *Treatise on Geochemistry: Second Edition*, *15*, 111–122. https://doi.org/10.1016/B978-0-08-095975-7.01407-8

Kuhn, M. (2008). Building predictive models in R using the caret package. *Journal of Statistical Software*, *28*(5), 1–26. https://doi.org/10.18637/jss.v028.i05

Lasaga, A. C., Soler, J. M., Ganor, J., Burch, T. E., & Nagy, K. L. (1994). Chemical weathering rate laws and global geochemical cycles. *Geochimica et Cosmochimica Acta*, *58*(10), 2361–2386. https://doi.org/10.1016/0016-7037(94)90016-7

Lawrence, D. M., Slater, A. G., & Swenson, S. C. (2012). Simulation of present-day and future permafrost and seasonally frozen ground conditions in CCSM4. *Journal of Climate*, *25*(7), 2207–2225. https://doi.org/10.1175/JCLI-D-11-00334.1

Lemarchand, E., Chabaux, F., Vigier, N., Millot, R., & Pierret, M. C. (2010). Lithium isotope systematics in a forested granitic catchment (Strengbach, Vosges Mountains, France). *Geochimica et Cosmochimica Acta*, *74*(16), 4612–4628. https://doi.org/10.1016/j.gca.2010.04.057

Li, W., & Liu, X. M. (2020). Experimental investigation of lithium isotope fractionation during kaolinite adsorption: Implications for chemical weathering. *Geochimica et Cosmochimica Acta*, *284*, 156–172. https://doi.org/10.1016/j.gca.2020.06.025

Li, W., Liu, X. M., & Godfrey, L. V. (2019). Optimisation of Lithium Chromatography for Isotopic Analysis in Geological Reference Materials by MC-ICP-MS. *Geostandards and Geoanalytical Research*, *43*(2), 261–276. https://doi.org/10.1111/ggr.12254

Lin, J., Liu, Y., Hu, Z., Chen, W., Zhang, L., & Chen, H. (2019). Accurate Measurement of Lithium Isotopes in Eleven Carbonate Reference Materials by MC-ICP-MS with Soft Extraction Mode and 10 12 Ω Resistor High-Gain Faraday Amplifiers. *Geostandards and Geoanalytical Research*, *43*(2), 277–289. https://doi.org/10.1111/ggr.12260

Liu, X. M., & Li, W. (2019). Optimization of lithium isotope analysis in geological materials by quadrupole ICP-MS. *Journal of Analytical Atomic Spectrometry*, *34*(8), 1708–1717. https://doi.org/10.1039/c9ja00175a

Liu, X. M., & Rudnick, R. L. (2011). Constraints on continental crustal mass loss via chemical weathering using lithium and its isotopes. *Proceedings of the National Academy of Sciences of the United States of America*, *108*(52), 20873–20880. https://doi.org/10.1073/pnas.1115671108

Liu, X. M., Rudnick, R. L., Hier-Majumder, S., & Sirbescu, M. L. C. (2010). Processes controlling lithium isotopic distribution in contact aureoles: A case study of the Florence County pegmatites, Wisconsin. *Geochemistry, Geophysics, Geosystems*, *11*(8), 1–21. https://doi.org/10.1029/2010GC003063

Liu, X. M., Wanner, C., Rudnick, R. L., & McDonough, W. F. (2015). Processes controlling δ7Li in rivers illuminated by study of streams and groundwaters draining basalts. *Earth and Planetary Science Letters*, *409*, 212–224. https://doi.org/10.1016/j.epsl.2014.10.032

Lyon, S. W., & Destouni, G. (2010). Changes in Catchment-Scale Recession Flow Properties in Response to Permafrost Thawing in the Yukon River Basin. *International Journal of Climatology*, *30*(14), 2138–2145. https://doi.org/10.1002/joc.1993

Magna, T., Wiechert, U., & Halliday, A. N. (2006). New constraints on the lithium isotope compositions of the Moon and terrestrial planets. *Earth and Planetary Science Letters*, *243*(3–4), 336–353. https://doi.org/10.1016/j.epsl.2006.01.005

Maher, K. (2010). The dependence of chemical weathering rates on fluid residence time. *Earth and Planetary Science Letters*, *294*(1–2), 101–110. https://doi.org/10.1016/j.epsl.2010.03.010

Mahowald, N. M., Muhs, D. R., Levis, S., Rasch, P. J., Yoshioka, M., Zender, C. S., & Luo, C. (2006). Change in atmospheric mineral aerosols in response to climate: Last glacial period, preindustrial, modern, and doubled carbon dioxide climates. *Journal of Geophysical*

Research Atmospheres, *111*(10). https://doi.org/10.1029/2005JD006653

Mason, T. F. D., Weiss, D. J., Horstwood, M., Parrish, R. R., Russell, S. S., Mullane, E., & Coles, B. J. (2004). High-precision Cu and Zn isotope analysis by plasma source mass spectrometry part 1. Spectral interferences and their correction. *Journal of Analytical Atomic Spectrometry*, *19*(2), 209–217. https://doi.org/10.1039/b306958c

Mavromatis, V., Rinder, T., Prokushkin, A. S., Pokrovsky, O. S., Korets, M. A., Chmeleff, J., & Oelkers, E. H. (2016). The effect of permafrost, vegetation, and lithology on Mg and Si isotope composition of the Yenisey River and its tributaries at the end of the spring flood. *Geochimica et Cosmochimica Acta*, *191*, 32–46. https://doi.org/10.1016/j.gca.2016.07.003

Meybeck, M. (1986). Composition chimique des ruisseaux non pollués en France. Chemical composition of headwater streams in France. *Sciences Géologiques. Bulletin*, *39*(1), 3–77. https://doi.org/10.3406/sgeol.1986.1719

Millot, R., Gaillardet, J., Dupré, B., & Allégre, C. J. (2003). Northern latitude chemical weathering rates: Clues from the Mackenzie River Basin, Canada. *Geochimica et Cosmochimica Acta*, *67*(7), 1305–1329. https://doi.org/10.1016/S0016-7037(02)01207-3

Millot, R., Vigier, N., & Gaillardet, J. (2010). Behaviour of lithium and its isotopes during weathering in the Mackenzie Basin, Canada. *Geochimica et Cosmochimica Acta*, *74*(14), 3897–3912. https://doi.org/10.1016/j.gca.2010.04.025

Misra, S., & Froelich, P. N. (2009). Measurement of lithium isotope ratios by quadrupole-ICP-MS: Application to seawater and natural carbonates. *Journal of Analytical Atomic Spectrometry*, *24*(11), 1524–1533. https://doi.org/10.1039/b907122a

Misra, S., & Froelich, P. N. (2012). Lithium isotope history of cenozoic seawater: Changes in silicate weathering and reverse weathering. *Science*, *335*(6070), 818–823. https://doi.org/10.1126/science.1214697

Molina, A., Vanacker, V., Corre, M. D., & Veldkamp, E. (2019). Patterns in Soil Chemical Weathering Related to Topographic Gradients and Vegetation Structure in a High Andean Tropical Ecosystem. *Journal of Geophysical Research: Earth Surface*, *124*(2), 666–685. https://doi.org/10.1029/2018JF004856

Moriguti, T., & Nakamura, E. (1998). High-yield lithium separation and the precise isotopic analysis for natural rock and aqueous samples. *Chemical Geology*, *145*(1–2), 91–104. https://doi.org/10.1016/S0009-2541(97)00163-0

Murphy, M. J., Porcelli, D., Pogge von Strandmann, P. A. E., Hirst, C. A., Kutscher, L., Katchinoff, J. A., Mörth, C. M., Maximov, T., & Andersson, P. S. (2019). Tracing silicate weathering processes in the permafrost-dominated Lena River watershed using lithium isotopes. *Geochimica et Cosmochimica Acta*, *245*, 154–171. https://doi.org/10.1016/j.gca.2018.10.024

Muskett, R., & Romanovsky, V. (2011). Alaskan Permafrost Groundwater Storage Changes Derived from GRACE and Ground Measurements. *Remote Sensing*, *3*(2), 378–397. https://doi.org/10.3390/rs3020378

Négrel, P., Millot, R., Brenot, A., & Bertin, C. (2010). Lithium isotopes as tracers of

groundwater circulation in a peat land. *Chemical Geology*, *276*(1–2), 119–127. https://doi.org/10.1016/j.chemgeo.2010.06.008

Nishio, Y., & Nakai, S. (2002). Accurate and precise lithium isotopic determinations of igneous rock samples using multi-collector inductively coupled plasma mass spectrometry. *Analytica Chimica Acta*, *456*(2), 271–281. https://doi.org/10.1016/S0003-2670(02)00042-9

Obu, J., Westermann, S., Bartsch, A., Berdnikov, N., Christiansen, H. H., Dashtseren, A., Delaloye, R., Elberling, B., Etzelmüller, B., Kholodov, A., Khomutov, A., Kääb, A., Leibman, M. O., Lewkowicz, A. G., Panda, S. K., Romanovsky, V., Way, R. G., Westergaard-Nielsen, A., Wu, T., … Zou, D. (2019). Northern Hemisphere permafrost map based on TTOP modelling for 2000–2016 at 1 km2 scale. *Earth-Science Reviews*, *193*(October 2018), 299–316. https://doi.org/10.1016/j.earscirev.2019.04.023

Osterkamp, T. E. (2007). Causes of warming and thawing permafrost in Alaska. *Eos*, *88*(48), 522–523. https://doi.org/10.1029/2007EO480002

Palmer, M. R., & Edmond, J. M. (1989). The strontium isotope budget of the modern ocean. *Earth and Planetary Science Letters*, *92*(1), 11–26. https://doi.org/10.1016/0012-821X(89)90017-4

Palmer, M. R., & Edmond, J. M. (1992). Controls over the strontium isotope composition of river water. *Geochimica et Cosmochimica Acta*, *56*(5), 2099–2111. https://doi.org/10.1016/0016-7037(92)90332-D

Patton, W. W., & Box, S. E. (1989). Tectonic setting of the Yukon-Koyukuk basin and its borderlands, western Alaska. *Journal of Geophysical Research*, *94*(B11), 15807–15820. https://doi.org/10.1029/jb094ib11p15807

Peterson, B. J., Holmes, R. M., McClelland, J. W., Vörösmarty, C. J., Lammers, R. B., Shiklomanov, A. I., Shiklomanov, I. A., & Rahmstorf, S. (2002). Increasing river discharge to the Arctic Ocean. *Science*, *298*(5601), 2171–2173. https://doi.org/10.1126/science.1077445

Peterson, E. E. (2015). *STARS: SPATIAL TOOLS FOR THE ANALYSIS OF RIVER SYSTEMS VERSION 2.0.0 - A TUTORIAL*.

Petit, J. C. J., de Jong, J., Chou, L., & Mattielli, N. (2008). Development of Cu and Zn Isotope MC-ICP-MS Measurements: Application to Suspended Particulate Matter and Sediments from the Scheldt Estuary. *Geostandards and Geoanalytical Research*, *32*(2), 149–166. https://doi.org/10.1111/j.1751-908X.2008.00867.x

Phan, T. T., Capo, R. C., Stewart, B. W., Macpherson, G. L., Rowan, E. L., & Hammack, R. W. (2016). Factors controlling Li concentration and isotopic composition in formation waters and host rocks of Marcellus Shale, Appalachian Basin. *Chemical Geology*, *420*, 162–179. https://doi.org/10.1016/j.chemgeo.2015.11.003

Philip Horwitz, E., Dietz, M. L., & Chiarizia, R. (1992). A novel strontium-selective extraction chromatographic resin. *Solvent Extraction and Ion Exchange*, *10*(2), 313–336. https://doi.org/10.1080/07366299208918107

Pietruszka, A. J., & Reznik, A. D. (2008). Identification of a matrix effect in the MC-ICP-MS

due to sample purification using ion exchange resin: An isotopic case study of molybdenum. *International Journal of Mass Spectrometry*, *270*(1–2), 23–30. https://doi.org/10.1016/j.ijms.2007.11.001

Pistiner, J. S., & Henderson, G. M. (2003). Lithium-isotope fractionation during continental weathering processes. *Earth and Planetary Science Letters*, *214*(1–2), 327–339. https://doi.org/10.1016/S0012-821X(03)00348-0

Pogge von Strandmann, P. A. E., Burton, K. W., James, R. H., van Calsteren, P., & Gislason, S. R. (2010). Assessing the role of climate on uranium and lithium isotope behaviour in rivers draining a basaltic terrain. *Chemical Geology*, *270*(1–4), 227–239. https://doi.org/10.1016/j.chemgeo.2009.12.002

Pogge von Strandmann, P. A. E., Burton, K. W., James, R. H., van Calsteren, P., Gíslason, S. R., & Mokadem, F. (2006). Riverine behaviour of uranium and lithium isotopes in an actively glaciated basaltic terrain. *Earth and Planetary Science Letters*, *251*(1–2), 134–147. https://doi.org/10.1016/j.epsl.2006.09.001

Pogge von Strandmann, P. A. E., Burton, K. W., Opfergelt, S., Eiríksdóttir, E. S., Murphy, M. J., Einarsson, A., & Gislason, S. R. (2016). The effect of hydrothermal spring weathering processes and primary productivity on lithium isotopes: Lake Myvatn, Iceland. *Chemical Geology*, *445*, 4–13. https://doi.org/10.1016/j.chemgeo.2016.02.026

Pogge von Strandmann, P. A. E., Frings, P. J., & Murphy, M. J. (2017). Lithium isotope behaviour during weathering in the Ganges Alluvial Plain. *Geochimica et Cosmochimica Acta*, *198*, 17–31. https://doi.org/10.1016/j.gca.2016.11.017

Pogge von Strandmann, P. A. E., & Henderson, G. M. (2015). The Li isotope response to mountain uplift. *Geology*, *43*(1), 67–70. https://doi.org/10.1130/G36162.1

Pogge von Strandmann, P. A. E., Opfergelt, S., Lai, Y. J., Sigfússon, B., Gislason, S. R., & Burton, K. W. (2012). Lithium, magnesium and silicon isotope behaviour accompanying weathering in a basaltic soil and pore water profile in Iceland. *Earth and Planetary Science Letters*, *339–340*, 11–23. https://doi.org/10.1016/j.epsl.2012.05.035

Pokrovsky, O. S., Schott, J., Kudryavtzev, D. I., & Dupré, B. (2005). Basalt weathering in Central Siberia under permafrost conditions. *Geochimica et Cosmochimica Acta*, *69*(24), 5659–5680. https://doi.org/10.1016/j.gca.2005.07.018

Post, E., Alley, R. B., Christensen, T. R., Macias-Fauria, M., Forbes, B. C., Gooseff, M. N., Iler, A., Kerby, J. T., Laidre, K. L., Mann, M. E., Olofsson, J., Stroeve, J. C., Ulmer, F., Virginia, R. A., & Wang, M. (2019). The polar regions in a 2°C warmer world. *Science Advances*, *5*(12). https://doi.org/10.1126/sciadv.aaw9883

Prestrud Anderson, S., Drever, J. I., & Humphrey, N. F. (1997). Chemical weathering in glacial environments. *Geology*, *25*(5), 399. https://doi.org/10.1130/0091-7613(1997)025<0399:cwige>2.3.co;2

Qi, H. P., Coplen, T. B., Wang, Q. Z., & Wang, Y. H. (1997). Unnatural Isotopic Composition of Lithium Reagents. *Analytical Chemistry*, *69*(19), 4076–4078. https://doi.org/10.1021/ac9704669

Qiu, L., Rudnick, R. L., McDonough, W. F., & Merriman, R. J. (2009). Li and δ7Li in mudrocks from the British Caledonides: Metamorphism and source influences. *Geochimica et Cosmochimica Acta*, *73*(24), 7325–7340. https://doi.org/10.1016/j.gca.2009.08.017

Rad, S., Rivé, K., Vittecoq, B., Cerdan, O., & Allègre, C. J. (2013). Chemical weathering and erosion rates in the lesser antilles: An overview in guadeloupe, martinique and dominica. In *Journal of South American Earth Sciences* (Vol. 45, pp. 331–344). Pergamon. https://doi.org/10.1016/j.jsames.2013.03.004

Rasmussen, C., Brantley, S., Richter, D. de B., Blum, A., Dixon, J., & White, A. F. (2011). Strong climate and tectonic control on plagioclase weathering in granitic terrain. *Earth and Planetary Science Letters*, *301*(3–4), 521–530. https://doi.org/10.1016/j.epsl.2010.11.037

Riley, J. P., & Tongudai, M. (1964). The lithium content of sea water. *Deep-Sea Research and Oceanographic Abstracts*, *11*(4), 563–568. https://doi.org/10.1016/0011-7471(64)90002-6

Romanovsky, V. E., Smith, S. L., & Christiansen, H. H. (2010). Permafrost thermal state in the polar northern hemisphere during the international polar year 2007-2009: A synthesis. *Permafrost and Periglacial Processes*, *21*(2), 106–116. https://doi.org/10.1002/ppp.689

Rosner, M., Ball, L., Peucker-Ehrenbrink, B., Blusztajn, J., Bach, W., & Erzinger, J. (2007). A simplified, accurate and fast method for lithium isotope analysis of rocks and fluids, and δ7Li values of seawater and rock reference materials. *Geostandards and Geoanalytical Research*, *31*(2), 77–88. https://doi.org/10.1111/j.1751-908X.2007.00843.x

Rosso, J. J., & Rimstidt, J. D. (2000). A high resolution study of forsterite dissolution rates. *Geochimica et Cosmochimica Acta*, *64*(5), 797–811. https://doi.org/10.1016/S0016-7037(99)00354-3

Rudnick, R. L., Tomascak, P. B., Njo, H. B., & Gardner, L. R. (2004). Extreme lithium isotopic fractionation during continental weathering revealed in saprolites from South Carolina. *Chemical Geology*, *212*(1–2), 45–57. https://doi.org/10.1016/j.chemgeo.2004.08.008

Scudder, G. G. E. (1997). *Environment of the Yukon*.

Serreze, M. C., Walsh, J. E., Chapin, F. S., Osterkamp, T., Dyurgerov, M., Romanovsky, V., Oechel, W. C., Morison, J., Zhang, T., & Barry, R. G. (2000). Observational evidence of recent change in the northern high-latitude environment. *Climatic Change*, *46*(1–2), 159–207. https://doi.org/10.1023/a:1005504031923

Sparks, D. L. (2003). Environmental Soil Chemistry: Second Edition. In *Environmental Soil Chemistry: Second Edition*. Elsevier Inc. https://doi.org/10.1016/B978-0-12-656446-4.X5000-2

Stallard, R. F., & Edmond, J. M. (1983). Oltman , Recent studies Meade et al sediment. *Journal of Geophysical Research*, *88*, 9671–9688.

Starkey, H. C. (1982). The role of clays in fixing lithium. In *Bulletin*. https://doi.org/10.3133/b1278F

Steefel, C. I., & Mäher, K. (2009). Fluid-rock interaction: A reactive transport approach. *Reviews in Mineralogy and Geochemistry*, *70*(1988), 485–532.

https://doi.org/10.2138/rmg.2009.70.11

Striegl, R. G., Aiken, G. R., Dornblaser, M. M., Raymond, P. A., & Wickland, K. P. (2005). A decrease in discharge-normalized DOC export by the Yukon River during summer through autumn. *Geophysical Research Letters*, *32*(21), 1–4. https://doi.org/10.1029/2005GL024413

Sturm, M., Schimel, J., Michaelson, G., Welker, J. M., Oberbauer, S. F., Liston, G. E., Fahnestock, J., & Romanovsky, V. E. (2005). Winter biological processes could help convert arctic tundra to shrubland. *BioScience*, *55*(1), 17–26. https://doi.org/10.1641/0006-3568(2005)055[0017:WBPCHC]2.0.CO;2

Swann, R. L., Laskowski, D. A., & McCall, P. J. (1983). A rapid method of the estimation of the environmental parameters octanol/water partition coeffient, soil sorption constant, water to air ratio, and water solubility. *Residue Reviews*, *Vol. 85*, 17–28. https://doi.org/10.1007/978-1-4612-5462-1_3

Tang, Y. J., Zhang, H. F., Deloule, E., Su, B. X., Ying, J. F., Santosh, M., & Xiao, Y. (2014). Abnormal lithium isotope composition from the ancient lithospheric mantle beneath the North China Craton. *Scientific Reports*, *4*(1), 1–4. https://doi.org/10.1038/srep04274

Taylor, S. R., & McLennan, S. M. (1995). The geochemical evolution of the continental crust. In *Reviews of Geophysics* (Vol. 33, Issue 2, pp. 241–265). John Wiley & Sons, Ltd. https://doi.org/10.1029/95RG00262

Taylor, T. I., & Urey, H. C. (1938). Fractionation of the lithium and potassium isotopes by chemical exchange with zeolites. *The Journal of Chemical Physics*, *6*(8), 429–438. https://doi.org/10.1063/1.1750288

Teng, F. Z., McDonough, W. F., Rudnick, R. L., & Walker, R. J. (2006). Diffusion-driven extreme lithium isotopic fractionation in country rocks of the Tin Mountain pegmatite. *Earth and Planetary Science Letters*, *243*(3–4), 701–710. https://doi.org/10.1016/j.epsl.2006.01.036

Teng, F. Z., McDonough, W. F., Rudnick, R. L., & Wing, B. A. (2007). Limited lithium isotopic fractionation during progressive metamorphic dehydration in metapelites: A case study from the Onawa contact aureole, Maine. *Chemical Geology*, *239*(1–2), 1–12. https://doi.org/10.1016/j.chemgeo.2006.12.003

Theobald, D., Norman, J., Peterson, E., & Ferraz, S. (2005). *Functional linkage of watersheds and streams (FLoWs) :Network-based ArcGIS tools to analyze freshwater ecosystems.*

Tomascak, P. B., Carlson, R. W., & Shirey, S. B. (1999). Accurate and precise determination of Li isotopic compositions by multi-collector sector ICP-MS. *Chemical Geology*, *158*(1–2), 145–154. https://doi.org/10.1016/S0009-2541(99)00022-4

Tomascak, P. B., Magna, T., & Dohmen, R. (2016). *Advances in Lithium Isotope Geochemistry*. Springer International Publishing. https://doi.org/10.1007/978-3-319-01430-2

Toohey, R. C., Herman-Mercer, N. M., Schuster, P. F., Mutter, E. A., & Koch, J. C. (2016). Multidecadal increases in the Yukon River Basin of chemical fluxes as indicators of changing flowpaths, groundwater, and permafrost. *Geophysical Research Letters*, *43*(23), 12,120-12,130. https://doi.org/10.1002/2016GL070817

Van Hoecke, K., Belza, J., Croymans, T., Misra, S., Claeys, P., & Vanhaecke, F. (2015). Single-step chromatographic isolation of lithium from whole-rock carbonate and clay for isotopic analysis with multi-collector ICP-mass spectrometry. *Journal of Analytical Atomic Spectrometry*, *30*(12), 2533–2540. https://doi.org/10.1039/c5ja00165j

Veizer, J., Ala, D., Azmy, K., Bruckschen, P., Buhl, D., Bruhn, F., Carden, G. A. F., Diener, A., Ebneth, S., Godderis, Y., Jasper, T., Korte, C., Pawellek, F., Podlaha, O. G., & Strauss, H. (1999). Srr 86 Sr, d 13 C and d 18 O evolution of Phanerozoic seawater. In *Chemical Geology* (Vol. 161). www.elsevier.comrlocaterchemgeo

Verplanck, P. L., Mueller, S. H., Goldfarb, R. J., Nordstrom, D. K., & Youcha, E. K. (2008). Geochemical controls of elevated arsenic concentrations in groundwater, Ester Dome, Fairbanks district, Alaska. *Chemical Geology*, *255*(1–2), 160–172. https://doi.org/10.1016/j.chemgeo.2008.06.020

Vigier, N., Decarreau, A., Millot, R., Carignan, J., Petit, S., & France-Lanord, C. (2008). Quantifying Li isotope fractionation during smectite formation and implications for the Li cycle. *Geochimica et Cosmochimica Acta*, *72*(3), 780–792. https://doi.org/10.1016/j.gca.2007.11.011

Vigier, N., & Goddéris, Y. (2015). A new approach for modeling Cenozoic oceanic lithium isotope paleo-variations: The key role of climate. *Climate of the Past*, *11*(4), 635–645. https://doi.org/10.5194/cp-11-635-2015

Vincent, W. F., Laurion, I., Pienitz, R., & Walter Anthony, K. M. (2012). Climate Impacts on Arctic Lake Ecosystems. In *Climatic Change and Global Warming of Inland Waters* (pp. 27–42). John Wiley & Sons, Ltd. https://doi.org/10.1002/9781118470596.ch2

Wadleigh, M. A., Veizer, J., & Brooks, C. (1985). Strontium and its isotopes in Canadian rivers: Fluxes and global implications. *Geochimica et Cosmochimica Acta*, *49*(8), 1727–1736. https://doi.org/10.1016/0016-7037(85)90143-7

Wahrhaftig, C., & Nolan, T. B. (1965). Physiographic Divisions of Alaska A classification and brief description with a discussion of high-latitude physiographic processes. In *Professional Paper*. https://doi.org/10.3133/PP482

Walvoord, M. A., & Striegl, R. G. (2007). Increased groundwater to stream discharge from permafrost thawing in the Yukon River basin: Potential impacts on lateral export of carbon and nitrogen. *Geophysical Research Letters*, *34*(12), L12402. https://doi.org/10.1029/2007GL030216

Walvoord, M. A., Voss, C. I., & Wellman, T. P. (2012). Influence of permafrost distribution on groundwater flow in the context of climate-driven permafrost thaw: Example from Yukon Flats Basin, Alaska, United States. *Water Resources Research*, *48*(7). https://doi.org/10.1029/2011WR011595

West, A. J., Galy, A., & Bickle, M. (2005). Tectonic and climatic controls on silicate weathering. *Earth and Planetary Science Letters*, *235*(1–2), 211–228. https://doi.org/10.1016/j.epsl.2005.03.020

White, A. F., & Blum, A. E. (1995). Effects of climate on chemical weathering in watersheds.

Water-Rock Interaction. Proc. Symposium, Vladivostok, 1995, *59*(9), 57–60.

Williams, L. B., & Hervig, R. L. (2005). Lithium and boron isotopes in illite-smectite: The importance of crystal size. *Geochimica et Cosmochimica Acta*, *69*(24), 5705–5716. https://doi.org/10.1016/j.gca.2005.08.005

Wilson, F. H., Dover, J. H., Bradley, D. C., Weber, F. R., Bundtzen, T. K., & Haeussler, P. J. (1998). Geologic map of central (interior) Alaska. In *Open-File Report*. https://doi.org/10.3133/OFR98133B

Wilson, S. (2007). *United States Geological Survey Certificate of Analysis Basalt, Hawaiian Volcanic Observatory, BHVO-2*. http://minerva.union.edu/hollochk/icp-ms/srm/usgs-bhvo2.pdf

Wimpenny, J., Colla, C. A., Yu, P., Yin, Q. Z., Rustad, J. R., & Casey, W. H. (2015). Lithium isotope fractionation during uptake by gibbsite. *Geochimica et Cosmochimica Acta*, *168*, 133–150. https://doi.org/10.1016/j.gca.2015.07.011

Wimpenny, J., James, R. H., Burton, K. W., Gannoun, A., Mokadem, F., & Gíslason, S. R. (2010). Glacial effects on weathering processes: New insights from the elemental and lithium isotopic composition of West Greenland rivers. *Earth and Planetary Science Letters*, *290*(3–4), 427–437. https://doi.org/10.1016/j.epsl.2009.12.042

Witherow, R. A., Lyons, W. B., & Henderson, G. M. (2010). Lithium isotopic composition of the McMurdo Dry Valleys aquatic systems. *Chemical Geology*, *275*(3–4), 139–147. https://doi.org/10.1016/j.chemgeo.2010.04.017

Woo, M. K. (2012). Permafrost hydrology. In *Permafrost Hydrology* (Vol. 9783642234620). Springer-Verlag Berlin Heidelberg. https://doi.org/10.1007/978-3-642-23462-0

Wunder, B., Meixner, A., Romer, R. L., Feenstra, A., Schettler, G., & Heinrich, W. (2007). Lithium isotope fractionation between Li-bearing staurolite, Li-mica and aqueous fluids: An experimental study. *Chemical Geology*, *238*(3–4), 277–290. https://doi.org/10.1016/j.chemgeo.2006.12.001

Wunder, B., Meixner, A., Romer, R. L., & Heinrich, W. (2006). Temperature-dependent isotopic fractionation of lithium between clinopyroxene and high-pressure hydrous fluids. *Contributions to Mineralogy and Petrology*, *151*(1), 112–120. https://doi.org/10.1007/s00410-005-0049-0

Xiao, X., Zhang, F., Li, X., Zeng, C., Shi, X., Wu, H., Jagirani, M. D., & Che, T. (2020). Using stable isotopes to identify major flow pathways in a permafrost influenced alpine meadow hillslope during summer rainfall period. *Hydrological Processes*, *34*(5), 1104–1116. https://doi.org/10.1002/hyp.13650

Yang, L., Dabek-Zlotorzynska, E., & Celo, V. (2009). High precision determination of silver isotope ratios in commercial products by MC-ICP-MS. *Journal of Analytical Atomic Spectrometry*, *24*(11), 1564–1569. https://doi.org/10.1039/b911554d

Zhang, T., Barry, R. G., Knowles, K., Heginbottom, J. A., & Brown, J. (1999). Statistics and characteristics of permafrost and ground-ice distribution in the Northern Hemisphere. *Polar Geography*, *23*(2), 132–154. https://doi.org/10.1080/10889379909377670

Zolkos, S., Tank, S. E., & Kokelj, S. V. (2018). Mineral Weathering and the Permafrost Carbon-Climate Feedback. *Geophysical Research Letters*, *45*(18), 9623–9632. https://doi.org/10.1029/2018GL078748

Zoltai, S. C., Tarnocai, C., & Pettapiece, W. W. (1978). *AGE OF CRYOTURBATED ORGANIC MATERIALS IN EARTH HUMMOCKS FROM THE CANADIAN ARCTIC*.

Zomer, R. J., Trabucco, A., Bossio, D. A., & Verchot, L. V. (2008). Climate change mitigation: A spatial analysis of global land suitability for clean development mechanism afforestation and reforestation. *Agriculture, Ecosystems and Environment*, *126*(1–2), 67–80. https://doi.org/10.1016/j.agee.2008.01.014

Appendix

Table A1: Summary of all $^{87}Sr/^{86}Sr$, $\delta^{7}Li$, and elemental data collected from different rivers across the Yukon River Basin in this study. [Li] and [Sr] are in µmol/L and [Na], [K], [Mg] and [Ca] are in mmol/L. Drainage basins; UY = Upper Yukon, ECY = East Central Yukon, WCY = West Central Yukon, and LY = Lower Yukon.

ID	River name	Lat	Long	Drainage basin	$^{87}Sr/^{86}Sr$	±2σSE	$\delta^{7}Li$	±2σSE	Li (µM)	Na (mM)	K (mM)	Mg (mM)	Ca (mM)	Sr (µM)
5	Tatchun	62.283	-136.307	UY	0.706946	0.000020	23.64	0.04	0.214	0.279	0.057	0.611	0.988	3.818
8	Pelly	62.841	-136.683	Pelly	0.718020	0.000020	15.91	0.25	0.490	0.113	0.020	0.551	0.741	2.134
9	White	61.987	-140.558	White	0.705950	0.000020	13.69	0.36	1.570	0.800	0.072	0.909	1.138	3.743
10	Donjek	61.679	-139.755	White	0.708710	0.000020	16.30	0.44	1.340	0.409	0.143	0.835	1.150	3.298
12	Stewart	63.454	-136.942	Stewart	0.723380	0.000020	16.07	0.21	0.504	0.096	0.015	0.675	0.828	2.431
14	Klondike	64.055	-138.908	UY	0.721460	0.000020	23.06	0.29	0.375	0.109	0.013	0.444	0.684	2.465
16	Fortymile	64.403	-140.597	UY	0.714510	0.000020	18.87	0.39	0.475	0.174	0.020	0.329	0.442	1.541
26	Nordenskiold	61.857	-136.109	UY	0.706220	0.000020	19.53	0.76	0.360	0.296	0.041	0.416	0.973	4.143
30	Willow Cr.	62.837	-136.621	Pelly	0.716860	0.000020	19.46	0.58	0.576	0.190	0.041	0.506	0.998	2.705
32	Drury Cr.	62.201	-134.387	Pelly	0.716080	0.000020	24.38	0.04	0.144	0.083	0.015	0.132	0.339	0.856
34	Pelly	62.221	-133.379	Pelly	0.717300	0.000020	13.76	0.19	0.447	0.083	0.018	0.658	0.811	2.248
38	Teklanika	64.356	-149.632	Tanana	0.711780	0.000020	15.70	0.26	0.864	0.430	0.032	0.813	1.608	4.043
39	Barton Cr.	64.309	-150.124	Kantishna	0.712260	0.000020	22.99	0.21	0.478	0.246	0.036	0.574	1.550	3.510
40	Toklat	64.282	-150.167	Kantishna	0.713130	0.000020	11.75	0.34	1.844	0.443	0.053	0.987	1.572	4.373
41	Clear Cr.	64.315	-150.281	Kantishna	0.712820	0.000020	23.55	0.38	0.478	0.165	0.036	0.614	1.479	3.610

42	Cosna	64.834	-151.442	Tanana	0.711240	0.000020	27.78	0.40	0.540	0.201	0.037	0.444	0.772	1.826
43	Tanana	64.902	-151.447	Tanana	0.716500	0.000020	14.15	0.66	0.663	0.151	0.064	0.319	0.903	1.843
44	Baker Cr.	65.009	-150.380	Tanana	0.709177	0.000020	28.00	0.69	0.270	0.211	0.029	0.345	0.773	2.307
45	Tolovana	65.050	-149.404	Tanana	0.731830	0.000020	32.96	0.53	0.241	0.121	0.037	0.323	0.641	1.566
46	Nenana	64.365	-149.209	Tanana	0.713150	0.000020	14.68	0.45	0.870	0.152	0.068	0.517	1.056	2.514
47	Totatlanika	64.411	-148.798	Tanana	0.729990	0.000020	13.48	0.26	1.380	0.395	0.059	0.640	0.864	2.310
48	Wood	64.451	-148.216	Tanana	0.720990	0.000020	17.06	0.85	0.310	0.105	0.052	0.721	1.582	3.173
49	Clear Cr.	64.644	-147.761	Tanana	0.726050	0.000020	19.49	0.16	0.344	0.147	0.068	0.528	1.529	3.052
50	Beaver Cr.	65.392	-147.292	ECY	0.736220	0.000020	23.09	0.29	0.272	0.065	0.013	0.147	0.312	0.917
51	Beaver Cr.	65.393	-147.291	ECY	0.741290	0.000020	26.62	0.15	0.291	0.092	0.013	0.133	0.243	1.211
52	Birch Cr.	65.516	-146.126	ECY	0.744630	0.000020	25.95	0.35	0.261	0.052	0.013	0.251	0.342	1.279
53	Birch Cr.	65.598	-144.436	ECY	0.731170	0.000020	18.06	0.09	1.046	0.107	0.038	0.250	0.779	1.664
54	Yukon	65.601	-144.012	ECY	0.713150	0.000020	15.14	0.13	0.511	0.127	0.050	0.356	0.840	1.825
55	Kandik	65.571	-141.529	ECY	0.713570	0.000020	16.60	0.24	0.644	0.122	0.013	0.228	0.692	1.422
56	Nation	65.446	-141.348	ECY	0.712430	0.000020	9.08	0.38	1.033	0.097	0.013	0.353	1.659	2.699
57	Tatonduk	65.004	-141.288	ECY	0.712850	0.000020	9.40	0.27	3.737	0.443	0.022	0.727	1.878	3.748
59	Yukon	65.114	-141.609	ECY	0.712305	0.000020	15.03	0.32	0.477	0.139	0.061	0.362	0.891	1.834
60	Charley	65.303	-142.744	ECY	0.718290	0.000020	21.87	0.64	0.470	0.119	0.018	0.124	0.325	1.058
64	Shaw Cr.	64.262	-146.108	Tanana	0.728090	0.000020	27.06	0.16	0.187	0.104	0.034	0.274	0.560	1.460
65	Kantishna	64.507	-150.254	Kantishna	0.711790	0.000020	15.88	0.45	0.841	0.165	0.071	0.387	1.081	2.581
66	Bearpaw	63.929	-150.829	Kantishna	0.723680	0.000020	22.23	0.00	0.158	0.117	0.033	0.296	0.903	2.271
67	McKinley	63.745	-151.676	Kantishna	0.709780	0.000020	15.44	0.51	0.879	0.096	0.092	0.222	0.961	2.191

68	Birch Cr.	63.693	-151.889	Kantishna	0.708510	0.000020	21.54	0.51	0.245	0.117	0.038	0.169	0.983	1.746
69	Foraker	63.654	-152.163	Kantishna	0.710650	0.000020	15.00	0.53	0.807	0.078	0.064	0.230	1.016	1.917
70	Kantishna	63.923	-151.310	Kantishna	0.709740	0.000020	17.12	0.42	0.706	0.091	0.077	0.214	0.953	2.066
71	Chatanika	65.192	-147.256	Tanana	0.741250	0.000020	28.58	0.17	0.274	0.057	0.031	0.239	0.551	1.507
72	Yukon	62.751	-164.498	LY	0.713860	0.000148	15.72	0.37	0.356	0.093	0.031	0.276	0.696	1.327
73	East Fork Andreafsky	62.068	-162.936	LY	0.707771	0.000014	30.29	0.00	0.261	0.132	0.007	0.154	0.227	1.154
74	East and West Fork Andreafsky	62.059	-163.153	LY	0.706673	0.000016	26.05	0.15	0.108	0.140	0.007	0.176	0.432	1.682
76	Sheenjek	67.360	-144.161	Porcupine	0.711010	0.000020	20.38	0.21	0.189	0.046	0.008	0.272	1.099	1.457
77	Coleen	67.374	-142.871	Porcupine	0.710120	0.000020	19.44	0.25	0.177	0.045	0.008	0.176	1.014	1.334
78	Porcupine	67.173	-141.679	Porcupine	0.713500	0.000020	16.89	0.29	0.874	0.191	0.014	0.475	0.843	1.813
80	Salmon Fork Black	66.518	-141.997	Porcupine	0.716310	0.000020	16.12	0.60	0.547	0.079	0.006	0.334	0.579	0.979
81	Black	66.637	-143.098	Porcupine	0.714910	0.000020	18.75	0.22	0.445	0.082	0.006	0.287	0.484	0.927
82	Porcupine	66.754	-144.271	Porcupine	0.713200	0.000020	16.94	0.22	0.789	0.173	0.013	0.440	0.806	1.700
83	East Fork Chandalar	67.394	-146.681	Chandlar	0.712080	0.000020	16.13	0.30	0.244	0.058	0.007	0.373	1.176	1.716
84	Chandalar	67.051	-146.891	Chandlar	0.714640	0.000020	18.80	0.42	0.317	0.090	0.013	0.507	1.124	1.959
85	North Fork Chandalar	67.113	-147.443	Chandlar	0.716890	0.000020	17.85	0.23	0.370	0.133	0.021	0.630	1.075	2.274
86	Hodzana	66.709	-148.687	ECY	0.713069	0.000020	22.30	0.51	0.365	0.116	0.020	0.157	0.429	1.097
88	Chandalar	66.673	-145.966	Chandlar	0.714450	0.000020	17.47	0.25	0.300	0.092	0.014	0.490	1.185	1.955
89	Yukon	66.558	-146.118	ECY	0.715060	0.000020	15.07	0.12	0.538	0.126	0.033	0.396	0.746	1.887

92	Fish Cr.	66.607	-151.264	Koyukuk	0.716270	0.000020	23.09	0.10	0.171	0.074	0.012	0.063	0.132	0.459
94	Upper Koyukuk	66.519	-152.306	Koyukuk	0.714940	0.000020	17.04	0.71	0.437	0.142	0.014	0.846	1.165	2.921
95	Koyukuk	66.829	-151.712	Koyukuk	0.715330	0.000020	17.28	0.22	0.583	0.174	0.014	1.139	1.454	3.700
97	Malamute Fork John	67.047	-152.142	Koyukuk	0.715490	0.000020	18.46	0.35	0.205	0.035	0.009	0.476	1.248	2.269
98	John	67.088	-151.897	Koyukuk	0.716510	0.000020	14.28	0.18	0.774	0.194	0.012	1.421	1.338	3.196
99	Wild	67.037	-151.486	Koyukuk	0.714270	0.000020	16.91	0.09	0.210	0.052	0.014	0.582	1.315	2.606
100	Koyukuk	66.550	-152.544	Koyukuk	0.714910	0.000040	15.50	0.10	0.412	0.144	0.014	0.810	1.142	2.873
102	Middle Fork Koyukuk	67.307	-150.186	Koyukuk	0.714350	0.000020	14.98	0.41	0.672	0.117	0.021	1.156	1.685	4.832
103	Hammond	67.519	-150.114	Koyukuk	0.715350	0.000020	12.44	0.39	1.374	0.150	0.017	2.500	2.508	7.489
104	North Fork Koyukuk	67.051	-151.085	Koyukuk	0.715540	0.000020	16.13	0.43	0.512	0.182	0.012	1.013	1.381	3.738
105	Malamute Fork Alatna	67.112	-152.847	Koyukuk	0.716820	0.000020	15.14	0.68	0.205	0.041	0.011	0.387	0.900	1.840
106	Malamute Fork Alatna	67.106	-153.035	Koyukuk	0.716230	0.000020	16.29	0.26	0.178	0.040	0.011	0.373	0.901	1.768
107	Alatna	66.812	-153.616	Koyukuk	0.716400	0.000020	12.34	0.42	0.612	0.080	0.022	0.766	1.206	2.640
114	Yukon	64.208	-158.642	WCY	0.715010	0.000020	16.43	0.55	0.479	0.110	0.027	0.340	0.719	1.670
115	Rodo	64.218	-158.887	WCY	0.707299	0.000020	31.35	0.35	0.098	0.111	0.005	0.221	0.317	1.303
117	Upper Nulato	64.697	-159.042	WCY	0.707120	0.000020	22.43	0.45	0.251	0.130	0.011	0.384	0.888	3.309
119	Yukon	64.823	-157.051	WCY	0.715450	0.000020	16.05	0.26	0.519	0.115	0.030	0.349	0.736	1.721
120	Koyukuk	65.048	-157.652	Koyukuk	0.711670	0.000020	19.69	1.83	0.248	0.109	0.010	0.369	0.646	1.774
121	Koyukuk	65.177	-157.655	Koyukuk	0.711700	0.000020	19.36	0.08	0.257	0.114	0.011	0.372	0.668	1.803

122	Gisasa	65.089	-158.117	Koyukuk	0.707040	0.000020	25.50	0.43	0.503	0.261	0.013	0.552	1.202	5.399
123	Kateel	65.615	-157.963	Koyukuk	0.707020	0.000020	30.51	0.82	0.277	0.240	0.018	0.367	1.022	4.358
129	Koyukuk	65.557	-156.329	Koyukuk	0.713450	0.000020	17.13	0.00	0.303	0.106	0.010	0.463	0.786	1.914
131	Sulukana	63.875	-154.146	WCY	0.709000	0.000020	23.08	0.68	0.157	0.072	0.008	0.377	0.798	1.386
132	Sethkokna	64.085	-153.270	WCY	0.709550	0.000020	18.92	0.48	0.176	0.062	0.005	0.448	0.880	1.975
133	Nowitna	64.422	-154.066	WCY	0.709939	0.000020	24.50	0.22	0.124	0.074	0.008	0.240	0.493	1.027
134	Yukon	65.057	-153.870	WCY	0.715090	0.000020	15.16	0.32	0.565	0.122	0.031	0.381	0.771	1.804
136	Yukon	65.180	-151.604	WCY	0.714790	0.000020	15.45	0.35	0.566	0.116	0.027	0.399	0.775	1.835
137	Ross	62.040	-132.337	Pelly	0.716399	0.000012	14.21	0.25	0.461	0.072	0.014	0.367	0.689	1.465
138	Pelly	61.989	-132.447	Pelly	0.716403	0.000018	14.24	0.25	0.466	0.074	0.017	0.377	0.696	1.467
139	Macmillan	62.952	-130.471	Stewart	0.717425	0.000014	8.58	0.07	1.227	0.033	0.012	0.263	0.498	0.854
140	Innoko	63.575	-156.359	LY	0.708093	0.000014	27.81	0.10	0.229	0.130	0.010	0.322	0.467	1.265
141	Tolstoi Cr.	63.252	-157.109	LY	0.708717	0.000018	26.63	0.88	0.229	0.113	0.008	0.296	0.407	0.992
142	Dishna	62.910	-157.522	LY	0.707191	0.000018	25.18	0.63	0.209	0.120	0.008	0.335	0.392	1.081
144	Anvik	62.737	-160.679	LY	0.706981	0.000014	29.52	0.43	0.126	0.186	0.009	0.191	0.392	1.182
145	Kantishna	64.001	-151.156	Kantishna	0.709755	0.000020	17.03	0.27	0.801	0.114	0.069	0.259	1.117	2.467
146	Toklat	64.424	-150.284	Kantishna	0.713290	0.000022	13.11	0.35	1.398	0.361	0.040	0.920	1.469	4.116
147	Clearwater Cr.	64.468	-149.323	Tanana	0.715117	0.000018	20.45	0.46	0.950	0.231	0.047	0.544	1.457	3.410
148	Miner	66.195	-138.809	Porcupine	0.716683	0.000010	9.03	0.41	1.313	0.196	0.017	0.464	1.450	2.220
149	Fishing Branch	66.467	-139.350	Porcupine	0.712068	0.000010	14.11	0.49	1.046	0.567	0.021	0.361	0.476	0.724
150	Whitestone	66.422	-138.412	Porcupine	0.710464	0.000010	8.45	0.44	0.947	0.230	0.019	0.436	1.310	1.803
151	Fishing Branch	66.489	-138.874	Porcupine	0.714897	0.000012	12.17	0.45	0.558	0.136	0.014	0.398	1.126	0.997

152	Fishing Branch	66.452	-138.597	Porcupine	0.716224	0.000012	13.10	0.12	0.922	0.220	0.015	0.469	1.187	1.237
154	North Fork Chena	64.945	-146.252	Tanana	0.736584	0.000022	22.46	0.26	0.378	0.082	0.027	0.126	0.488	1.265
156	Tanana	64.156	-145.848	Tanana	0.717321	0.000012	11.42	0.29	0.599	0.151	0.051	0.243	0.841	1.568
157	Toklat	63.743	-150.248	Kantishna	0.710932	0.000014	10.54	0.10	1.833	0.364	0.068	1.556	1.779	6.221
159	Kanuti	66.250	-152.141	Koyukuk	0.712752	0.000038	20.80	0.20	0.225	0.095	0.008	0.112	0.157	0.409

Table A2: Summary of topography and environmental variables for samples collected from different rivers across the Yukon River Basin in this study. Drainage basins; UY = Upper Yukon, ECY = East Central Yukon, WCY = West Central Yukon, and LY = Lower Yukon. Catchment area (km^2), relief (m), Upstream distance from mouth (updist), channel slope (cslope), salt (sea salt deposition), rclay (soil clay content), and rcec (soil cation exchange capacity.)

ID	River name	Drainage basin	Catchment area	relief	updist	cslope	salt	rclay	rcec
5	Tatchun	UY	1041	178	2626610	1.3	0.00	15.2	51.6
8	Pelly	Pelly	49437	296	2585739	1.6	0.00	15.0	44.5
9	White	White	6213	1003	2608805	2.4	0.00	13.6	41.6
10	Donjek	White	3	205	2721231	0.6	0.00	27.0	91.6
12	Stewart	Stewart	36984	616	2555488	1.9	0.00	15.2	42.5
14	Klondike	UY	6737	25	2287785	2.2	0.00	13.3	40.4
16	Fortymile	UY	16547	504	2175522	1.0	0.00	11.1	41.0
26	Nordenskiold	UY	4631	645	2727335	1.7	0.00	15.2	50.5
30	Willow Cr.	Pelly	690	370	2590540	1.0	0.00	12.5	45.2
32	Drury Cr.	Pelly	567	1186	2828982	2.7	0.00	13.7	49.9
34	Pelly	Pelly	21728	119	2899205	1.4	0.00	15.1	44.3
38	Teklanika	Tanana	2146	54	1550550	1.0	0.00	14.7	51.5
39	Barton Cr.	Kantishna	325	273	1501704	0.5	0.00	17.4	57.7
40	Toklat	Kantishna	2926	95	1497344	1.1	0.00	14.3	47.4
41	Clear Cr.	Kantishna	76	99	1504489	0.1	-0.01	33.8	124.9

42	Cosna	Tanana	1534	370	1281037	0.5	0.00	11.3	44.4
43	Tanana	Tanana	112678	273	1264713	1.0	0.00	11.9	44.2
44	Baker Cr.	Tanana	1386	383	1340253	0.5	0.00	10.9	44.7
45	Tolovana	Tanana	8157	185	1451948	0.5	0.00	10.8	43.7
46	Nenana	Tanana	6591	708	1500679	1.4	0.00	12.8	45.0
47	Totatlanika	Tanana	1011	872	1518085	0.8	0.00	16.9	57.8
48	Wood	Tanana	2625	143	1561510	1.7	0.00	13.3	47.8
49	Clear Cr.	Tanana	1449	148	1586659	0.6	0.00	12.7	45.6
50	Beaver Cr.	ECY	1016	769	2013239	1.6	0.00	11.8	41.2
51	Beaver Cr.	ECY	230	1073	2013216	1.0	0.00	11.8	43.2
52	Birch Cr.	ECY	258	697	2006895	0.6	0.00	13.3	39.6
53	Birch Cr.	ECY	4024	82	2037948	0.7	0.00	11.7	41.9
54	Yukon	ECY	308619	513	1861652	1.8	0.00	13.4	45.4
55	Kandik	ECY	1707	479	2038186	0.9	0.00	13.3	37.5
56	Nation	ECY	1106	545	2053426	1.5	0.00	13.0	39.1
57	Tatonduk	ECY	3501	638	2045860	1.5	0.00	13.7	37.7
59	Yukon	ECY	294839	819	2018815	1.8	0.00	13.5	45.6
60	Charley	ECY	4397	440	1945426	1.2	0.00	11.5	43.4
64	Shaw Cr.	Tanana	1018	190	1698857	0.8	0.00	10.4	44.6
65	Kantishna	Kantishna	17576	18	1442387	0.9	0.00	12.7	46.4
66	Bearpaw	Kantishna	1296	19	1577686	1.1	0.00	13.2	46.4

67	McKinley	Kantishna	1970	743	1637228	1.7	0.00	12.9	44.6
68	Birch Cr.	Kantishna	856	21	1665976	2.0	0.00	12.7	46.6
69	Foraker	Kantishna	1860	60	1741722	1.1	0.00	13.0	47.9
70	Kantishna	Kantishna	8873	29	1598975	1.0	0.00	12.4	46.1
71	Chatanika	Tanana	929	692	1670415	1.2	0.00	11.5	42.4
72	Yukon	LY	839295	37	44329	1.1	0.00	13.5	47.4
73	East Fork Andreafsky	LY	1790	150	201092	0.8	0.00	12.5	52.7
74	East and West Fork Andreafsky	LY	6242	124	181274	0.7	0.00	13.9	54.6
76	Sheenjek	Porcupine	11362	103	1920736	1.3	0.00	17.1	42.4
77	Coleen	Porcupine	10022	71	2008700	0.7	0.00	17.3	48.0
78	Porcupine	Porcupine	61228	319	2007715	0.7	0.00	18.7	48.3
80	Salmon Fork Black	Porcupine	5182	331	2042499	1.0	0.00	12.3	42.7
81	Black	Porcupine	14864	390	1934559	0.7	0.00	12.7	47.0
82	Porcupine	Porcupine	79054	11	1801329	0.7	0.00	18.0	48.8
83	East Fork Chandalar	Chandlar	11271	401	1855545	1.5	0.00	16.1	41.2
84	Chandalar	Chandlar	25183	26	1786481	1.4	0.00	15.1	41.0
85	North Fork Chandalar	Chandlar	10337	1195	1817018	1.5	0.00	14.4	41.0
86	Hodzana	ECY	2266	488	1721066	1.1	0.00	12.4	47.9

88	Chandalar	Chandlar	25995	21	1697372	1.4	0.00	15.0	41.6
89	Yukon	ECY	462911	5	1667224	1.4	0.00	14.4	46.1
92	Fish Cr.	Koyukuk	1364	36	1742353	0.5	0.00	13.6	46.3
94	Upper Koyukuk	Koyukuk	26454	68	1647884	1.4	0.00	13.3	42.6
95	Koyukuk	Koyukuk	18247	17	1718129	1.7	0.00	13.4	40.1
97	Malamute Fork John	Koyukuk	395	352	1788632	1.4	0.00	15.1	52.1
98	John	Koyukuk	6026	497	1774400	1.8	0.00	14.4	41.0
99	Wild	Koyukuk	1431	435	1758545	1.1	0.00	12.6	42.4
100	Koyukuk	Koyukuk	26855	25	1626898	1.4	0.00	13.3	42.9
102	Middle Fork Koyukuk	Koyukuk	3601	974	1842027	1.9	0.00	13.4	36.6
103	Hammond	Koyukuk	606	779	1874896	1.8	0.00	14.1	39.5
104	North Fork Koyukuk	Koyukuk	4721	151	1774932	2.0	0.00	13.1	38.8
105	Malamute Fork Alatna	Koyukuk	772	956	1810661	1.8	0.00	12.7	43.4
106	Malamute Fork Alatna	Koyukuk	889	865	1795993	1.7	0.00	12.5	42.9
107	Alatna	Koyukuk	7217	185	1731249	1.7	0.00	13.2	41.4
114	Yukon	WCY	758464	14	776316	1.2	0.00	13.5	46.4
115	Rodo	WCY	369	488	808215	0.5	0.00	13.8	62.4
117	Upper Nulato	WCY	382	971	928278	0.7	0.00	15.1	52.3

119	Yukon	WCY	669220	13	913217	1.2	0.00	13.6	46.0
120	Koyukuk	Koyukuk	79594	453	943029	0.9	0.00	12.7	48.3
121	Koyukuk	Koyukuk	79443	453	958346	0.9	0.00	12.7	48.4
122	Gisasa	Koyukuk	1062	487	1027357	0.8	0.00	12.2	46.1
123	Kateel	Koyukuk	2594	542	1079619	0.6	0.00	12.2	45.1
129	Koyukuk	Koyukuk	65401	295	1156490	1.0	0.00	12.8	47.2
131	Sulukana	WCY	912	534	1439429	0.8	0.00	12.2	43.3
132	Sethkokna	WCY	823	685	1443043	0.7	0.00	12.8	46.9
133	Nowitna	WCY	11455	307	1247834	0.5	0.00	11.7	43.7
134	Yukon	WCY	635485	8	1105047	1.3	0.00	13.7	46.0
136	Yukon	WCY	511357	859	1229748	1.4	0.00	14.2	46.4
137	Ross	Pelly	7025	617	2979046	1.4	0.00	15.5	43.9
138	Pelly	Pelly	18016	749	2966642	1.4	0.00	15.3	43.9
139	Macmillan	Stewart	860	163	3111725	2.2	0.00	16.0	43.4
140	Innoko	LY	3037	142	1186570	0.6	0.00	12.5	44.7
141	Tolstoi Cr.	LY	450	805	1113121	0.5	0.00	17.3	66.2
142	Dishna	LY	1192	288	1177218	0.6	0.00	15.4	58.2
144	Anvik	LY	3824	16	617464	0.9	0.00	12.5	52.1
145	Kantishna	Kantishna	8936	91	1576215	1.0	0.00	12.3	46.1
146	Toklat	Kantishna	3470	89	1463495	1.0	0.00	14.1	47.0
147	Clearwater Cr.	Tanana	46	35	1499161	0.2	0.00	11.9	45.1

148	Miner	Porcupine	3811	26	2530382	1.1	0.00	16.7	37.1
149	Fishing Branch	Porcupine	1612	597	2570252	1.0	0.00	17.7	39.3
150	Whitestone	Porcupine	1305	421	2491259	0.3	0.00	19.1	44.1
151	Fishing Branch	Porcupine	3809	655	2514132	1.0	0.00	17.3	38.9
152	Fishing Branch	Porcupine	4226	102	2483862	1.0	0.00	17.3	38.9
154	North Fork Chena	Tanana	982	608	1725256	1.1	0.00	10.5	40.2
156	Tanana	Tanana	35053	310	1716645	1.4	0.00	11.6	43.8
157	Toklat	Kantishna	472	1329	1571807	1.5	0.00	15.1	51.9
159	Kanuti	Koyukuk	5517	68	1715480	0.6	0.00	12.3	42.4

Table A3: Summary of climatic and environmental variables for samples collected from different rivers across the Yukon River Basin in this study. Drainage basins; UY = Upper Yukon, ECY = East Central Yukon, WCY = West Central Yukon, and LY = Lower Yukon. Permafrost distribution probability (perp), rph (soil pH), magt (mean annual ground temperature), mat (mean air temperature), pet (potential evapotranspiration), glacier (%), and last glacial maximum (lgm, %).

ID	**River name**	**Drainage basin**	**perp**	rph	**magt**	**mat**	**pet**	**glacier**	**lgm**
5	Tatchun	UY	0.08	5.9	1.13	-2.91	561.9	0.00	0.83
8	Pelly	Pelly	0.15	5.7	0.92	-4.20	504.7	0.00	0.96
9	White	White	0.51	5.0	-0.95	-5.73	396.0	0.29	1.00
10	Donjek	White	1.73	13.7	-1.05	-8.04	1139.8	0.00	1.00
12	Stewart	Stewart	0.45	5.5	-0.23	-5.20	477.6	0.00	0.73
14	Klondike	UY	0.84	5.4	-1.29	-5.50	484.0	0.00	0.26
16	Fortymile	UY	0.93	5.3	-1.75	-5.55	532.9	0.00	0.00
26	Nordenskiold	UY	0.31	6.0	0.42	-2.84	532.0	0.00	0.94
30	Willow Cr.	Pelly	0.21	5.6	0.66	-3.86	551.4	0.00	0.00
32	Drury Cr.	Pelly	0.27	5.7	0.42	-3.76	517.3	0.00	1.00
34	Pelly	Pelly	0.12	5.6	1.03	-4.43	494.2	0.00	1.00
38	Teklanika	Tanana	0.49	5.7	-0.04	-3.36	503.6	0.01	0.16
39	Barton Cr.	Kantishna	0.48	6.8	0.40	-4.11	667.7	0.00	0.00
40	Toklat	Kantishna	0.47	5.2	-0.07	-3.22	462.6	0.01	0.16
41	Clear Cr.	Kantishna	1.13	13.6	0.18	-8.50	1346.2	0.00	0.00

42	Cosna	Tanana	0.22	5.3	0.75	-3.48	515.2	0.00	0.00
43	Tanana	Tanana	0.45	5.3	-0.10	-3.75	502.9	0.04	0.23
44	Baker Cr.	Tanana	0.36	5.4	0.39	-3.77	546.9	0.00	0.00
45	Tolovana	Tanana	0.44	5.5	0.10	-3.42	534.2	0.00	0.00
46	Nenana	Tanana	0.44	5.5	-0.04	-3.50	460.4	0.03	0.57
47	Totatlanika	Tanana	0.50	6.4	0.26	-3.53	607.7	0.00	0.00
48	Wood	Tanana	0.44	6.1	-0.04	-3.70	531.4	0.03	0.25
49	Clear Cr.	Tanana	0.29	6.1	0.65	-3.30	564.5	0.00	0.00
50	Beaver Cr.	ECY	0.81	5.0	-1.27	-4.32	479.4	0.00	0.00
51	Beaver Cr.	ECY	0.77	5.0	-1.10	-4.18	472.9	0.00	0.00
52	Birch Cr.	ECY	0.96	5.3	-2.15	-5.50	501.7	0.00	0.00
53	Birch Cr.	ECY	0.87	5.2	-1.54	-5.30	518.6	0.00	0.00
54	Yukon	ECY	0.43	5.5	0.11	-4.11	502.5	0.02	0.62
55	Kandik	ECY	0.77	5.2	-0.90	-6.28	483.6	0.00	0.00
56	Nation	ECY	0.74	5.3	-0.79	-5.93	486.9	0.00	0.00
57	Tatonduk	ECY	0.82	5.4	-1.39	-6.27	487.0	0.00	0.06
59	Yukon	ECY	0.41	5.5	0.16	-4.05	502.1	0.02	0.65
60	Charley	ECY	0.88	5.3	-1.77	-5.57	512.1	0.00	0.02
64	Shaw Cr.	Tanana	0.17	5.6	1.00	-2.81	545.1	0.00	0.00
65	Kantishna	Kantishna	0.28	5.1	0.58	-3.44	476.6	0.04	0.17
66	Bearpaw	Kantishna	0.26	5.0	0.79	-3.31	490.5	0.00	0.00

67	McKinley	Kantishna	0.34	4.9	-0.19	-4.12	402.9	0.23	0.77
68	Birch Cr.	Kantishna	0.20	4.9	0.68	-4.02	431.8	0.11	0.29
69	Foraker	Kantishna	0.18	5.3	1.11	-3.87	471.7	0.09	0.33
70	Kantishna	Kantishna	0.22	5.1	0.76	-3.63	458.6	0.08	0.28
71	Chatanika	Tanana	0.65	5.2	-0.52	-3.94	510.0	0.00	0.00
72	Yukon	LY	0.55	5.4	-0.70	-4.62	471.2	0.01	0.31
73	East Fork Andreafsky	LY	0.32	5.0	0.57	-1.80	394.0	0.00	0.00
74	East and West Fork Andreafsky	LY	0.38	5.0	0.41	-1.69	392.0	0.00	0.00
76	Sheenjek	Porcupine	0.99	5.6	-5.84	-8.52	323.1	0.00	0.13
77	Coleen	Porcupine	0.98	5.6	-5.02	-8.60	340.0	0.00	0.00
78	Porcupine	Porcupine	0.97	5.2	-3.91	-8.39	396.5	0.00	0.31
80	Salmon Fork Black	Porcupine	0.86	5.5	-1.28	-6.72	453.7	0.00	0.00
81	Black	Porcupine	0.82	5.7	-1.04	-6.55	489.7	0.00	0.00
82	Porcupine	Porcupine	0.97	5.3	-3.84	-8.28	393.6	0.00	0.24
83	East Fork Chandalar	Chandlar	0.99	5.8	-6.35	-8.51	335.2	0.00	0.61
84	Chandalar	Chandlar	0.97	5.7	-4.99	-7.75	381.5	0.00	0.47
85	North Fork Chandalar	Chandlar	0.96	5.6	-4.16	-7.21	416.4	0.00	0.48
86	Hodzana	ECY	0.73	5.5	-0.99	-5.29	491.9	0.00	0.00

88	Chandalar	Chandlar	0.96	5.7	-4.87	-7.70	385.4	0.00	0.46
89	Yukon	ECY	0.60	5.5	-1.12	-5.32	471.1	0.01	0.48
92	Fish Cr.	Koyukuk	0.58	5.1	-0.43	-5.10	481.3	0.00	0.00
94	Upper Koyukuk	Koyukuk	0.86	5.4	-2.64	-6.37	418.3	0.00	0.24
95	Koyukuk	Koyukuk	0.94	5.5	-3.42	-6.76	395.9	0.00	0.34
97	Malamute Fork John	Koyukuk	1.04	6.3	-1.80	-7.25	511.2	0.00	0.00
98	John	Koyukuk	0.97	5.5	-3.98	-7.26	369.2	0.00	0.45
99	Wild	Koyukuk	0.94	5.5	-2.15	-6.32	433.3	0.00	0.00
100	Koyukuk	Koyukuk	0.85	5.4	-2.61	-6.35	419.7	0.00	0.23
102	Middle Fork Koyukuk	Koyukuk	0.96	5.7	-3.96	-6.76	401.2	0.00	0.45
103	Hammond	Koyukuk	1.04	6.0	-4.32	-7.34	418.8	0.00	0.20
104	North Fork Koyukuk	Koyukuk	0.96	5.6	-3.78	-6.84	389.0	0.00	0.39
105	Malamute Fork Alatna	Koyukuk	0.88	5.6	-1.50	-6.22	444.7	0.00	0.00
106	Malamute Fork Alatna	Koyukuk	0.86	5.5	-1.43	-6.11	439.9	0.00	0.00
107	Alatna	Koyukuk	0.86	5.5	-2.24	-6.27	378.8	0.00	0.41
114	Yukon	WCY	0.56	5.4	-0.81	-4.89	473.7	0.01	0.34
115	Rodo	WCY	0.25	6.5	0.91	-3.57	507.3	0.00	0.00
117	Upper Nulato	WCY	0.56	6.6	-0.01	-4.15	461.7	0.00	0.00

119	Yukon	WCY	0.56	5.5	-0.80	-4.90	480.3	0.01	0.37
120	Koyukuk	Koyukuk	0.59	5.3	-0.97	-5.01	425.2	0.00	0.12
121	Koyukuk	Koyukuk	0.59	5.3	-0.97	-5.02	426.0	0.00	0.12
122	Gisasa	Koyukuk	0.49	5.3	-0.09	-3.54	385.0	0.00	0.00
123	Kateel	Koyukuk	0.61	5.1	-0.45	-3.45	369.3	0.00	0.00
129	Koyukuk	Koyukuk	0.62	5.3	-1.19	-5.36	428.7	0.00	0.14
131	Sulukana	WCY	0.13	5.1	1.30	-2.51	469.0	0.00	0.00
132	Sethkokna	WCY	0.11	5.9	1.51	-3.24	544.6	0.00	0.00
133	Nowitna	WCY	0.14	5.1	1.22	-2.80	481.2	0.00	0.00
134	Yukon	WCY	0.58	5.5	-0.90	-5.00	480.7	0.02	0.39
136	Yukon	WCY	0.61	5.5	-1.11	-5.30	475.4	0.01	0.44
137	Ross	Pelly	0.10	5.7	1.05	-4.65	498.0	0.00	1.00
138	Pelly	Pelly	0.10	5.6	1.08	-4.57	493.9	0.00	1.00
139	Macmillan	Stewart	0.39	5.3	-0.17	-6.03	438.3	0.02	1.00
140	Innoko	LY	0.23	4.9	0.86	-2.47	465.9	0.00	0.01
141	Tolstoi Cr.	LY	0.37	6.4	0.99	-2.84	591.9	0.00	0.03
142	Dishna	LY	0.30	5.4	0.82	-2.37	493.2	0.00	0.01
144	Anvik	LY	0.27	5.1	0.66	-2.29	404.7	0.00	0.00
145	Kantishna	Kantishna	0.22	5.1	0.76	-3.63	458.5	0.08	0.28
146	Toklat	Kantishna	0.46	5.2	-0.01	-3.22	472.2	0.01	0.13
147	Clearwater Cr.	Tanana	0.31	5.9	0.39	-3.12	559.1	0.00	0.00

148	Miner	Porcupine	0.92	5.3	-2.52	-7.45	449.6	0.00	0.01
149	Fishing Branch	Porcupine	1.00	5.7	-2.82	-8.21	468.5	0.00	0.00
150	Whitestone	Porcupine	1.00	4.9	-3.53	-7.96	416.2	0.00	0.00
151	Fishing Branch	Porcupine	0.96	5.3	-2.85	-8.02	442.7	0.00	0.00
152	Fishing Branch	Porcupine	0.96	5.3	-2.87	-7.98	440.4	0.00	0.00
154	North Fork Chena	Tanana	0.64	5.0	-0.55	-4.13	504.5	0.00	0.00
156	Tanana	Tanana	0.63	5.3	-0.81	-4.40	510.9	0.07	0.39
157	Toklat	Kantishna	0.66	5.9	-0.83	-3.78	465.4	0.06	0.59
159	Kanuti	Koyukuk	0.47	5.2	-0.08	-4.76	491.1	0.00	0.00

Table A4: Summary of geological variables for samples collected from different rivers across the Yukon River Basin in this study. Drainage basins; UY = Upper Yukon, ECY = East Central Yukon, WCY = West Central Yukon, and LY = Lower Yukon. Siliciclastic rock unit in % (per_sil), carbonate rock unit in % (per_carb), volcanic rock unit in % (per_vol), and metamorphic rock unit in % (per_meta). The composition of each lithology is in Table 5.

ID	**River name**	**Drainage basin**	per_sil	per_carb	per_vol	per_meta
5	Tatchun	UY	0.71	0.07	1.01	0.11
8	Pelly	Pelly	0.92	0.54	0.30	0.26
9	White	White	0.66	0.06	0.84	0.00
10	Donjek	White	0.92	0.00	0.07	0.00
12	Stewart	Stewart	1.37	0.39	0.09	0.59
14	Klondike	UY	1.22	0.44	0.05	0.35
16	Fortymile	UY	0.01	0.39	0.74	1.21
26	Nordenskiold	UY	0.69	0.06	0.79	0.13
30	Willow Cr.	Pelly	0.60	0.00	0.38	0.19
32	Drury Cr.	Pelly	0.08	0.04	1.10	0.40
34	Pelly	Pelly	0.96	0.57	0.26	0.17
38	Teklanika	Tanana	1.25	0.00	0.18	0.43
39	Barton Cr.	Kantishna	1.07	0.00	0.00	0.00
40	Toklat	Kantishna	1.01	0.00	0.22	0.72
41	Clear Cr.	Kantishna	1.00	0.00	0.00	0.00

42	Cosna	Tanana	1.36	0.00	0.27	0.84
43	Tanana	Tanana	0.80	0.05	0.31	0.75
44	Baker Cr.	Tanana	2.77	0.00	0.04	0.13
45	Tolovana	Tanana	1.05	0.00	0.05	1.26
46	Nenana	Tanana	1.50	0.03	0.26	0.42
47	Totatlanika	Tanana	1.60	0.00	0.08	0.12
48	Wood	Tanana	1.19	0.00	0.03	0.38
49	Clear Cr.	Tanana	1.15	0.01	0.01	0.14
50	Beaver Cr.	ECY	0.33	0.00	0.24	1.76
51	Beaver Cr.	ECY	0.87	0.00	0.26	1.74
52	Birch Cr.	ECY	0.00	0.00	0.05	1.95
53	Birch Cr.	ECY	0.29	0.10	0.20	1.52
54	Yukon	ECY	0.72	0.26	0.50	0.44
55	Kandik	ECY	1.25	0.00	0.41	0.01
56	Nation	ECY	1.59	0.10	0.09	0.00
57	Tatonduk	ECY	1.46	0.63	0.01	0.06
59	Yukon	ECY	0.71	0.27	0.49	0.45
60	Charley	ECY	0.09	0.26	1.27	0.56
64	Shaw Cr.	Tanana	0.01	0.00	0.04	1.95
65	Kantishna	Kantishna	1.14	0.00	0.10	0.71
66	Bearpaw	Kantishna	1.24	0.00	0.07	0.97

67	McKinley	Kantishna	0.90	0.00	0.49	0.24
68	Birch Cr.	Kantishna	1.28	0.00	0.02	0.44
69	Foraker	Kantishna	1.24	0.00	0.01	0.59
70	Kantishna	Kantishna	1.11	0.00	0.12	0.89
71	Chatanika	Tanana	0.00	0.00	0.03	1.97
72	Yukon	LY	0.92	0.19	0.49	0.45
73	East Fork Andreafsky	LY	1.82	0.00	0.18	0.00
74	East and West Fork Andreafsky	LY	1.86	0.00	0.12	0.00
76	Sheenjek	Porcupine	0.99	1.25	0.44	0.02
77	Coleen	Porcupine	0.53	1.10	0.24	0.52
78	Porcupine	Porcupine	1.37	0.15	0.05	0.06
80	Salmon Fork Black	Porcupine	1.62	0.10	0.00	0.22
81	Black	Porcupine	1.50	0.04	0.11	0.28
82	Porcupine	Porcupine	1.25	0.26	0.09	0.20
83	East Fork Chandalar	Chandlar	0.86	1.55	0.02	0.43
84	Chandalar	Chandlar	1.03	0.92	0.12	0.78
85	North Fork Chandalar	Chandlar	1.16	0.41	0.26	1.00
86	Hodzana	ECY	0.58	0.00	0.83	1.16
88	Chandalar	Chandlar	1.04	0.89	0.12	0.76
89	Yukon	ECY	0.89	0.30	0.38	0.39
92	Fish Cr.	Koyukuk	0.64	0.00	0.80	1.11

94	Upper Koyukuk	Koyukuk	1.10	0.36	0.37	0.79
95	Koyukuk	Koyukuk	1.22	0.52	0.13	0.93
97	Malamute Fork John	Koyukuk	0.92	0.59	0.10	0.93
98	John	Koyukuk	1.45	0.83	0.00	0.61
99	Wild	Koyukuk	1.05	0.39	0.10	1.13
100	Koyukuk	Koyukuk	1.10	0.36	0.38	0.78
102	Middle Fork Koyukuk	Koyukuk	1.01	0.46	0.06	1.33
103	Hammond	Koyukuk	1.08	0.26	0.00	1.65
104	North Fork Koyukuk	Koyukuk	1.22	0.45	0.14	1.12
105	Malamute Fork Alatna	Koyukuk	0.85	0.44	0.47	0.77
106	Malamute Fork Alatna	Koyukuk	0.86	0.39	0.43	0.92
107	Alatna	Koyukuk	0.99	0.71	0.23	0.69
114	Yukon	WCY	0.89	0.21	0.49	0.47
115	Rodo	WCY	1.97	0.00	0.03	0.00
117	Upper Nulato	WCY	1.84	0.00	0.16	0.00
119	Yukon	WCY	0.89	0.22	0.40	0.48
120	Koyukuk	Koyukuk	0.78	0.18	1.18	0.36
121	Koyukuk	Koyukuk	0.78	0.18	1.18	0.36
122	Gisasa	Koyukuk	1.41	0.00	0.59	0.00
123	Kateel	Koyukuk	1.09	0.00	0.91	0.00
129	Koyukuk	Koyukuk	0.79	0.22	1.08	0.43

131	Sulukana	WCY	1.21	0.00	0.17	1.35
132	Sethkokna	WCY	0.68	0.00	0.64	1.36
133	Nowitna	WCY	0.98	0.00	0.58	1.08
134	Yukon	WCY	0.89	0.23	0.38	0.48
136	Yukon	WCY	0.90	0.27	0.39	0.41
137	Ross	Pelly	0.95	0.94	0.18	0.13
138	Pelly	Pelly	0.97	0.65	0.19	0.20
139	Macmillan	Stewart	1.07	0.61	0.28	0.00
140	Innoko	LY	1.80	0.00	0.15	0.04
141	Tolstoi Cr.	LY	1.68	0.00	0.09	0.25
142	Dishna	LY	1.55	0.00	0.51	0.01
144	Anvik	LY	0.80	0.00	1.57	0.00
145	Kantishna	Kantishna	1.11	0.00	0.12	0.89
146	Toklat	Kantishna	1.02	0.00	0.19	0.61
147	Clearwater Cr.	Tanana	1.00	0.00	0.00	0.00
148	Miner	Porcupine	1.49	0.35	0.00	0.00
149	Fishing Branch	Porcupine	1.46	0.38	0.00	0.00
150	Whitestone	Porcupine	2.00	0.00	0.00	0.00
151	Fishing Branch	Porcupine	1.48	0.20	0.00	0.00
152	Fishing Branch	Porcupine	1.45	0.20	0.00	0.00
154	North Fork Chena	Tanana	0.00	0.00	0.03	1.97

156	Tanana	Tanana	0.49	0.07	0.72	0.65
157	Toklat	Kantishna	0.89	0.00	0.37	0.78
159	Kanuti	Koyukuk	0.56	0.00	1.20	0.47

Table A5: Summary of composition of each lithology. Each lithology corresponds to the geological variable in Table 4.

Lithology	**Composition**
Siliciclastic rock unit (per_sil)	SSMX (mixed clay), SSMXCL (siliciclastic mixed chlorite), SSLOGL (siliciclastic loess glacial), SMMX (siliciclastic mixed mixed grained), SMMXCH (mixed sediments mixed grained chert), SSPYVR (siliciclastic sediment pyroclastic volcanic rocks), SSSH (siliciclastic sediment shale), SSHCH (siliciclastic sediment shale chert), SM_NOT_VR (mixed sediment not volcanic), SS_PLUS_SMV (siliciclastic sediment and volcanic sediment)
Carbonate rock unit (per_carb)	PU (pure carbonate), SC (carbonate), SC_ALL (carbonate all), SCMXCH (carbonate mixed grained chert), SMSHCH (mixed shale cert), CH (chert), EV (evaporite)
Volcanic rock unit (per_vol)	SUPY (unconsolidated sediment pyroclastic). XXPA (plutonic felsic), XXPB (plutonic mafic), XXPI (plutonic intermediate), XXVA (volcanic felsic), XXVB (volcanic mafic), XXVI (volcanic intermediate). XXPY (pyroclastic), PA (plutonic felsic rock), VB (plutonic mafic rock), PI (plutonic intermediate), VI (volcanic intermediate), PIVI (plutonic and volcanic intermediate), SMPYVR (mixed sediment pyroclastic volcanic rock)
Metamorphic rock unit (per_meta)	XXMTMA (metamorphic mafic rock), XXMTSR (metamorphic other rock), MTPU (metamorphic carbonate), MTAM (metamorphic mafic rock), MT (metamorphic rock), SMMXMT (mixed sediment metamorphic), SMSHMT (mixed sediment shale metamorphic)